Air-sea interaction at the synoptic- and the meso-scale

Aimie Moulin

Aimie Moulin. Air-sea interaction at the synoptic- and the meso-scale. Earth Sciences. Université Grenoble Alpes, 2015. English. NNT : 2015GREAU026 . tel-01561705

HAL Id: tel-01561705
https://theses.hal.science/tel-01561705v1

Submitted on 13 Jul 2017

UNIVERSITE DE GRENOBLE

THÈSE

Pour obtenir le grade de

DOCTEUR DE L'UNIVERSITÉ DE GRENOBLE

Spécialité : **Océan, Atmosphère, Hydrologie**

Arrêté ministériel : 7 août 2006

Présentée par

Aimie MOULIN

Thèse dirigée par **Achim Wirth**

préparée au sein **du Laboratoire des Ecoulements Géophysiques et Industriels (UMR 5519)**
et de **l'école doctorale Terre Univers et Environnement**

Air-sea interaction at the synoptic and the mesoscale

Thèse soutenue publiquement le **04/11/2015**,
devant le jury composé de :

Mme, Chantal Staquet
Pr, UJF (Grenoble), Présidente
Mr, Nick Hall
Pr, UPS, Univ Toulouse, Rapporteur
Mr, David Straub
DR, McGill University (Quebec), Rapporteur
Mme, Alessandra Sabina Lanotte
CR, ISAC (Italie), Examinateur
Mr, Florian Lemarié
INRIA Researcher, LJK, Examinateur
Mr, Achim Wirth
DR, LEGI, Directeur de thèse

Remerciements

Je voudrais remercier tout particulièrement Achim Wirth, qui m'a dirigé tout au long de ces trois années de thèse. Merci pour la disponibilité, l'écoute de mes nombreuses questions, et l'intérêt pour l'avancement de mes travaux. Les nombreuses discussions que nous avons eues ainsi que les conseils sont pour beaucoup dans le résultat final de ce travail. Enfin, les nombreuses relectures et corrections ont été très appréciables. J'ai énormément appris à tes côtés, pour tout cela MERCI.

Je remercie Alessandra Lanotte avec qui j'ai eu la chance de pouvoir travailler durant 1 mois et qui m'a accueilli au laboratoire ISAC à Lecce. Nos discussions ainsi que son point de vue m'ont permis de progresser et de prendre du recul sur mes travaux.

Je voudrais remercier Nick Hall et David Straub d'avoir accepté de relire cette thèse et d'en être rapporteurs. La version finale de ce mémoire a bénéficié de leur lecture très attentive et de leurs remarques précieuses. Je tiens à remercier Chantal Staquet d'avoir accepté d'être présidente du jury, et de m' avoir apporté son aide et ses conseils pour les corrections de la version finale. Je remercie aussi Florian Lemarié, Alessandra Lanotte ainsi que tous les autres membres du jury d'avoir accepté d'assister à la présentation de ce travail.

Je remercie aussi l'école doctorale Terre Univers Environnement et en particulier Jean Braun et Christine Bigot pour leur disponibilité et leur gentillesse.

Je tiens également à remercier le LEGI pour l'accueil et les conditions de travail qui m'ont été offertes. Je voudrais remercier particulièrement le support informatique pour leur sympathie et leur efficacité dans la résolution des problèmes.

Je remercie tous les thésards du LEGI pour la bonne ambiance de travail mais également pour les nombreux bons moments passés ensemble aux cours de ces trois années. Avec un remerciement particulier à mon "co-bureau" pour les pauses cafés, les discussions et pour avoir supporté le chauffage dans le bureau.

Enfin, je remercie également tous mes amis pour le soutien et les sorties qui m'ont permis d'oublier momentanément le travail.

On finit toujours par le meilleur...alors MERCI à mes parents et à mes sœurs. Je n' aurais rien fait de tout cela sans votre soutien.

Résumé

Cette thèse concerne l'étude de l'interaction air-mer, due aux échanges de mouvements, avec un modèle idéalisé mais consistant. Les études sont réalisées à partir d'un modèle shallow-water bicouches (une pour l'océan et une pour l'atmosphère), avec une fine résolution spatiale et temporelle. L'interaction est uniquement due à la friction de surface entre les deux couches. Elle est implémentée par une loi de friction quadratique. La force appliquée à l'océan est calculée en utilisant la différence de vitesse entre les vents et les courants. Pour la force appliquée à l'atmosphère on distingue deux cas l'interaction "1way" et "2way". Pour la première, la friction appliquée à l'atmosphère néglige la dynamique de l'océan ; elle est calculée en utilisant uniquement les vents. Pour l'interaction "2W", la friction appliquée à l'atmosphère est l'opposée de celle appliquée à l'océan. Trois configurations idéalisées sont explorées ici.

La première configuration explique la génération d'une instabilité barotrope dans l'océan due à la force de friction quadratique et la dissipation visqueuse horizontale de l'atmosphère. Dans le cas 1W le cisaillement entraîne une instabilité barotrope dans l'océan. Dans le cas d'une interaction 2W, l'instabilité est amplifiée en amplitude et en dimension et est transférée à l'atmosphère. L'échelle principal de cette instabilité correspond à celle du rayon de déformation de Rossby dans l'océan. Elle est uniquement visible dans les modèles numériques, lorsque la dynamique est résolue à cette échelle à la fois dans l'océan mais aussi dans l'atmosphère. Dans la deuxième configuration, des expériences pour différentes valeurs du coefficient de traînée de surface sont réalisées. Le forçage diffère de la première configuration, et permet d'avoir une dynamique turbulente dans l'océan et l'atmosphère. L'énergie perdue par l'atmosphère et gagnée par l'océan par cisaillement à l'interface sont déterminées et comparées aux estimations basées sur les vitesses moyennes. La corrélations entre la vorticité océanique et atmosphérique est déterminée à l'échelle synoptique et méso-échelle de l'atmosphère. Les résultats diffèrent des études dans lesquelles les échanges sont considérés à l'échelle du bassin. L'océan a un rôle passif, et absorbe l'énergie cinétique à quasiment tout les instants et tous les lieux. De par les faibles vitesses de l'océan, le transfert d'énergie dépend que faiblement des courants. La dynamique de l'océan laisse cependant son empreinte dans la dynamique de l'atmosphère conduisant à un état "quenched disorder" du système océan-atmosphère, pour le plus fort coefficient de friction utilisé. La dernière configuration, considère l'échange de mouvements entre l'océan et l'atmosphère autour d'une île circulaire. Dans les simulations actuelles de la dynamique océanique, le champs du forçage atmosphérique est généralement trop grossier pour inclure la présence de petites îles (diamètre inférieur à 100km). Dans les calculs présentés ici, l'île est représenté dans la couche atmosphérique par un coefficient de traînée cent fois plus fort au dessus de l'île que l'océan. Cela engendre de la vorticité dans l'atmosphère , autour et près du sillage de l'île. L'influence de la vorticité atmosphérique sur la vorticité de l'océan, l'upwelling, la turbulence et le transfert d'énergie est considéré en utilisant des simulations couplées océan-atmosphère. Les résultats sont comparés avec des simulations ayant un forçage atmosphérique constant dans le temps et l'espace (pas de sillage) et des simulations "1W" (pour lesquelles la vitesse de l'océan n'a pas d'in-

fluence sur l'atmosphère). Les résultats des simulations sont en accords avec les travaux et les observations précédemment réalisés, et confirment que le sillage atmosphérique est le principal processus générant des tourbillons océanique dans le lit de l'île. Il est aussi montré que la vorticité est injectée directement par le rotationel du vent, mais aussi par la force du vent perpendiculaire au gradient d'épaisseur de la couche de surface océanique. De plus, la couche limite de friction horizontal (au niveau de l'île) semble conduire à des tourbillons plus intense à la submesoéchelle, pour les plus grands nombres de Reynolds.

Abstract

This thesis considers air-sea interaction, due to momentum exchange, in an idealized but consistent model. Two superposed one-layer fine-resolution shallow-water models are numerically integrated. The upper layer represents the atmosphere and the lower layer the ocean. The interaction is only due to the shear between the two layers. The shear applied to the ocean is calculated using the velocity difference between the ocean and the atmosphere. The frictional force between the two-layers is implemented using the quadratic drag law. Three idealized configurations are explored.

First, a new mechanism that induces barotropic instability in the ocean is discussed. It is due to air-sea interaction with a quadratic drag law and horizontal viscous dissipation in the atmosphere. I show that the instability spreads to the atmosphere. The preferred spatial scale of the instability is that of the oceanic baroclinic Rossby radius of deformation. It can only be represented in numerical models, when the dynamics at this scale is resolved in the atmosphere and the ocean. In one-way interaction the shear applied to the atmosphere neglects the ocean dynamics, it is calculated using the atmospheric wind, only. In two-way interaction it is opposite to the shear applied to the ocean. In the one-way interaction the atmospheric shear leads to a barotropic instability in the ocean. The instability in the ocean is amplified, in amplitude and scale, in two-way interaction and also triggers an instability in the atmosphere.

Second, the air-sea interaction at the atmospheric synoptic and mesoscale due to momentum transfer, only, is considered. Experiments with different values of the surface friction drag coefficient are performed, with a different atmospheric forcing from the first configuration, that leads to a turbulent dynamics in the atmosphere and the ocean. The actual energy loss of the atmosphere and the energy gain by the ocean, due to the interfacial shear, is determined and compared to the estimates based on average speeds. The correlation between the vorticity in the atmosphere and the ocean is determined. Results differ from previous investigations where the exchange of momentum was considered at basin scale. It is shown that the ocean has a passive role, absorbing kinetic energy at nearly all times and locations. Due to the feeble velocities in the ocean, the energy transfer depends only weakly on the ocean velocity. The ocean dynamics leaves nevertheless its imprint in the atmospheric dynamics leading to a quenched disordered state of the atmosphere-ocean system, for the highest value of the friction coefficient considered. This finding questions the ergodic hypothesis, which is at the basis of a large number of experimental, observational and numerical results in ocean, atmosphere and climate dynamics.

The last configuration considers the air-sea interaction, due to momentum exchange, around a circular island. In todays simulations of the ocean dynamics, the atmospheric forcing fields are usually too coarse to include the presence of smaller islands (typically < 100km). In the calculations presented here, the island is represented in the atmospheric layer by a hundred fold increased drag coefficient above the island as compared to the ocean. It leads to an increased atmospheric vorticity in the vicinity and in the wake of the island. The influence of the atmospheric vorticity on the ocean vorticity, upwelling,

turbulence and energy transfer is considered by performing fully coupled simulations of the atmosphere-ocean dynamics. The results are compared to simulations with a constant, in space and time, atmospheric forcing (no wake) and simulations with one-way coupling only (where the ocean velocity has no influence on the atmosphere). Results of our simulations agree with previous published work and observations, and confirm that the wind-wake is the main process leading to mesoscale oceanic eddies in the lee of an island. It is shown that vorticity is injected directly by the curl of the wind stress, but also by wind stress orthogonal to the gradient of the oceanic surface-layer thickness. Furthermore, the importance of the horizontal boundary layer friction (at the island), in higher Reynolds number simulations, leading to intense submesoscale vortices, is evaluated.

Contents

List of Figures

List of Tables

Chapter 1

Introduction

1.1 Air-sea interaction

The air-sea interface covers around 70 % of the Earth's surface. It is of great importance to the physics and the biology of the ocean and the atmosphere. Air-sea interactions are key to understanding both the oceanic and the atmospheric circulation, and is therefore important for weather forecasting and for the study of climate variability. This interface is the location of numerous complex processes which mainly consist in the exchange of heat, momentum, fresh water and other chemical substances, as it is shown in the figure 1.1.

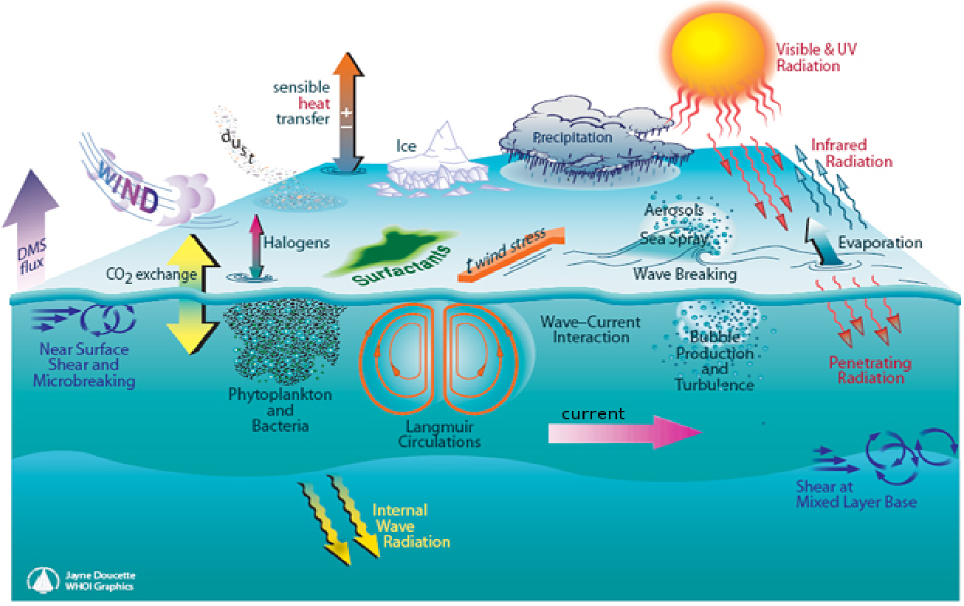

Figure 1.1: Processes operating at the air-sea interface *(Illustration by Jayne Doucette, Woods Hole Oceanographic Institution, WHOI [2013])*

The interaction between the two elements includes material exchange (gases, fluids, particles and organisms). The sources and sinks of material for the ocean are naturally water (rainfall, evaporation), but also the particles (airborne dust, mineral or organic), and finally atmospheric gases, which are either dissolved in water (depending on the temperature, atmospheric pressure, and the water chemical composition), or further absorbed by biological processes (CO2). These exchanges of different kinds are dependent on the physical properties, because the surface temperature, the sea state and the wind play an important role in the variation of most of the fluxes. None of these processes will be considered in this thesis. I focus on the exchange of momentum only. Nevertheless, observations and research considering the study of chemical and biological exchanges between the atmosphere and the ocean are essential to following the global carbon cycle (which is of a great interest to global warming and climate change).

1.1.1 Scales

Before proceeding, I would like to clear up the definition of the scales considered in the sequel, to clarify the concepts and the discussion. Air-sea interaction interferes in the dynamics of the ocean and the atmosphere at wide ranges of scales in time and space. In time, it involves short scales of the droplets dynamics (<1 second) to the diurnal cycle, to the El Nino phenomenon (a few years), up to the climate scale of thousands of years (fig 1.2). In space, sea spray involves scales smaller than 10^{-3}meters, hurricanes involve scales up to 10^{5} meters, and the forcing of the basin scale circulation spreads over 10^{7} meters.

Transfers of momentum and heat occur within the atmosphere, the ocean and across the air-sea interface on all of these range of space and time scales (fig 1.2). One characteristic of physical oceanography and meteorology is the overlap between the various physical processes. For example, processes occurring on small and intermediate scales influence the motion, temperature, and other properties of the large scale circulation and vice-versa. A complete understanding of the large-scale oceanic and atmospheric circulation require a consideration of all the physical processes at all time and space scales occurring in the ocean and the atmosphere and at the air-sea interface.

It is useful for the following to notice that all these processes can be indexed in five main classes of scale: the microscale, the small-scale, the mesoscale, the synoptic-scale and the planetary scale (fig 1.2), defined at the beginning of the 19th century. The synoptic-scale is defined in the American Meteorological Society's Glossary of Meteorology (AMS [2015]) as referring to "meteorological data that are obtained simultaneously over a wide area in order to present a nearly instantaneous snap-shot of the state of the atmosphere". Initially it does not define a precise scale, but is now a term used to describe the scale of large-scale weather systems (the only types of meteorological phenomena that could be resolved regularly by the coarse resolution observing platforms of the middle of the 19th century). It ranges in size from several hundred kilometers to a few thousand kilometers including such phenomena as cyclones, anticyclones and tropical cyclones. This scale can be estimated by the first baroclinic Rossby radius of deformation of the atmosphere (a typical characteristic scale in meteorology).

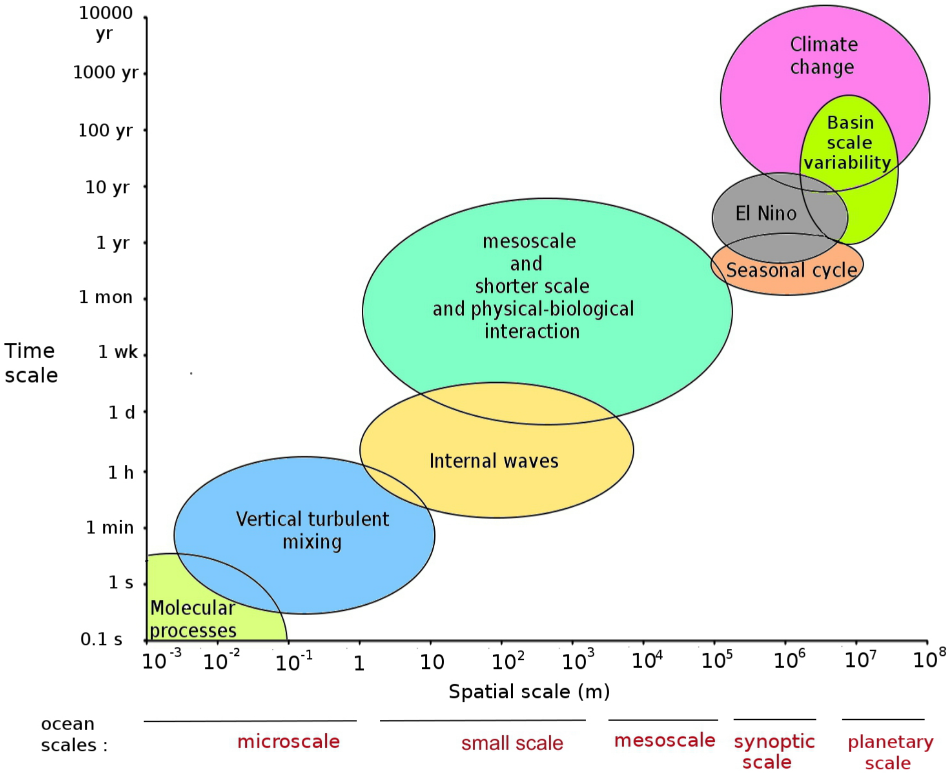

Figure 1.2: Scale definitions and the characteristic time and horizontal length scales of a variety of processes.

In the classification of the American Meteorological Society's Glossary of Meteorology (AMS [2015]), the microscale is reserved for horizontal scales smaller than 2 kilometers in the atmosphere. In the ocean, it is divided in microscale used in reference to phenomena having a scale of a few meters or less and small-scale for phenomena with a scale of few meters to a few kilometers.

The term mesoscale has been defined in order to describe phenomena smaller than the synoptic scale but larger than the microscale. Today the mesoscale in the American Meteorological Society's Glossary of Meteorology (AMS [2015]) is used for atmospheric phenomena having horizontal scales ranging from a few kilometers to a few hundred kilometers, including convective cells, thunderstorms, fronts, precipitation bands in tropical and extra-tropical cyclones... It is important to highlight that the term mesoscale in oceanography is, in terms of dynamical properties, the equivalent of the synoptic-scale for the atmosphere. It can be estimated thanks to the first baroclinic Rossby radius of deformation of the ocean. The mesoscale variability, in the ocean, generally refers to ocean signals with space scales of a few tens of kilometers to several hundreds of kilometers.

Scales larger than the synoptic scale are denoted planetary scale or basin scale (in the ocean).

1.1.2 Role of the ocean

Through their fluid motions, their high heat capacity, and their ecosystems, the oceans play a central role in shaping the Earth's climate and its variability. The feedback of the ocean on climate (e.g. increasing mean temperature, change in sea level), may have profound affects on ecosystems through habitat changes and on human society (trade, offshore industry, reserves in fish and minerals). To understand all energy and material transfers between the atmosphere and the ocean, quantifying and studying their time evolution is an important issue to improving our comprehension and the prediction of the climate system and the processes involved. One of the biggest challenges given to the scientific community, at the beginning of the 21st century, marked by the consequences of global warming and the turning in future energy choices, is to assign liability to each of the climate components and understand how they interact. The examples below, show that for all domains of climate dynamics (seasonal forecasting, climate scenarii) and also for meteorology, natural hazards, and marine resources; the mechanisms at the air-sea interface are essential.

The oceans are a major component of the climate system. Their role is not only to be a reservoir of water but also of heat. Indeed, the thermal inertia of the water is higher than each of the air and of the soil. The ocean as a huge heat capacity per volume which is about 4000 times larger than that of the atmosphere. Absorbing about twice as much of the sun's radiation as the atmosphere or the land surface. The ocean's thermohaline circulation allows water from the surface to be carried into the deep ocean, where it is isolated from atmospheric influence and hence, it may sequester heat and CO2 for periods up to a thousand years or more. It is a significant component of heat and carbon dioxide redistribution across the globe. Changes in this circulation can have major impacts upon the global and regional climate (e.g. Wood et al. [2003]).

The oceans at shorter time scale (few years) and smaller spatial scale ($\simeq$kilometers) damp temperature fluctuations and has a dynamic role as well. Ocean currents move vast amounts of heat across the planet (roughly the same amount as the atmosphere does). But in contrast to the atmosphere, the oceans are confined by land masses, so their heat transport is more localized and channeled into specific regions. For example, eddies are the principal mechanism for the transport of heat across strong currents, as the Gulf Stream or the Kurushio and they lead to slow down the winter cooling, and soften latitude contrasts (temperate climate up to 50 ° N latitude on the western edges of continents). Eddies can bring energy and momentum back into the mean flow and contribute to drive the deep ocean circulation. They also transport heat, carbon, and nutrients as they propagate in the ocean, and play a significant role in the global budgets of these quantities.

On smaller scales (about few days and few hundred of kilometers), the ocean contributes to the formation of extreme events like tropical cyclones. For tropical cyclones, the ocean is the main source of humidity and heat. It is favored if the oceanic mixed layer provides thermal energy for its development and maintenance, i.e an oceanic mixed layer with high temperatures (generally$>$ 26C degrees) and a consistent depth. The mixing induced by tropical cyclones in the ocean can play an important role in driving the general circulation of the ocean and so affect the climate (Emanuel [2001]). The air-sea retro-action can also lead to the dimming or the death of a cyclone. The upwelling and the thinning of thermal reservoirs can destruct the thermocline, and lead to colder sea surface temperature (SST) which reduces cyclone intensity if its displacement is slow (Bender et al. [1993]). Cyclones also lead to extreme wind conditions at the surface which can form a large amount of spray near the surface, cutting the heat flux efficiency and isolating the cyclone of its energy source. Quantifying the air-sea exchange of energy and mass, especially during high winds, is critical to improving the predictive capability of storm forecasting and climate-change models.

During the last sixty years the idea that the ocean temperature fluctuations can influence atmospheric circulation at small scales (few tens to hundred of kilometers) grew. Until recent years the influence of the ocean on the atmosphere has only been studied at large scales. The surface winds response to SST, at scales of about a few tens or hundreds of kilometers, have become evident over the past decade from simultaneous satellite measurements of SST and surface winds. They have revealed that ocean-atmosphere interaction is fundamentally different on oceanic mesoscales (order of tens to hundred kilometers) than at synoptic-scale (order of thousand kilometers) (Chelton and Xie [2010]). At large scales (synoptic-scale) an anomaly of positive temperature in the atmosphere is usually connected to a heat flux from the atmosphere into the ocean. At smaller scales (mesoscale) such anomaly is associated with a heat flux from the ocean to the atmosphere. Much of the small scale variability in the wind stress field are assigned to SST modification of low level winds through the influence of air sea-heat flux on the marine atmospheric boundary layer (Chelton et al. [2004]). Following the studies performed on the SST, its influence is now included in ocean-atmosphere coupled models. Currently, studies concerned with the influence of the ocean on the atmosphere are made considering SST induced processes but not the involvement of surface ocean currents, that remains unexplored and unknown while they may have an important role in the air-sea interaction, as I demonstrate in this work. In this thesis, I am going to consider only the momentum energy exchanges between the ocean and the atmosphere.

1.2 Modeling of air-sea interaction

Although a strong effort was put towards determining air-sea interaction, a lot of work needs to be accomplished. Conventional technology has provided only limited observations under high-wind conditions and few observations at high latitude where exchanges are particularly strong. Observations and analytical calculations are not sufficient to understand all the processes in the air-sea interaction. The numerical model is today a decisive stage in scientific research. Numerical models are an essential tool to study the future development of our environment, and understand the physical processes.

The ocean and the atmosphere are two fluids which obey the same dynamic laws. Nevertheless the air and water properties are very different and confer to each one its own dynamics. The water is around 1000 times denser than the air and it can stock 4000 times more heat for a same volume. One of the main difficulties of studying air-sea interaction is the difference in characteristic time and length scales between the global atmospheric and oceanic circulation. The first baroclinic Rossby radius of deformation, which is the characteristic horizontal scale, of the ocean (few tens of kilometers) is small compared to the atmospheric counter part (order of few hundreds of kilometers).

For example in the atmosphere, the cyclones and anti-cyclones at mid latitude have typical horizontal scales of few thousand kilometers, whereas eddies and meanders in the ocean have dimensions from few kilometers to hundred kilometers. The difference in the characteristic time scale is also important, indeed it takes a long time to alter the global oceanic circulation while the large scale atmospheric circulation evolves rapidly. The atmospheric dynamics at the synoptic scale evolves with a characteristic time scale of few days whereas the global gyres circulation in the ocean has a typical time scale from about a few months to a few years. Moreover oceanic anomalies persist much longer than its atmospheric source, and may in turn affect the atmosphere. The differences of scale of spatial and temporal variations between the two fluids makes it complex to study the exchange processes in models.

The ocean is not a homogeneous surface for the atmosphere, even if the heterogeneity is less important than that of the continents with the mountains and vegetation. These disparate characteristic time and length scales, lead to study the two fluids independently in the past. Today a lot of ocean-atmosphere coupled-models exist for global and large scale simulations. They typically have resolutions coarser than several tens of kilometers for the atmosphere and a few tens of kilometers for the ocean. They have been created to resolve questions about climate evolution or seasonal forecasting. Nevertheless only few oceanic models are coupled with regional atmospheric models with fine spatial and temporal resolution. This is based on the assumption that the time scales of variation in the ocean are lower than the time scales of atmospheric phenomena. But in intense atmospheric events or situations for closed basins, the characteristics of the ocean surface can change on faster time scales.

The atmospheric sciences in recent decades have greatly benefited from studies at process interfaces: atmosphere-continent and atmosphere-ocean. These have allowed a better quantification of energy exchanges (momentum and heat) and matter exchanges (water and chemical components) between the different compartments and also an improvement in their representation in numerical modeling of a single compartment or coupled modeling. Nevertheless coupling remains a weak point in the realistic modelization (IPCC [2007]).

Ocean-atmosphere coupled models must have a high spatial and temporal resolution. Models with high resolutions including more and more components are designed to provide the best representation of the system and its dynamics, but they are limited by their high computational cost. Atmosphere Ocean General Circulation Models (AOGCMs) are the most comprehensive models available and provide credible quantitative estimates of future climate change, particularly at continental and larger scales, but their computational cost limits the amount of simulations that can be done (IPCC [2007]). An idealized model is often better suited for answering to specific questions (IPCC [2007]).

1.3 Momentum fluxes

Winds a few meters above the surface tend to be of the order of several meters per second. Ocean currents are typically of the order of a few tens of centimeters per second. Hence, from the point of view of the atmosphere, the ocean can be considered, to first order, effectively as inert. From the point of view of the ocean, the atmosphere imposes a significant wind stress on its surface, and this forces currents in the ocean. Surface stress is one of the fundamental processes of the coupling between the atmosphere and the ocean. Indeed, the mechanical energy input to the ocean by atmospheric winds is known to be the dominant source of mechanical energy for driving the ocean circulation. Heating-cooling and precipitation-evaporation at the ocean surface are also important for the ocean circulation, because they create density differences influencing the ocean and atmosphere dynamics, but I do not consider them in this thesis. In existing ocean-atmosphere coupled models the ocean is considered motionless and bottom friction of the atmosphere is calculated from atmospheric velocities only. Since 2003, satellite scatterometer observations have shown that current induced features are visible in the wind stress curl (Chelton et al. [2004]). This is important for atmosphere and ocean circulation modeling. Indeed studies (Duhaut and Straub [2006], Scott and Xu [2009]) have found that calculations of wind power input to the ocean should depend on the relative motion between the atmosphere and the ocean and not on the velocity of the atmosphere alone. The surface shear stress τ, should be parametrized as a function of the difference between wind and ocean velocities. Because they did not account for the effects of ocean currents on the wind stress, numerical weather prediction models until few years ago, did not provide the true wind stress that drives the ocean circulation (Chelton et al. [2004]). Still today ocean currents are not taken into account in many simulations of the ocean dynamics and coupled ocean-atmosphere models and in almost all atmospheric simulations.

1.4 Aim and outline of this study

The aim of this PhD is to determine the air-sea interaction, due to momentum flux only, at the synoptic and the mesoscale, with an idealized but consistent model. Two superposed one layer fine resolution shallow-water models are used to study the coupled dynamics. The upper layer represents the atmosphere and the lower layer the ocean. The physical and the mathematical model to study the dynamics and its numerical implementation are described in the part I. The manuscript is then divided into three main parts which differ in the model configuration.

The first configuration (Part II), deals with the difference between simulations which use a consistent calculation for the wind stress applied to the atmosphere and those which neglect the oceanic velocity in the calculation of the shear between the ocean and the atmosphere. In one-way interaction the shear applied to the atmosphere neglects the ocean dynamics, it is calculated using the atmospheric wind, only. In two-way interaction it is opposite to the shear applied to the ocean. First, a semi-analytic one-dimensional model of two superposed fluid layers is used to explain the source and the physics of the barotropic instability induces in the ocean (Part II. Ch 6). Then the shallow water model is integrated numerically in a 1D (but two components) and 2D domain and compared with the semi-analytical model (Part II. Ch 8). In the one-way interaction the atmospheric shear leads to a barotropic instability in the ocean. The instability in the ocean is amplified, in amplitude and scale, in two-way interaction and also triggers an instability in the atmosphere.

In the second configuration (Part III), experiments with different values of the surface-friction drag-coefficient are performed. The actual energy loss of the atmosphere and the energy gain by the ocean, due to the inter-facial shear, is determined and compared to the estimates based on average speeds (Part III, Ch 12). The results concerning the correlation between the vorticity dynamics in the ocean and the atmosphere are presented in Part III, Ch 12. I also study the variability in space and time of the vorticity field in the atmosphere and the ocean as a function of the drag coefficient.

The last configuration (Part IV), deals with the influence of quadratic friction and atmospheric forcing on the oceanic mixed layer at mesoscale, in the presence of an island. Results confirm that the wind wake induced by the island is the main process which influences the ocean dynamics (Part IV, Ch 17.1). The transport around the island and the dynamic evolution and the injection and generation of vorticity are further investigate in the Part IV, Ch 17.2).

Part I

Two-layer reduced gravity shallow-water model

Chapter 2

Physical model

The model consist in two superposed homogeneous fluid layers, a shallow layer of the atmosphere above an ocean surface layer.
The physical model is illustrated by figure 2.1. For the following, the exponent “o“ refers to the ocean layer and the exponent “a” refers to the atmosphere layer.

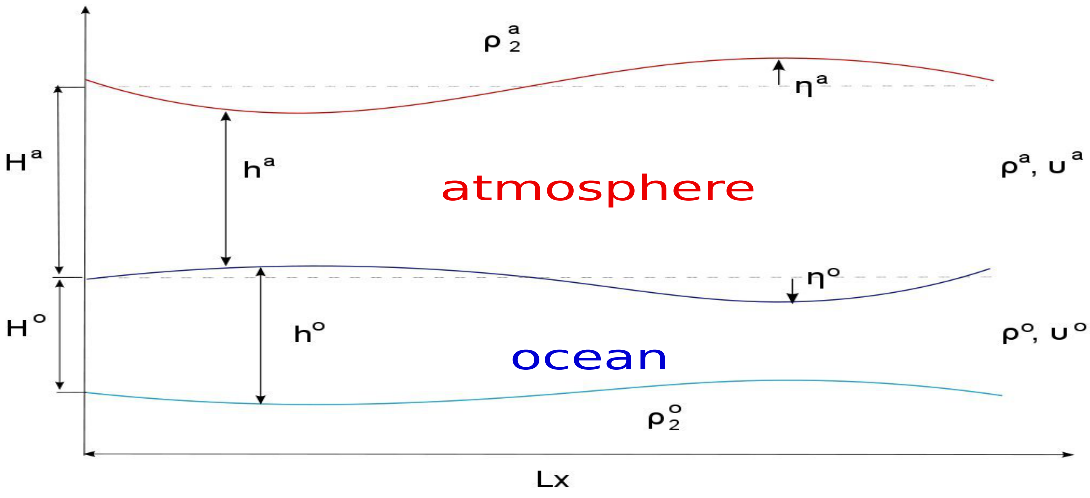

Figure 2.1: Scheme of the physical model

The average local thicknesses of the layers are H^o for the ocean and H^a for the atmosphere. The actual thicknesses denoted by $h^o(x, y, t)$, $h^a(x, y, t)$, can vary over time and space(Fig 2.1):

$$h^a(x, y, t) = H^a + \eta^a(x, y, t) \quad \text{and} \quad h^o(x, y, t) = H^o + \eta^o(x, y, t). \tag{2.1}$$

Where η^a, η^o represent only height perturbations of the top of the atmosphere layer and of the sea surface respectively. They depend on space and time.

The layers have an average density of $\rho^a = 1kg/m^3$ and $\rho^o = 1000kg/m^3$.

The ocean surface layer superposes a motionless layer of higher density ρ_2^o of infinite depth. Similarly, a motionless layer of atmosphere of density ρ_2^a superposes the shallow atmosphere layer. Thereby the two layers considered can be represented by reduced gravity models. The gravity g has just to be replaced by the reduced gravity of the ocean g^o and the atmosphere g^a in the dynamic equations:

$$g^o = \frac{\rho_2^o - \rho^o}{\rho_2^o} g = 2.10^{-2} m.s^{-2}, \tag{2.2}$$

where ρ_2^o is the density of the deep ocean layer and ρ^o the density of the ocean surface layer. In the same way : $g^a = 0.8 m.s^{-2}$.

The fluid motion considered extends over many days and so, the model must take into account the Earth's rotation. The Earth's rotation vector $\overrightarrow{\Omega}$ points northward along the south-north axis, and has a magnitude $\Omega = 2\pi/T = 7,45.10^{-5} s^{-1}$, where T is the Earth's rotation period. At each point of the surface of the Earth, Ω can be described by a vertical and an horizontal component. For large scale motion as here, the horizontal component of the rotation vector $\overrightarrow{\Omega}$ is usually neglected; this is called the traditional approximation. Thus, at latitude θ, the vertical component of the rotation vector is denoted by $f = 2\Omega \sin\theta$ and called the Coriolis parameter.

The Rossby radius can be calculated for the ocean and the atmosphere:

$$Rd^k = \frac{\sqrt{g^k h^k}}{f} \tag{2.3}$$

It represents the length scale at which rotational effects become as important as buoyancy effects in the evolution of the flow.

In this idealized model, the two layers are only linked by frictional forces at the interface, as atmospheric pressure variations have a negligible effect on the ocean dynamics and as height variations of the ocean surface have a negligible effect on the atmosphere. It is this friction term that I am going to vary between simulations by varying, the parametrization of the law, the drag coefficient, or the orography and the bathymetry.

Chapter 3

Mathematical model based on the reduced gravity shallow water equations

3.1 Hypothesis and equations

The physical model presented above can be described by a mathematical model based on the reduced gravity shallow water equations. The shallow water equations are the most widely used equations in geophysical and environmental fluid dynamics.

To use this mathematical model, I assume that:
- The atmosphere and the ocean are composed of two incompressible fluids.
- The atmosphere and the ocean are very flat because height scales are very small compared to length scales
- Density variations within one fluid are very low.

The shallow water equations which describe the dynamics of the ocean and atmosphere layers are written:

$$\begin{aligned} \partial_t u^k + u^k \partial_x u^k + v^k \partial_y u^k - f v^k + g^k \partial_x \eta^k &= \nu^k \nabla^2 u^k + F_x^k && (3.1) \\ \partial_t v^k + u^k \partial_x v^k + v^k \partial_y v^k + f u^k + g^k \partial_y \eta^k &= \nu^k \nabla^2 v^k + F_y^k && (3.2) \\ \partial_t h^k + \partial_x [h^k u^k] + \partial_y [h^k v^k] = 0, & && (3.3) \end{aligned}$$

where k=a or k=o.

The friction force applied to the atmosphere is the opposite of the friction force applied to the ocean:

$$\begin{pmatrix} f_x^o \\ f_y^o \end{pmatrix} = - \begin{pmatrix} f_x^a \\ f_y^a \end{pmatrix}.$$

The friction force F between the two layers in equations 3.1 and 3.2 can be defined by:

$$\begin{pmatrix} F_x^k \\ F_y^k \end{pmatrix} = \pm\frac{1}{\rho^k h^k}\begin{pmatrix} f_x \\ f_y \end{pmatrix}.$$

Where f_x and f_y are the surface forces depending on x and y axes.

I am going to study the dynamics with a quadratic friction law. Such law parametrizes the turbulent dynamics of the boundary layers. It is based on the turbulent law-of-the-wall stating that the average velocity of a turbulent flow at a certain point is proportional to the logarithm of the distance from that point to the "wall", or the boundary of the fluid region.

$$\begin{pmatrix} f_x \\ f_y \end{pmatrix} = \rho^a C_d |u| \begin{pmatrix} u^o - u^a \\ v^o - v^a \end{pmatrix},$$

with $|u| = \sqrt{(u^o - u^a)^2 + (v^o - v^a)^2}$.
C_d is the drag coefficient it can be calculated with an empirical formula (Jin [1982], Smith [1988]):

$$C_d = (0.8 + 0.065 \times u_{10}) \times 10^{-3}$$

where u_{10} is the typical atmospheric velocity at 10 meters height.

3.2 Dimensional analysis of the mathematical model

I am starting from the shallow water equations obtained in the previous section (3). Each parameter is adimensionalized:

$$\begin{aligned} x' &= \frac{x}{L} \quad \text{and} \quad y' = \frac{y}{L} \\ u^{k'} &= \frac{u^k}{u_0^k} \quad \text{and} \quad v^{k'} = \frac{v^k}{u_0^k} \\ t' &= tf \\ \eta^{k'} &= \frac{\eta^k}{H^k} \end{aligned}$$

assuming that L is a relevant lengthscale for the dynamics described.

The first equation adimensionalized (3.1) becomes:

$$\begin{aligned} u_0^k f \partial'_t u^{k'} + \frac{{u_0^k}^2}{L} u^{k'} \partial'_x u^{k'} + \frac{{u_0^k}^2}{L} v^{k'} \partial'_y u^{k'} - f u_0^k v^{k'} + \frac{g^k H^k}{L} \partial'_x \eta^{k'} &= \frac{\nu^k u_0^k}{L^2} \nabla^2 u^{k'} + F_x^k \\ \partial'_t u^{k'} + \frac{u_0^k}{fL} u^{k'} \partial'_x u^{k'} + \frac{u_0^k}{fL} v^{k'} \partial'_y u^{k'} - v^{k'} + \frac{g^k H^k}{u_0^k f L} \partial'_x \eta^{k'} &= \frac{\nu^k}{fL^2} \nabla^2 u^{k'} + F_x^k \\ \partial'_t u^{k'} + Ro^k (u^{k'} \partial'_x u^{k'} + v^{k'} \partial'_y u^{k'}) - v^{k'} + \frac{Ro^k}{{Fr^k}^2} \partial'_x \eta^{k'} &= \frac{Ro^k}{Re^k} \nabla^2 u^{k'} + F_x^k. \end{aligned}$$

The second equation adimensionalized (3.2) gives:

$$\partial'_t v^{k'} + Ro^k(u^{k'}\partial'_x v^{k'} + v^{k'}\partial'_y v^{k'}) - u^{k'} + \frac{Ro^k}{{Fr^k}^2}\partial'_y \eta^{k'} \quad = \quad \frac{Ro^k}{Re^k}\nabla^2 v^{k'} + F^k_y.$$

The third equation (3.3) becomes:

$$\begin{aligned} H^k f \partial'_t h^{k'} + \frac{H^k u^k_0}{L}(\partial'_x u^{k'} h^{k'} + \partial'_y v^{k'} h^{k'}) = 0 \\ \partial'_t h^{k'} + \frac{u^k_0}{fL}(\partial'_x u^{k'} h^{k'} + \partial'_y v^{k'} h^{k'}) = 0 \\ \partial'_t h^{k'} + Ro^k(\partial'_x u^{k'} h^{k'} + \partial'_y v^{k'} h^{k'}) = 0 \end{aligned}$$

$Ro = u/fL$ is the Rossby number, $Fr = u/\sqrt{gH}$ is the Froude number, and $Re = uL/\nu$ is the Reynolds number.

The friction term adds other dimensionless numbers:

- for the Rayleigh friction: $\frac{\lambda}{f}$.
- for the Quadratic friction: $C_d u/fH^k$.

Another non dimensional parameters is the ratio of densities: ρ^a/ρ^o.

Chapter 4

Numerical model

4.1 Numerical grid

The numerical frame has only two horizontal dimensions x and y, and there are two layers in the vertical. The velocities u and v are z-independent, and obviously the thickness of the layers $H^k + \eta$ does not depend on z, thus there is no need to work with the vertical axis. The ocean and the atmosphere basins are represented by a square, of $L_x \times L_y$. Periodic boundary conditions are used in both horizontal directions (section 4.2). The numerical grid is regular and contains $n_x \times n_y$ points. Each grid point is characterized by a couple of integers i_x, i_y, with i_x= [1:n_x] and i_y= [1:n_y]. Spatial resolutions are the same in both directions, $\Delta x = L_x/n_x = \Delta y = L_y/n_y$. The horizontal components of the velocity u^k, v^k, and height variations η^k are calculated on each grid points. u^k is positive going eastwards and v^k is positive going northward. Variables u^k, v^k, η^k at time t and $t+\Delta t$ will respectively write u_o^k, v_o^k, η_o^k and u_n^k, v_n^k, η_n^k. The layers have kinematic viscosity coefficients ν^a and ν^o, which are constants in space and time.

4.2 Discretization of periodic boundary conditions

As in the second order scheme, values at points i+1 and i-1 are involved to calculate values at point i. At the boundaries values have to be provided. For this model, periodic boundary conditions are used. Every point that comes out of the field at a boundary reappears at its opposite side (Fig 4.1).

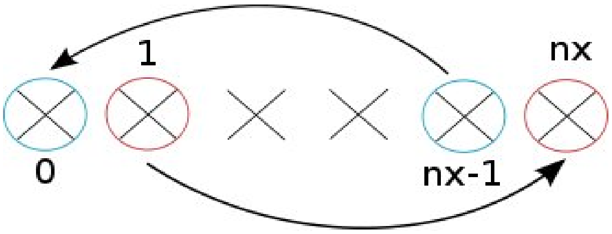

Figure 4.1: Scheme of the periodic boundary conditions in the x-direction

4.3 Stability of the numerical scheme

To ensure the stability of the numerical scheme, the Courant Friedrich Levy condition (CFL) must be satisfied. In order to avoid numerical instabilities, the time step Δt of the simulation must be inferior to the characteristic advection time scales. Indeed, the distance of wave propagation during a time step Δt must be smaller than the mesh size. Finally the model has to satisfy the condition:

$$\frac{c^k \Delta t}{\Delta x} \leq 1 \qquad \text{where} \quad c^k = \sqrt{g^k h^k} \qquad \text{(wave velocity)}$$

To improve accuracy I choose:

$$\sqrt{g^k h^k}\frac{\Delta t}{\Delta x} \leq 0.2$$

Since the thicknesses and the reduced gravities of the atmosphere and the ocean are very different, it is necessary to take a time step which respect the stability condition for both layers.

In the atmospheric layer, gravity wave propagation c^a is faster than in the ocean :

$$\begin{aligned} c^a &= \sqrt{g^a h^a} \\ c^o &= \sqrt{g^o h^o} \end{aligned}$$

so it is the atmospheric dynamics that sets the time-step.

4.4 Numerical implementation

4.4.1 Code (part II and part III)

In the two first configurations (part II and part III), the code is written in FORTRAN90.

The mathematical model is discretized with second order schemes.

Numerical schemes used here are based on the Taylor series. If a function f(x,y) has continuous derivatives up to the order n+1 then:

$$\begin{aligned} f(x,y) &= f(x_0,y) + \frac{f'(x,y)}{1!}(x - x_o) + \frac{f''(x,y)}{2!}(x - x_0)^2 \\ &+ \ ... + \frac{f^{(n)}(x,y)}{n!}(x - x_0)^n + O((x - x_0)^{n+1}). \end{aligned}$$

First I have to discretize all equations in space. To improve accuracy, the centered finite difference method is used for the space discretization. Thanks to the Taylor series, I calculate first and second order space derivatives:

$$\begin{aligned} f'(x,y) &= \frac{f(x+\Delta x,y)-f(x-\Delta x,y)}{2\Delta x}+O(\Delta x^2) \\ f''(x,y) &= \frac{f(x+\Delta x,y)-2f(x,y)+f(x-\Delta x,y)}{\Delta x^2}+O(\Delta x^2) \end{aligned}$$

A second-order Runge-Kutta time scheme is used for the time discretization. The Runge-Kutta 2 method consist in evaluating the function derivative at the middle time $t+\Delta t/2$ of the iteration,

$$\begin{aligned} f(t+\frac{\Delta t}{2}) &= f(t)+\frac{\Delta t}{2}F(t,f(t)) && With \quad F(t,f(t))=f'(t) \\ f(t+\Delta t) &= f(t)+\Delta t F(t+\frac{\Delta t}{2},f(t)+\frac{\Delta t}{2}) \end{aligned}$$

All values (u^k, v^k, η^k) are calculated in each points of the area.

The Fortran program was compiled with the Intel Ifort compiler. Then the compiled file was submitted on one of the LEGI calculators (servcalcul3) thanks to a job performed by the batch system OAR. All calculation are made in double precision. The runs presented have lasted up to 20 days. The simulation results were finally analyzed thanks to the Scilab, Matlab, and Paraview softwares.
The model has been parallelized with MPI and is then executed in the IDRIS calculator with finner spatial and temporal resolutions for the second configuration (part III). The model has been tested during my M2 internship by comparing with analytical simulations, and using different parametrization of the friction law (linear friction, quadratic friction, Ekman friction).

4.4.2 OpenFOAM code (part IV)

For the last configuration, I wrote a code in OpenFOAM to implemented an island.

OpenFOAM used an object-oriented techniques and is discretized by the finite volume method (Weller et al. [1998]). The OpenFOAM solver used here was developed according to the shallow-water Foam solver (Pilqvist [2010]). I added a second layer, the diffusion, and the friction between the two layers. The file was submitted on one of the LEGI calculators (servcalcul3). The runs have lasted up to 1 week. The simulations are then analyzed with paraFOAM.

Part II

A drag-induced barotropic instability in air-sea interaction (Moulin et al. [2014])

Chapter 5

Introduction

Air-sea interaction is a key process in the dynamics of the atmosphere, the ocean and the climate system. Many aspects of it are today not well understood. At the air-sea interface there is an exchange of heat, inertia and chemical substances, as carbon-dioxide and other gases. The understanding of the processes are hindered by the fact that air-sea interaction involves dynamics on a large range of scales, from the molecular motion to droplet dynamics to wave dynamics and braking, and up to the scale of weather systems, involving a large variety of physical, chemical and even biological processes. An explicit resolution of all these processes in numerical models of the dynamics is impossible, even in a far future. The important processes have thus to be parameterized in calculations of the atmosphere, ocean and climate dynamics.

Recent fine scale satellite observations of the sea surface show an abundance of dynamical features at the meso and sub-meso scale. The explanation of the origin, turbulent dynamics and fate of these structures represents a formidable problem of geophysical fluid dynamics. Furthermore, it was shown recently that the dynamics at these scales is not dynamically passive, but has a major impact on the scale-dependent physics of air-sea interaction due to their signature in the sea-surface temperature (Seo et al. [2008] and Chelton and Xie [2010] for a recent review).

In the present work we exclusively focus on the exchange of momentum. The exchange of heat is completely neglected here, which does not mean that we question its importance for the atmosphere, ocean and climate dynamics. In todays numerical models there are various ways and parameterizations to represent the exchange of momentum. They mathematically treat the atmosphere differently than the ocean. Concerning the atmosphere, a Dirichlet boundary condition is imposed, that means the wind is supposed to vanish at the surface, without considering the direct effect of ocean currents. For the ocean, a Neumann boundary condition is imposed, that is the shear of the atmosphere on the ocean is applied to the ocean. In calculations of air-sea interaction the resolution in the ocean is usually finer than in the atmosphere, as the first baroclinic Rossby radius of deformation, the synoptic scale, is one order of magnitude smaller than in the atmosphere. Such kind of mixed treatment, in the type of the boundary condition and the resolution, might be justified at large spatial scales and long time scales, but might not be siutable when the resolution, in both, the atmosphere and the ocean become ever finer. In the present paper we compare this "classical" implementation of the air-sea momentum exchange to a dynamically consistent implementation. We demonstrate that the results are substantially different and that a new instability arises in the atmosphere-ocean system.

When parameterizing the effect of small-scale turbulent friction at a solid boundary a quadratic drag law is used. Such a drag law dates back to the work of Prandtl and Schlichting [1934] and Schlichting and Gertsen [2000] and has been extensively studied since then (see Schlichting and Gertsen [2000]). All these investigations essentially confirming its robustness and its applicability to all fields of fluid dynamics. When the motion of the atmosphere and the ocean are considered a large volume of research is dedicated to the determination of the drag coefficient over various surfaces (Stull [1988]). When the sea surface is considered the drag coefficient depends on the sea-state, which itself is a function of various parameters (see *e.g.* Högström et al. [2013]). The robustness of the law itself seems above any doubt.

In chapter 6 we use a semi-analytic one-dimensional model of two superposed fluid layers to explain the source and the physics of the instability. Two cases are considered, translational and rotational invariant forcing. A shallow water model of the same physical model is introduced in chapter 7. The model is integrated numerically in a 1D and 2D domain. The former converges to a stationary state, while the latter develops instability. Results are presented in chapter 8 and discussed in chapter 9.

Chapter 6

One Dimensional Model

6.1 Atmospheric layer

The state of a shallow fluid layer of constant depth and subject to a large scale forcing $F(y)$, a constant drag coefficient and a viscous dissipation in the horizontal can be modeled by the following equation:

$$\frac{c_D}{H}|u(y)|u(y) - \nu\partial_{yy}u(y) = F(y), \tag{6.1}$$

where we have further supposed, that the flow is stationary, the Coriolis parameter is zero, that its velocity component in the y-direction is vanishing and that the velocity component in the x-direction, that is u, depends on y, only.

Note that the drag term and the viscous term, for a smooth velocity field, are of equal strength at a scale

$$l = \sqrt{\frac{\nu H}{u_0 c_D}}, \tag{6.2}$$

We show below, that this scaling is modified for the singular behavior at points of vanishing velocity.

If $F(y) = F_0 \cos(y/L)$ and $\nu = 0$ the analytic solution is:

$$u(y) = \operatorname{sgn}\left[\cos(y/L)\right] \sqrt{\frac{F_0 H}{c_D}|\cos(y/L)|} \tag{6.3}$$

which has a vorticity:

$$\zeta(y) = -\partial_y u(y) = \operatorname{sgn}\left[\cos(y/L)\right] \sqrt{\frac{F_0 H}{4L^2 c_D}\sin(y/L)\tan(y/L)} \tag{6.4}$$

The vorticity is singular at every point $y = (j + 1/2)\pi$, $\forall j \in \mathbb{Z}$. In the case of a non-vanishing viscosity the singularity disappears.

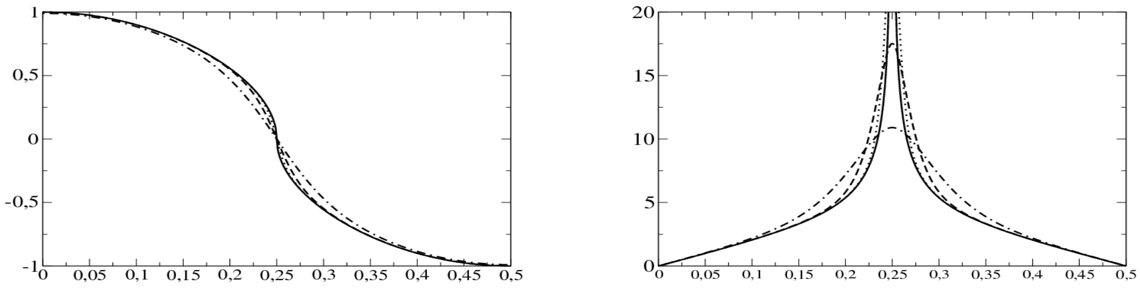

Figure 6.1: Velocity u (left) and vorticity (right) for $\nu = 0$ (full line), $\nu = 10^{-5}$ (dotted line) , $\nu = 10^{-4}$ (dashed line) and $\nu = 10^{-3}$ (dashed-dotted line), in the atmosphere. Only half of the domain is shown, rest can be continued by symmetry.

Equation (6.1) can be put in non-dimensional form by setting:

$$\tilde{\nu} = \frac{\epsilon}{c_D \, Re}, \tag{6.5}$$

with $\epsilon = H/L$ is the ratio of the layer thickness to a characteristic horizontal scale and $Re = u_0 L/\nu$ the Reynolds number based on the typical velocity scale u_0 and a turbulent viscosity ν. This leads to the non-dimensional equation:

$$|\tilde{u}(\tilde{y})|\tilde{u}(\tilde{y}) - \tilde{\nu}\partial_{\tilde{y}\tilde{y}}\tilde{u}(\tilde{y}) = \tilde{F}(\tilde{y}) \tag{6.6}$$

where all the $\tilde{.}$ variables are non-dimensional and of order one, except for the non-dimensional viscosity which is typically $\tilde{\nu} \ll 1$.

The solution for $\tilde{\nu} = 0$ is now $\tilde{u}(\tilde{y}) = \mathrm{sgn}(\cos y)\sqrt{|\cos y|}$ and $\tilde{\zeta}(\tilde{y}) = \mathrm{sgn}(\cos y)\sqrt{\sin y \tan y}/2$. We did not find an analytical solution for $\tilde{\nu} \neq 0$. The numerical solutions for different values of $\tilde{\nu}$ are shown in fig. 6.1. For the smaller values of the viscosity the solution in the velocity field are almost indistinguishable from the case of a vanishing viscosity. The vorticity however goes to infinity with a vanishing viscosity. This singularity is avoided with a non-vanishing viscosity. In the limit of vanishing viscosity, the behavior at the point of vanishing velocity is proportional to $\sqrt{y}$, the drag term is $\sqrt{y}^2 = y$, the viscous term is $-\tilde{\nu}\partial_{yy}\sqrt{y} = \tilde{\nu}y^{-3/2}/4$. By equating both terms one finds that they are of equal strength at a scale $l = (\tilde{\nu}/4)^{2/5}$. The maximum vorticity is given by $\zeta_{\max} = u/l = \sqrt{l}/l = l^{-1/2} = (\tilde{\nu}/4)^{-1/5}$. We measured numerically the characteristic length scale l_g as the distance between the inflection point of $\zeta(y)$ and the maximum of $\zeta(y)$ in numerical solutions of eq. (6.6). The results are given in fig. 6.2, where a clear scaling law behavior is exposed, for the lower values of the viscosity. The scaling law exponents agree perfectly with the above predictions. If we define a local atmospheric Reynolds number base on the distance between the inflection points we get $Re^a = ul/\tilde{\nu} = l^{1/2}l/\tilde{\nu} = (\tilde{\nu}/4)^{6/10}/\tilde{\nu} \propto \tilde{\nu}^{-2/5}$

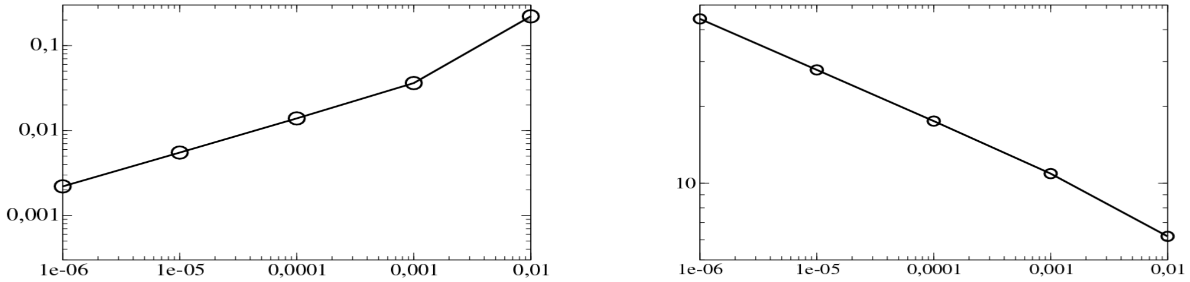

Figure 6.2: Length scale l_g in the atmosphere as a function of the viscosity $\tilde{\nu}$ (left). For the 4 lower values of the viscosity $\tilde{\nu}$ the scaling is $l_g \propto \tilde{\nu}^{2/5}$. Maximum value of the vorticity $\zeta_{\max}$ in the atmosphere as a function of the viscosity $\tilde{\nu}$. For the 4 lower values of the viscosity $\tilde{\nu}$ the scaling is $\zeta_{max} \propto \tilde{\nu}^{-1/5}$

6.2 Oceanic layer

In the stationary case and with a vanishing viscosity in the atmosphere, the force applied to the atmosphere equals the force transmitted to the ocean at every point. The balance is local in the horizontal. This is no longer true for a non-vanishing viscosity and the functional form of the velocity field in the atmosphere and the ocean differ. The momentum balance in the atmosphere is:

$$F^{ao} - \nu^a \partial_{yy} u^a = \tilde{F}^a, \tag{6.7}$$

Where $\tilde{F}^a$ is the force applied to the atmospheric layer by the (exterior) pressure gradient and F^{ao} the force transmitted to the ocean. We can further suppose that the (eddy) viscosity is many orders of magnitude smaller in the ocean, than in the atmosphere. Indeed, the eddy viscosity can be estimated using a mixing length approach $\nu = Lu$, where L and u are a typical length and velocity scale, respectively (Prandtl [1925], Vallis [2006]). The first baroclinic Rossby radius of deformation is at least an order of magnitude smaller in the ocean than it is in the atmosphere and the same is true for the characteristic velocities. The estimated eddy viscosity in the ocean is more than two orders of magnitude smaller than its atmospheric counter-part. When the ocean layer is subject to the force F^{ao} at its surface and to a linear damping at its lower boundary, its velocity and vorticity are shown in fig. 6.3. Please note that the oceanic vorticity profile shows three extrema, instead of only one for the atmosphere, this is of importance for the stability of the flow as vorticity maxima are key to barotropic instability as shown by Rayleigh's and Fjortoft's criterion for barotropic instability (see Vallis [2006], Paldor and Ghil [1997]). Furthermore, the distance between the maxima, which is the important length scale for instability is governed by the atmospheric (eddy) viscosity. This leads to an oceanic Reynolds number

$$Re^o = \frac{u^o \nu^a}{u^a \nu^o} Re^a \tag{6.8}$$

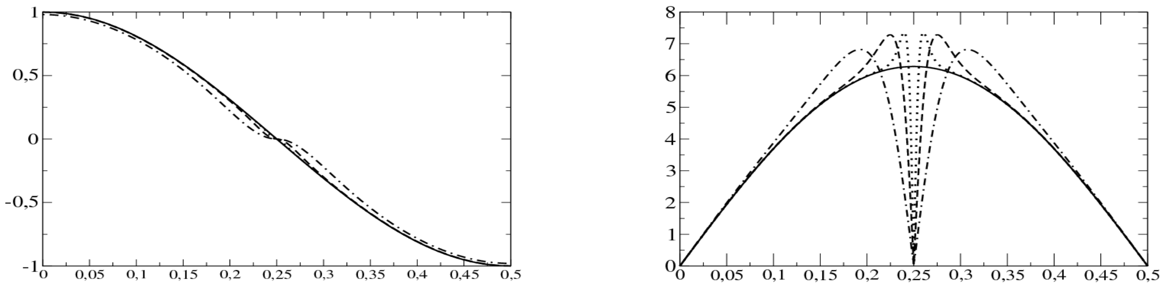

Figure 6.3: Velocity u (left) and vorticity (right) for $\nu = 0$ (full line), $\nu = 10^{-5}$ (dotted line), $\nu = 10^{-4}$ (dashed line) and $\nu = 10^{-3}$ (dashed-dotted line), in the ocean. Only half of the domain is shown, rest can be continued by symmetry.

which is larger than the atmospheric Reynolds number.

6.3 Point symmetry

When the forcing and the initial conditions are point symmetric all variables initially depend only on the distance r from the center of symmetry. This property is conserved in the absence of instability. In this case the non-divergent dynamics in the constant depth layer is best described by a stream function with:

$$u = -\partial_y \Psi \quad \text{and} \quad v = \partial_x \Psi \tag{6.9}$$

The equations for a stationary solution are:

$$-|\partial_r \Psi(r)| \partial_r \Psi(r) + \tilde{\nu} \partial_r \left(\frac{1}{r} \partial_r (r \partial_r \Psi(r)) \right) = r \tag{6.10}$$

where we used:

$$\partial_x f(r) = \frac{x}{r} \partial_r f(r) \quad \text{and} \quad \nabla^2 f(r) = \frac{1}{r} \partial_r \left(r \partial_r f(r) \right) \tag{6.11}$$

In the case of a vanishing viscosity the solution is completely local and we obtain the same dependence as in the case of an axial symmetry $\partial_r \Psi(r) = \sqrt{r}$. The scaling behavior for the viscous case is also the same $l = (3\tilde{\nu}/2)^{2/5}$, with a different numerical prefactor.

When viscosity in the atmosphere is included, then, again, the forcing transmitted to the ocean creates a vorticity extrema in a ring around the point of vanishing velocity, at which an extrema of opposite vorticity reside.

Chapter 7

Shallow-water model

7.1 Physical model

The model consists of two superposed homogeneous fluid layers, a shallow layer of the atmosphere above an ocean surface layer. The average thicknesses are respectively $H^a = 500m$ and $H^o = 200m$. The actual layer thicknesses $h^a(x, y, t)$, $h^o(x, y, t)$ vary over time and space. The ocean surface layer superposes a motionless layer of higher density and of infinite depth. Similarly a motionless layer of air of a lesser density superposes the shallow atmosphere layer. Layers have an average density of $\rho^a = 1kg/m^3$ and $\rho^o = 1000kg/m^3$. The fluid motion considered extends over many days and so, the model must take into account the Earth's rotation. Using the f-plane approximation we set the Coriolis parameter $f = 10^{-4}\mathrm{s}^{-1}$, a typical value at mid-latitudes.

7.2 Mathematical model

This physical model can be described by the reduced gravity shallow water equations:

$$\begin{aligned}
\partial_t u^k + u^k \partial_x u^k + v^k \partial_y u^k - f v^k + g^k \partial_x h^k &= \nu^k \nabla^2 u^k + F_x^k && (7.1)\\
\partial_t v^k + u^k \partial_x v^k + v^k \partial_y v^k + f u^k + g^k \partial_y h^k &= \nu^k \nabla^2 v^k + F_y^k && (7.2)\\
\partial_t h^k + \partial_x [h^k u^k] + \partial_y [h^k v^k] = \tilde{F}_h^k, & && (7.3)
\end{aligned}$$

Where $k = a, o$ stands for the atmosphere and the ocean, respectively. The parameters g^a and g^o are the reduced gravity of the atmosphere and of the ocean (i.e., the gravitational acceleration multiplied by the fractional density difference between the two layers). They are respectively set to $0.8m/s^2$ and $2.10^{-2}\ m/s^2$. The restoring force $\tilde{F}_h^k$ in the atmosphere and ocean acts on the layer-thickness.

The typical horizontal scale is the Rossby radius of deformation $Rd^k = \sqrt{g^k H^k}/f$. It is one order of magnitude smaller in the ocean where $Rd^o = 20km$ than in the atmosphere where $Rd^a = 200km$. The domain size is $L_x = L_y = 1000\mathrm{km}$ and there are periodic boundary conditions in both horizontal directions. In the absence of forcing and friction the potential vorticity (PV):

$$q^k = \frac{\zeta^k + f}{h^k} \quad \text{with} \quad \zeta^k = \partial_x v^k - \partial_y u^k, \tag{7.4}$$

is conserved by the flow. The initial atmospheric height variation (A.1) is defined by the leading four terms of the Fourier series of the sawtooth function in the y-direction.

$$\eta_o^a(x,y) = 300m \times (sin(2\pi y/L_y) - \frac{1}{3}sin(4\pi y/L_y) + \frac{1}{5}sin(6\pi y/L_y) - \frac{1}{7}sin(8\pi y/L_y))$$

The initial velocity field is calculated using the geostrophic equilibrium, so narrow jet in the x-direction depending only on y-direction is imposed on the atmosphere.

A restoring acts to force the average (in the x-direction) of the atmospheric layer thickness projected on the sawtooth profile towards its initial value. To this end, the projection is compared to its initial value and a multiple of the initial profile is added or subtracted to restore towards the initial amplitude of the projected mode. Such kind of (large-scale) restoring affects the large scale dynamics without directly influencing the small scales which can evolve more freely. The restoring time is two days. The variations of layer thickness in the ocean layer are locally and linearly damped to zero with a damping time of 1000 days, in order to not disturb the air-sea interaction.

The two layers are only linked by frictional forces at the interface, parameterized by a quadratic drag law. The frictional acceleration between the two layers (see eqs. (7.1) and (7.2)) is defined by:

$$\begin{pmatrix} F_x^k \\ F_y^k \end{pmatrix} = \pm \frac{1}{\rho^k h^k} \begin{pmatrix} f_x^k \\ f_y^k \end{pmatrix}. \tag{7.5}$$

Where f_x and f_y are the surface forces depending on x and y. The shear applied to the ocean is calculated using the velocity difference between wind and ocean current.

$$\begin{pmatrix} f_x^o \\ f_y^o \end{pmatrix} = \rho^a C_d |u| \begin{pmatrix} u^o - u^a \\ v^o - v^a \end{pmatrix}, \tag{7.6}$$

with $|u| = \sqrt{(u^o - u^a)^2 + (v^o - v^a)^2}$. The drag coefficient is constant in our calculations, $C_d = 8.10^{-4}$ a classical value (Stull [1988]).

In one way interaction, the shear applied to the atmosphere neglects the effects of ocean currents, the ocean is a rough motion-less surface:

$$\begin{pmatrix} f_x^a \\ f_y^a \end{pmatrix} = \rho^a C_d \sqrt{(u^a)^2 + (v^a)^2} \begin{pmatrix} -u^a \\ -v^a \end{pmatrix}. \tag{7.7}$$

In two way interaction, the shear applied to the atmosphere is the opposite to the shear applied to the ocean.

7.3 Numerical model

The ocean and the atmosphere basins are represented by a rectangle, of $L_x \times L_y$. Periodic boundary conditions are used in both horizontal directions. The numerical grid is regular and contains $n_x \times n_y$ points. Fine spatial resolutions $\Delta x = L_x/n_x = \Delta y = L_y/n_y$ are employed to well resolved the horizontal scales. We choose $n_x = n_y = 512$ and $L_x = L_y = 1000km$ for the 2D shallow water model. For the one-dimension-two-component (1D-2C) geometry we have $L_x = 1000km/512, L_y = 1000km$ and $n_x = 1, n_y = 512$. The horizontal components of the velocity u^k, v^k, and height variations η^k are calculated on each grid point. The eddy viscosity of the layers are $\nu^a = 100m^2/s$ and $\nu^o = 1m^2/s$, which are constants in space and time.

A second order centered finite difference method is used for the space discretization and a second-order Runge-Kutta scheme is used for the time discretization. The time resolution is constraint by the CFL condition. As atmospheric waves are ten times faster than oceanic waves, it is the CFL condition for the atmosphere that sets the minimum time step $\Delta t = 15$s to well resolve the temporal evolution of the atmospheric dynamics.

Chapter 8

Results

We integrate the numerical model in a 1D-2C and a 2D geometry. In the former no instability can develop and it is thus perfect to evaluate the effect and the evolution of instability that develops in the latter. Without instability there is a perfect agreement between the two simulations as forcing and damping are independent of the x-direction. In all results presented, the model was run for 2000 days and averages were calculated from the daily snapshots from day 1000 to 2000.

8.1 One-dimensional Two-component (1D-2C) model

No instability develops in this geometry and the dynamics converges towards a stationary state. The potential vorticity for the atmosphere and the ocean along the y-axis, for one-way or two-way interaction are shown in the fig. 8.1.

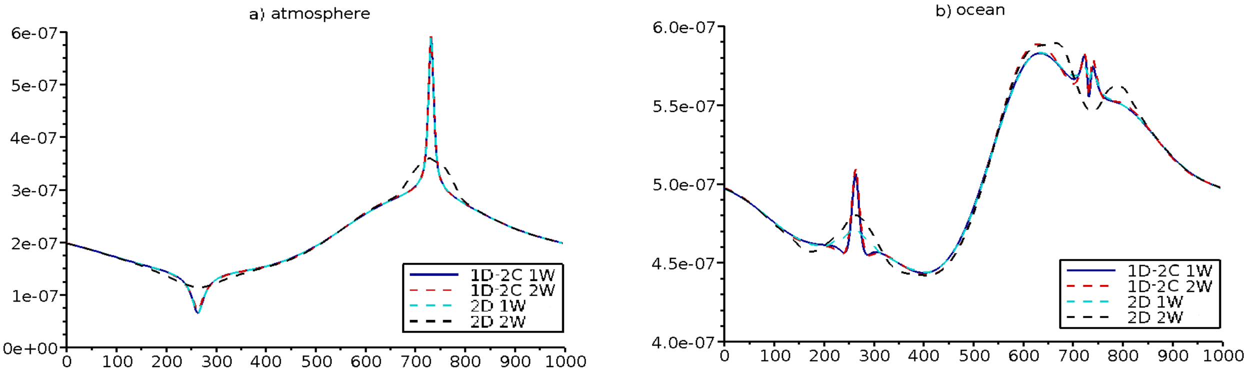

Figure 8.1: Potential vorticity (in $s^{-1}.m^{-1}$) averaged in time and x-direction, along the y-axis, in the atmosphere (left) and in the ocean (right), for the four cases considered, as labeled

The quadratic drag law leads to a widening of the atmospheric jet because it acts stronger on the faster velocities. In the atmosphere, the balance between the forcing term, the drag term and the viscous term leads to vanishing velocities and a strong velocity gradient at $y = 260$km and $y = 740$km. This is the analogue to the situation observed in the 1D model of chapter 6. These characteristics of the velocity field, give rise to two peaks of potential vorticity (fig. 8.1). There is a minimum at $y = 260$km because the velocity gradient is positive and a maximum at $y = 740$km because the velocity gradient is negative. The velocity field and the mean potential vorticity are not symmetric because of the different atmospheric layer thicknesses: $\langle h^a(y = 260\text{km})\rangle_{t,x} = 586m$ whereas $\langle h^a(y = 740\text{km})\rangle_{t,x} = 408m$, where $\langle\rangle_{t,x}$ denotes averaging over time from day 1500 to day 2000 and over space along the x-axis.

The ocean layer submitted to the forcing of the atmosphere and the damping develops three extrema in the PV, which appear around the locations where the velocity in the atmosphere vanishes. This behavior is explained by the one-dimensional model in chapter 6.

The distance of the extrema is this of the inflexion points in the wind. Shallow water currents are found by Paldor and Ghil [1997] to be most unstable when the characteristic length scale is close to the Rossby radius of deformation.

In one dimension, in the atmosphere the temporal potential vorticity along the y-axis is almost indistinguishable for one-way and two-way interactions. Indeed only the shear applied to the atmosphere changes and as oceanic velocity is very low compared to the atmospheric velocity the shear applied to the atmosphere hardly varies. In the ocean the small differences between two way and one way are due to the feedback of the forcing on the ocean. The qualitative behavior is the same as of the, well understood, simple one dimensional model discussed in chapter 6. The situation is different for the fully two dimensional configuration, which allows for instability, as we will show in the sequel.

8.2 Two Dimensional Shallow Water Model

In this part, we present results from integrations of the fully 2D numerical model described in the section 7.3.

We added an initial perturbation to the ocean. A narrow jet in geostrophic equilibrium, perpendicular to the atmospheric current, depending only on the x-direction, is imposed. It is calculated from the height variation:

$$\begin{aligned}\eta_o^o(x,y) &= 100m \times (sin(2\pi x/L_x) - \frac{1}{3}sin(4\pi x/L_x) + \frac{1}{5}sin(6\pi x/L_x) \\ &- \frac{1}{7}sin(8\pi x/L_x) + \frac{1}{9}sin(10\pi x/L_x)).\end{aligned}$$

This initial perturbation disappears overtime and after 900days no trace of it is visible in the ocean.

8.3 One way Interaction

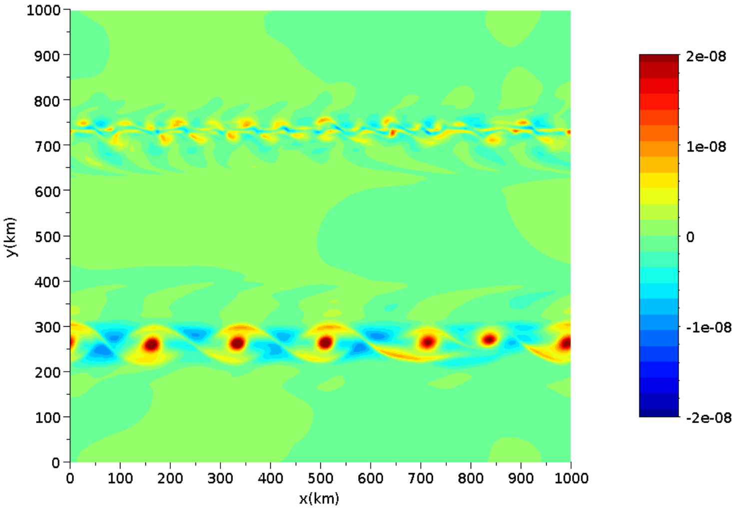

Figure 8.2: Potential vorticity anomaly (in $s^{-1}.m^{-1}$), in 2D, for one-way interaction, in the ocean at $t = 2000$days.

In one way simulation, there are no dependencies on the x-direction in the atmosphere, as we do not considered the action of the ocean for the shear applied to it and as there is no instability developing in the atmosphere. The dynamics in the atmosphere is identical to the 1D-2C simulation as can be verified in fig. 8.1. The atmospheric dynamics converges towards a balance between the large scale forcing, viscous dissipation and the drag at the lower (motionless) boundary. The development of an atmospheric instability is inhibited by the forcing, which acts at the basin scale, which is close to 2π-times the atmospheric Rossby radius of deformation. In the ocean, instabilities develop as shown by the potential vorticity anomalies in fig. 8.2, in the form of two vortex streets along lines, where the average velocity differences between the ocean and the atmosphere vanish.

The anomalies are about twice as strong at 260km than at 740km. Indeed, the greater the distance between the potential vorticity maxima, the stronger and bigger are the instabilities, that is why eddies are more developed at 260km. These instabilities lead to a turbulent dissipation of energy in these latitudes, and decrease the amplitude of oceanic potential vorticity peaks.

The size of the ocean eddies created by instability can be estimated from fig. 8.2. For a quantitative determination of the scale of the turbulent structures we determine the Taylor scale:

$$\lambda(y) = \sqrt{\frac{\langle \zeta^2 \rangle_{t,x}}{2\langle u^2 + v^2 \rangle_{t,x}}}, \tag{8.1}$$

where averages are taken in time (from day 1500 to day 2000 of the integration) and along the x-axis. Results for the ocean (not shown) give a size at the locations of instability which vary around the Rossby radius of deformation ($Rd^o = \sqrt{g^o H^o}/f = 20$km). At $y = 740$km we have $\langle h^o \rangle_{t,x} = 176$m leading to $Rd^o = \sqrt{g^o h^o}/f = 18.8$km and at $y = 260$km, $\langle h^o \rangle_{t,x} = 215$m leads to $Rd^o = \sqrt{g^o h^o}/f = 20.7$km. Although the Taylor scale varies, the values are close to the oceanic Rossby radius of deformation and taking into account the difference of the layer thickness the trend is well respected and scales are smaller at 740km than at 260km as can also be seen in fig. 8.2.

In the atmosphere, which has no variability, neither in x nor in time, the Taylor scale reaches zero at the location where the velocity vanishes and vorticity is large. This proves that the ocean adapts to the dynamics of the atmosphere at large scale, but develops its own dynamic with typical scale of the order of the oceanic Rossby radius of deformation. This agrees well with the results of Paldor and Ghil [1997], who found the most unstable mode of a shallow water current having a cosh-velocity-profile to be connected to the Rossby radius of deformation. The size of the eddies is then around $2\pi\lambda$ and we see that there are numerous eddies at $y = 740$km and six eddies are present at $y = 260$km along the periodic x-direction.

8.4 Two-way Interaction

For two way interactions, the time averaged potential vorticity is very different between the 1D and the 2D simulation. It is due to the non linear terms in x, which are neglected in 1D.

The main characteristic of the two way simulation in 2D, is the formation of two atmospheric perturbations (fig. 8.3), one between 680km and 800km and another between 150 and 350km. These eddies are formed just above the line of oceanic eddies and move along the x-direction with the mean flow. They lead to a significant turbulent dissipation of energy, that expands and strongly reduces the two potential vorticity extrema. Around 260km the anomaly is ten-times lower than the one around 740km, because of the thicker atmospheric layer in this latitude which stabilizes the fluid.

The time averaged atmospheric potential vorticity peaks are larger than in one way simulation, so the action induces in the ocean three potential vorticity extrema that are further apart. As they are more distant, ocean instabilities are bigger and stronger, as we can see in the figs. 8.2 and 8.3.

To better analyze the size of instabilities in the two layers, we again considered the Taylor scale. It is of the order of 30km in the ocean, larger than in the one way case due to the retro-action of the atmosphere. This can be explained by the observation that the atmospheric scale, which represents the forcing is also increased. It still compares well to the oceanic Rossby radius of deformation in the ocean which is around 20km. Near $y = 740$km $\langle h^o \rangle_{t,x} = 183$m leading to $Rd^o = 19.1$km and near $y = 260$km $\langle h^o \rangle_{t,x} = 221$m leading to $Rd^o = 21$km. As we have seen previously, turbulent scales are larger around 740km than around 260km because of the thicker layer at 260km. The trend is respected

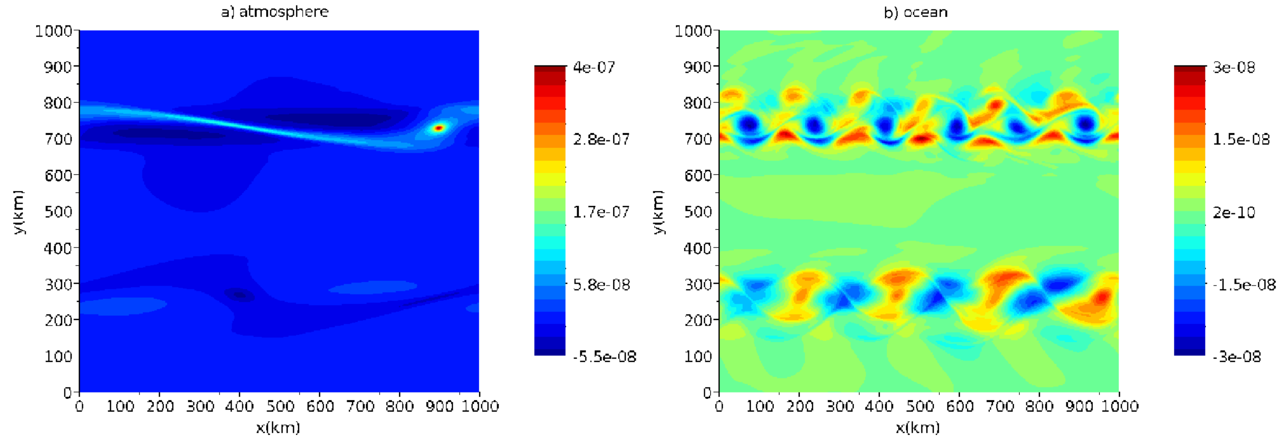

Figure 8.3: Potential vorticity anomalies (in $s^{-1}.m^{-1}$), in 2D, for a two-way interaction, in the atmosphere (left) and in the ocean (right) at $t = 2000$days.

and scales are greater than in one way simulations.

For two way simulations, a turbulent scale in the y-direction of the order of 10km appears in the atmosphere. The smallest scale of the atmosphere corresponds well to the smallest scale in the ocean. This scale does not correspond to the characteristic scale $Rd^a = 200km$ that develops usually in the atmosphere. The atmospheric turbulent scale is of the order of the oceanic Rossby radius of deformation and are the imprint of the ocean dynamics. It shows that the unstable dynamics in the atmosphere is slaved to the ocean dynamics. However, the forcing of the atmosphere is at large scales, at the scale of the atmospheric Rossby radius of deformation and has therefore a strong damping effect on the dynamics on the atmospheric synoptic scale and hinders the development of instability at the synoptic scale. Increasing the domain to allow for an unforced development in the atmosphere at its synoptic scale, also, is beyond our actual computer resources.

The forcing at large scale explains that in the x-direction, turbulent scales are of the order of the atmospheric Rossby radius of deformation. But note, that in the x-direction there is only one structure in the domain, showing that the larger synoptic scale in the atmosphere leaves its imprint in the dynamics of the instability, which can not extend in the y-direction due to the forcing.

We have so far only considered the statistically stationary turbulent state of the instability, but not its initial evolution. There are two processes involved, first the spin-up of the ocean by currents due to the wind-shear at the surface, which has a typical spin-up time scale of $t_{\text{spinup}} = (h^o \rho^o)/(c_D \rho^a u) \approx 300$days and second, the characteristic time scale of the barotropic instability, which is around a few tens of days. The latter is much shorter than the former and indeed small amplitude barotropic instability is observed early in the experiment, but only attains its full amplitude and a stationary state at time scales characteristic of the ocean spin up. The spin up time is inversely proportional to the thickness of the oceanic surface layer, which also means that in surface mixed layers much shallower than the 200m used here it proceeds much faster. The numerical calculations with a shallower ocean layers is however more involved due to the finer resolution necessary and the increased stiffness of the system.

Chapter 9

Discussion

We have demonstrated, that the complicity of turbulent friction between the air and the ocean and the horizontal turbulent friction in the atmosphere triggers a barotropic instability in the ocean which propagates to the atmosphere. The simple model used is composed of two superposed shallow-water layers, the turbulent friction is parametrized by the classical drag law and the horizontal turbulent exchange of vorticity by a constant eddy viscosity. The physics of the instability is depicted and its explanation is based on physical arguments which apply also to more involved models and to the nature of the air, the sea and their interaction.

Paldor and Ghil [1997] demonstrated the importance of the Rossby radius of deformation for the barotropic instability of currents. They found that their jet was stable if narrower than πR, where R is the Rossby radius of deformation. Wider jets are stable for perturbations smaller than πR with a maximum growth-rate for scales around $2\pi R$. In view of their work, neither the stability of the atmospheric layer, in one-way interaction, nor the instability of the ocean layer in our calculations are a surprise, although our system of forced and dissipative dynamics is far from the free jets studied by Paldor and Ghil [1997]. More surprising is that the unstable ocean dynamics manages to trigger a sustained submesoscale instability in the atmosphere. The present work is an example how the interaction of the atmosphere and ocean can give rise to new interesting dynamics.

A prerequisite to observe the here discussed instability in numerical models of the ocean and atmosphere dynamics is the fine resolution. The atmospheric model has to resolve the scales corresponding to the oceanic Rossby radius of deformation. As in coupled simulations atmospheric models are usually run at coarser grid scale than the oceanic model, this is today not the case in most simulations performed.

The present results are obtained using a model based on two shallow-water layers with constant viscosities in the atmosphere and the ocean, that differ by two orders of magnitude. The difference in the viscosity will also appear in fine resolution models using large eddy simulations (LES) as the coefficients are calculated based on characteristic scales in space and velocity which are both higher in the atmosphere than in the ocean. Furthermore, LES schemes that are based on velocity gradients will amplify the dissipation near points of vanishing wind-stress, where horizontal gradients are amplified by the quadratic drag law.

Research of how the here discovered instability mechanism acts in more complicated models for ocean and atmosphere dynamics and the research of small scale structures in the ocean near lines and points of vanishing wind-stress are the next step. We want to emphasize once more that the discussed instability is not numerical but due to the physics of air-sea interaction. Fine resolution observations provided by satellite data of the sea surface, together with observations of the ocean wind stress will be used to track down this instability in the ocean.

Part III

Momentum transfer between an atmospheric and an oceanic layer at the synoptic and the mesoscale

Chapter 10

Introduction

Today's theory of the basin-scale ocean-dynamics is based on the conservation and fluxes of (potential) vorticity (see e.g. Vallis [2006]). The large scale features of the ocean dynamics can be explained to leading order by a wind-stress forcing that is averaged in space and time. In numerical simulations of the ocean dynamics, performed during the past four decades, the wind-stress field was commonly averaged over one month in time and a few degrees in both longitude and latitude. There has more recently been a growing interest in the ocean circulation kinetic energy: reservoirs, sources and sinks (Ferrari and Wunsch [2009]). The major input of mechanical energy into the ocean is through the wind-stress, that is the friction caused by the different horizontal velocities of the atmospheric winds and the ocean currents near the ocean surface. A theory of how kinetic energy is injected by the large-scale wind-stress into the basin-scale geostrophic ocean-circulation is given in Roquet et al. [2011]. At smaller scales the energy injection is, so far, less studied and understood. Furthermore, the ocean currents were commonly not taken into account when the wind-stress field was calculated, because the ocean surface currents velocities are small as compared to atmospheric winds over much of the ocean. Calculating the wind-stress using the difference between the ocean currents and the atmospheric wind, rather than the wind only, was found to lead to a twenty percent reduction of energy input in the large scale double-gyre circulation (Duhaut and Straub [2006]).

As the resolution of (satellite) observations becomes ever finer in space and shorter in time, air-sea interactions at smaller scales are found to leave their imprint in the atmosphere and ocean dynamics (Chelton et al. [2004]) leading to persistent small-scale structures in the atmospheric winds. The air-sea heat flux influencing the marine atmospheric boundary layer is found in Chelton et al. [2004] to be the dominant source of the small-scale structures in the atmospheric winds. In the present work the influence of momentum transfer due to ocean dynamics is considered.

The importance of these small scale interactions for the atmosphere and ocean dynamics is confirmed using numerical simulations in idealized configurations (Hogg et al. [2009]) and when applied to regional configurations (Seo et al. [2008]). As the resolution of regional and global ocean models becomes ever finer in space and shorter in time, they become increasingly sensitive to more accurate and finer-resolution higher-frequency surface-wind-stress forcing. The importance of realistic amplitude, fine resolution and high-wavenumber, surface-wind-forcing has been demonstrated in a variety of ocean modeling and climate applications. Recent fine scale satellite observations of the sea surface show an abundance of dynamical features at the oceanic meso and sub-meso scale. The explanation of the origin, turbulent dynamics and fate of these structures represents a formidable problem of geophysical fluid dynamics.

In the present work we exclusively focus on the exchange of momentum to evaluate its potential as an alternative source of small scales structures in the ocean and the atmosphere. The most conspicuous feature of the atmosphere-ocean system is the different density of the two phases, leading to a large difference in the inertia of the atmosphere and the ocean layer. At large times the atmosphere is influenced by the persistent ocean dynamics, while the short time fluctuations appear to be independent of the ocean. On the other side, short time fluctuations have only a negligible influence on the ocean dynamics, which however responds to a persistent atmospheric forcing. This is discussed in detail by Esau [2014] for the case of the heat exchange, the case of the momentum exchange is considered here. As noted in Esau [2014] the difference in density leads in numerical models to imposing different types of boundary conditions to the atmosphere, the value is imposed (Dirichlet boundary conditions) and the ocean, the flux is imposed (Von Neumann boundary conditions). This is not only the case for the heat-flux (as discussed in Esau [2014]) but the same is true for the flux of inertia.

Estimates of energy fluxes are usually based on coarse-grained variables, that is variables averaged in time and space. Variables from (satellite) observations and numerical models are always coarse-grained representations of the real dynamics. When energy fluxes are estimated based on coarse-grained variables it is often not clear how good the estimate is, or even if the true value is over- or under-estimated. The energy input and cycle is however key to understanding the dynamics of the atmosphere, ocean and climate system. The fluxes at smaller scales contribute to the turbulent mixing of substances and momentum, in the atmosphere and the ocean, without which we can not fully understand the respective dynamics. Furthermore, in the two-dimensional turbulent dynamics of the atmosphere and the ocean, energy cascades from smaller to larger scales (see e.g. Vallis [2006]), emphasizing the importance of energy exchanges at small scales for the large scale dynamics.

In this study, two superposed one-layer fine-resolution shallow-water models are used. The upper layer represents the atmosphere and the lower layer the ocean. Their only interaction is through a frictional force at the interface, which is parameterized by the prominent quadratic drag law. The characteristic horizontal length scales in the atmosphere and the ocean are the respective first baroclinic Rossby radii of deformation. The layer thicknesses of the atmosphere and the ocean in our model are chosen, so that the (barotropic) Rossby radii of deformation correspond to the respective length scales. The first baroclinic atmospheric Rossby radius of deformation (a few hundreds of kilometers) is usually referred to as the synoptic scale and in oceanography the first baroclinic oceanic Rossby radius of deformation (a few tens of kilometers) is referred to as the mesoscale (e.g. section 1.1.1). All structures with a horizontal extension smaller than the synoptic scale will be called small scale, for convenience. Synoptic structures in the atmosphere rarely take more than a few days until they have moved away from a specific location, while the corresponding time scale for mesoscale eddies in the ocean is of a few weeks.

Experiments with different values of the surface-friction drag-coefficient are performed. It is varied within the range of observed values of the ocean-atmosphere system. Ocean currents are not neglected when calculating the shear between the ocean and the atmosphere. A physically consistent parametrization of the shear between ocean and atmosphere is employed, without interpolation, neither in space nor in time, beyond the grid resolution and the numerical time-step. This leads to a dynamically consistent model respecting Newton's laws of motion. The approach and a version of the model discussed here has already been used to illustrate a new mechanism of inducing barotropic instability in the ocean by air-sea interaction (Moulin et al. [2014]).

A fully coupled 3D-atmosphere and ocean model was used by Esau [2014] to consider heat fluxes and the induced turbulent convective dynamics in the mixed layers at the meso and sub-meso scales. He, however, considered a stress-free interface, that is without transfer of momentum. We consider momentum transfer, without including buoyancy or buoyancy fluxes. The two studies are complementary and the combination of the two effects is left for future research.

In the present work we focus on the local exchange of momentum between the ocean and the atmosphere at the synoptic, and the mesoscale. The forcing has no large scale component. The situation is very different from basin scale forcing, dynamics and flow. A basin wide forcing and circulation can create strong boundary currents which can separate from the boundary and penetrate into the interior of the domain, as is the case for the double gyre circulation (Duhaut and Straub [2006], Hogg et al. [2009]), leading to strong ocean currents. To the best of our knowledge the local exchange of momentum, only, between a turbulent atmosphere and ocean, at the mesoscale has never been considered before.

In the present work, the qualitative dynamics of air sea-interaction is considered and the existence of two different regimes is exposed. We further assemble quantitative results on the energy fluxes and vorticity correlations between the atmosphere and the ocean for different values of the atmospheric friction coefficient. They allow to evaluate the importance of the dynamics at the meso and sub-mesoscale for the dynamics of the atmosphere and the ocean. There exists, to the best of our knowledge, no work discussing the interaction of a turbulent atmosphere-ocean system at the synoptic scale and below and providing quantitative evidence.

Exchanges of heat and chemical substances are of paramount importance for the dynamics of the atmosphere, the ocean and the climate of our planet but they are not considered here as we exclusively focus on the exchange of momentum. As models of the atmosphere, the ocean and the climate system become ever more refined, further processes have to be explored and their possible impact on the dynamics has to be evaluated. It is therefore important to investigate and quantify the exchange of momentum between the synoptic and the mesoscale, the scales where the atmospheric and oceanic speeds are high.

The two superposed shallow water models and their coupling are introduced in the next section. Experiments are performed for different values of the drag coefficient given in chapter 12, where the results concerning the energy transfer and the correlation between the vorticity dynamics in the ocean and the atmosphere are presented. The results are discussed in chapter 13 and conclusion presented in chapter 14.

Chapter 11

Shallow Water Model

11.1 Physical model

The model consists of two superposed homogeneous fluid layers, a shallow layer for the lower atmosphere above an ocean surface layer. The average thicknesses are respectively $H^a = 1000m$ and $H^o = 200m$. The actual layer thicknesses $h^a(x, y, t)$, $h^o(x, y, t)$ vary over time and space. The ocean surface layer superposes a motionless layer of higher density and of infinite depth. Similarly a motionless layer of air of a lesser density superposes the shallow atmosphere layer. Layers have an average density of $\rho^a = 1kg/m^3$ and $\rho^o = 1000kg/m^3$. The fluid motion considered extends over a period many days and so, the model must take into account the Earth's rotation. Using the f-plane approximation we set the Coriolis parameter $f = 10^{-4}\text{s}^{-1}$, a typical value at mid-latitudes.

11.2 Mathematical model

This physical model can be described by the reduced gravity shallow water equations:

$$\begin{aligned} \partial_t u^k + u^k \partial_x u^k + v^k \partial_y u^k - f v^k + g^k \partial_x h^k &= \nu^k \nabla^2 u^k + F_x^k && (11.1) \\ \partial_t v^k + u^k \partial_x v^k + v^k \partial_y v^k + f u^k + g^k \partial_y h^k &= \nu^k \nabla^2 v^k + F_y^k && (11.2) \\ \partial_t h^k + \partial_x [h^k u^k] + \partial_y [h^k v^k] = \tilde{F}_h^k, & && (11.3) \end{aligned}$$

Where $k = a, o$ stands for the atmosphere and the ocean, respectively. The parameters g^a and g^o are the reduced gravity of the atmosphere and of the ocean (i.e., the gravitational acceleration multiplied by the fractional density difference between the two layers). They are respectively set to $0.8m/s^2$ and $2.10^{-2}\ m/s^2$. The restoring force $\tilde{F}_h^k$ in the atmosphere and ocean acts on the layer-thickness.

The typical horizontal scale is the Rossby radius of deformation $Rd^k = \sqrt{g^k H^k}/f$. It is about one order of magnitude smaller in the ocean where $Rd^o = 20km$ than in the atmosphere where $Rd^a \simeq 283km$. The domain size is $L_x = L_y = 4000\text{km}$ and there are periodic boundary conditions in both horizontal directions. In the absence of forcing and friction the potential vorticity (PV):

$$q^k = \frac{\zeta^k + f}{h^k} \quad \text{with} \quad \zeta^k = \partial_x v^k - \partial_y u^k, \tag{11.4}$$

is conserved by the flow.

The initial oceanic height variation is defined by the sum of the 2π periodic cosinus in the x- and y- direction.

$$\eta_o^a(x,y) = 50m \times (cos(\frac{2\pi(x - 7/24)}{L_x}) + cos(\frac{2\pi(y - 7/24)}{L_y}))$$

The initial velocity field is calculated using the geostrophic equilibrium.

The initial atmospheric height variation (B.1) is defined by a periodic alternating of cyclone and anticyclone in the x and y direction with a period of 1000km.

$$\begin{aligned} \eta_o^a(x,y) = 350m\times \quad [& \quad cos(8\pi x/L_x) + cos(16\pi x/L_x) + cos(24\pi x/L_x) \\ + & \quad cos(8\pi y/L_y)) + cos(16\pi y/L_y) + cos(24\pi y/L_y) \\ + & \quad cos(8\pi(x+y)/L_x) + cos(16\pi(x+y)/L_x)] \end{aligned} \tag{11.5}$$

The initial velocity field is calculated using the geostrophic equilibrium, so four cyclonic and anti-cyclonic alternating structures are imposed on the x and on the y direction, leading to 16 identical tiles in the forcing field.

A restoring acts to force the average of the atmospheric layer thickness projected on the forcing profile (eq. (11.5)) towards its initial value. To this end, the projection is compared to its initial value and a multiple of the initial profile is added or subtracted to restore towards the initial amplitude of the projected mode. Such kind of restoring directly affects only the forced mode without directly influencing the other modes which can evolve more freely. The restoring time is two days. The variations of layer thickness in the ocean layer are locally and linearly damped to zero with a long damping time of 1000 days, in order to not disturb the air-sea interaction.

When parameterizing the effect of small-scale turbulent friction at a solid boundary a quadratic drag law is used. Such a drag law dates back to the work of Prandtl and Schlichting [1934] & Schlichting and Gertsen [2000] and has been extensively studied since then (see Schlichting and Gertsen [2000]). All these investigations essentially confirming its robustness and its applicability to all fields of fluid dynamics. When the motion of the atmosphere and the ocean are considered a large volume of research is dedicated to the determination of the drag coefficient over various surfaces (Stull [1988]). When the sea surface is considered the drag coefficient depends on the sea-state, which itself is a function of various parameters (see *e.g.* Högström et al. [2013]). The robustness of the law itself seems above any doubt.

The two layers are only linked by frictional forces at the interface, parameterized by a quadratic drag law. The frictional acceleration between the two layers (see eqs. (11.1) and (11.2)) is defined by:

$$\begin{pmatrix} F_x^k \\ F_y^k \end{pmatrix} = \pm \frac{1}{\rho^k h^k} \begin{pmatrix} f_x^k \\ f_y^k \end{pmatrix}. \tag{11.6}$$

Where f_x and f_y are the surface forces varying in x, y and time. They are calculated using the velocity difference between wind and ocean current.

$$\begin{pmatrix} f_x^o \\ f_y^o \end{pmatrix} = \rho^a C_d |u| \begin{pmatrix} u^o - u^a \\ v^o - v^a \end{pmatrix}, \tag{11.7}$$

with $|u| = \sqrt{(u^o - u^a)^2 + (v^o - v^a)^2}$. The shear applied to the atmosphere is the opposite to the shear applied to the ocean.

The drag coefficient C_d is constant within each experiment.

11.3 Numerical model

The ocean and the atmosphere basins are represented by a rectangle, of $L_x \times L_y$. Periodic boundary conditions are used in both horizontal directions. The numerical grid is regular and contains $n_x \times n_y$ points. Fine spatial resolutions $\Delta x = L_x/n_x = \Delta y = L_y/n_y$ are employed to well resolved the horizontal scales. We choose $n_x = n_y = 2048$ and $L_x = L_y = 4000km$ for the 2D shallow water model. The horizontal components of the velocity u^k, v^k, and height variations η^k are calculated on each grid point. The eddy viscosity of the layers are $\nu^a = 500m^2/s$ and $\nu^o = 0.1m^2/s$, which are constants in space and time.

A second order centered finite difference method is used for the space discretization and a second-order Runge-Kutta scheme is used for the time discretization. The time step is constraint by the Courant-Friedrichs-Lewy (CFL) condition (see Courant et al. [1928]). It states that the time step must be less than the time for the wave to travel to adjacent grid points. As atmospheric waves are ten times faster than oceanic waves, it is the CFL condition for the atmosphere that sets the minimum time step $\Delta t = 15$s to well resolve the temporal evolution of the atmospheric dynamics.

The model has been already employed in Moulin et al. [2014] at lower resolution in a non-parallelized version.

11.4 Experiments Performed

We present results from four numerical experiments which only vary by the drag coefficient used. The drag coefficient C_d is constant for each experiment. In the four simulations discussed here, the drag coefficient is $C_d = 1 \times 10^{-4}$, 2×10^{-4}, 4×10^{-4} and 8×10^{-4}. The values used are within the typical values for ocean dynamics.

The drag coefficient depends on a variety of parameters as the ocean state and the density stratification of the atmosphere. When the motion of the atmosphere and the ocean are considered a large volume of research is dedicated to the determination of the drag coefficient over various surfaces (e.g. Stull [1988], Högström et al. [2013]) and atmospheric conditions. In the shallow water equations the velocity vertically averaged over the whole layer thickness, is represented. This explains, why these geostrophic drag coefficients are lower than the drag coefficients based on velocities at 10m above the ocean surface (*e.g.* Stull [1988]). According to Stull [1988] the drag coefficient for a reference level of about 500m is between 1×10^{-4} for stable atmosphere and 8×10^{-4} for a neutral atmosphere.

Integrations are performed over 2700 days. The last 1000 days are considered for temporal averages. This ensures that the calculations have converged close to a statistically stationary state.

Chapter 12

Results

12.1 Qualitative Description

In all the four experiments a nonlinear dynamics is observed in the atmosphere and the ocean. The speeds and the absolute vorticity values of the ocean increase as the drag coefficient increases. The opposite is true for the atmosphere, as expected. The structures in the ocean are smaller than those in the atmosphere, showing that both developed their own dynamics. The difference in size is readily explained by the different Rossby radii of deformation. For all values of the drag coefficient, a correspondence between the vorticity in the atmosphere and the ocean is observed, showing that the dynamics in the atmosphere and the ocean is co-organized.

For the smaller values of the drag coefficient the co-organization is only visible in the averages (see fig. 12.1, lower panels), as the atmospheric perturbations are strong and evolve on a much faster time-scale than the ocean. The short-term instantaneous perturbations in the atmosphere are almost transparent to the ocean, which only adapts to a time-integrated atmospheric dynamics. The atmospheric dynamics appears independent of the ocean dynamics and the external forcing on the atmosphere, when instantaneous values are considered (see fig. 12.1 upper panels). In the instantaneous vorticity field of the experiment with the lowest drag coefficient, the 16 cells of the space periodic forcing are visible in the ocean but not in the atmosphere, although the forcing is applied to the atmosphere and not to the ocean, which experiences it only through the atmospheric dynamics. When long-time averages are considered the forcing is also the dominant signal in the atmosphere. This shows that the ocean adapts to a time-averaged atmosphere. For the smaller drag coefficients there are only a few coherent structures in the ocean. The velocities are too small for the non-linear terms to become important, and their dynamics is hindered by the strong atmospheric turbulence representing a high frequency forcing on the ocean dynamics. Inspection of movies show that at times, the atmospheric eddies are attracted by like-sign ocean vorticity structures and they superpose during few days. This injects further vorticity in the ocean and leads to stronger eddies during a laps of time. These transient structures in the ocean disappear after the atmospheric eddy has moved and the high-frequency forcing of to the atmosphere disintegrates the structures.

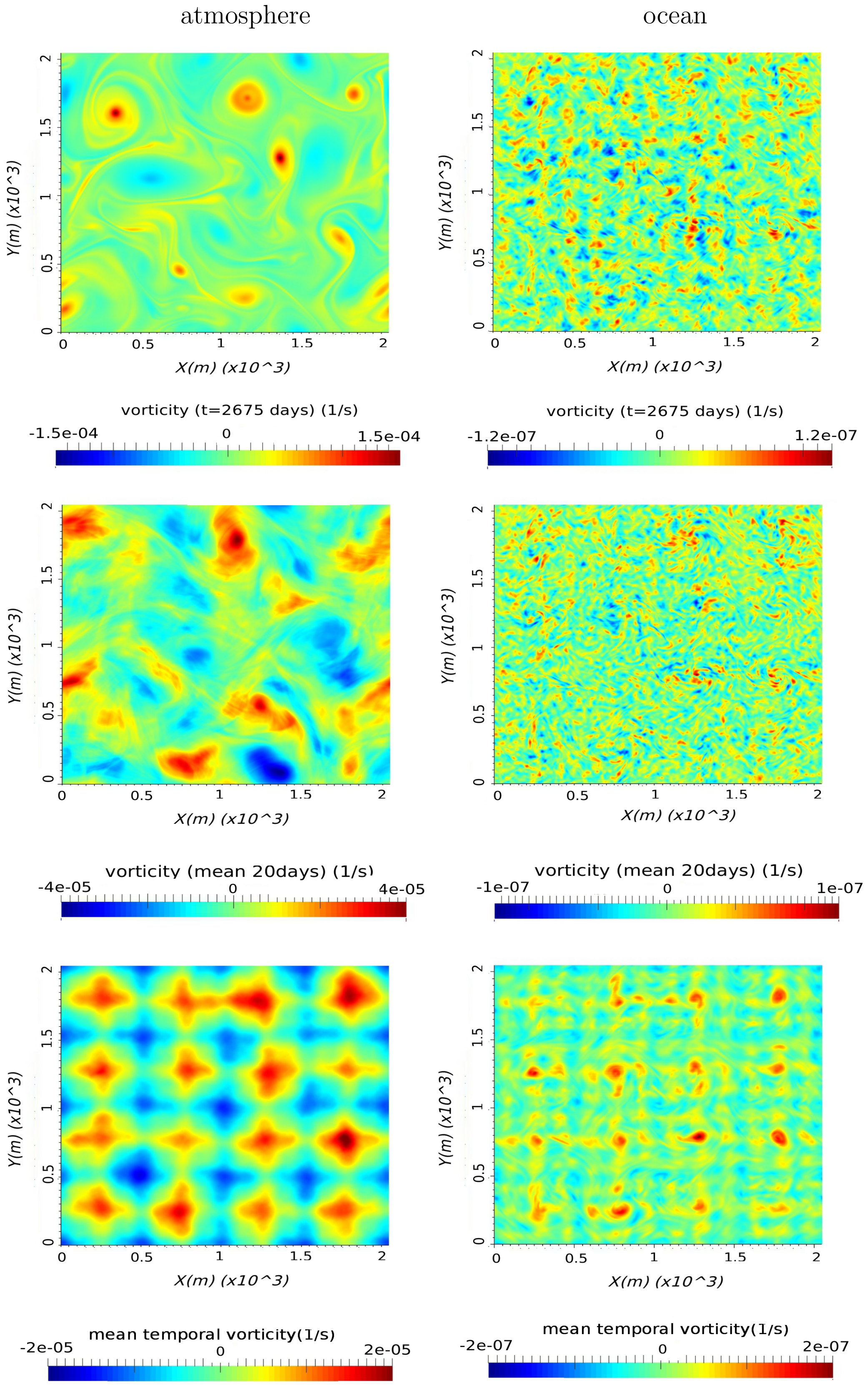

Figure 12.1: For $C_d = 1 \times 10^{-4}$. Map of the average vorticity, averaged over 1000 days, starting from day 1700 (bottom). Map of the vorticity anomaly, averaged over 20 days, starting from day 2680, with respect to the 1000day average (middle). Map of the instantaneous vorticity anomaly at day 2675, with respect to the 1000 days average (top).

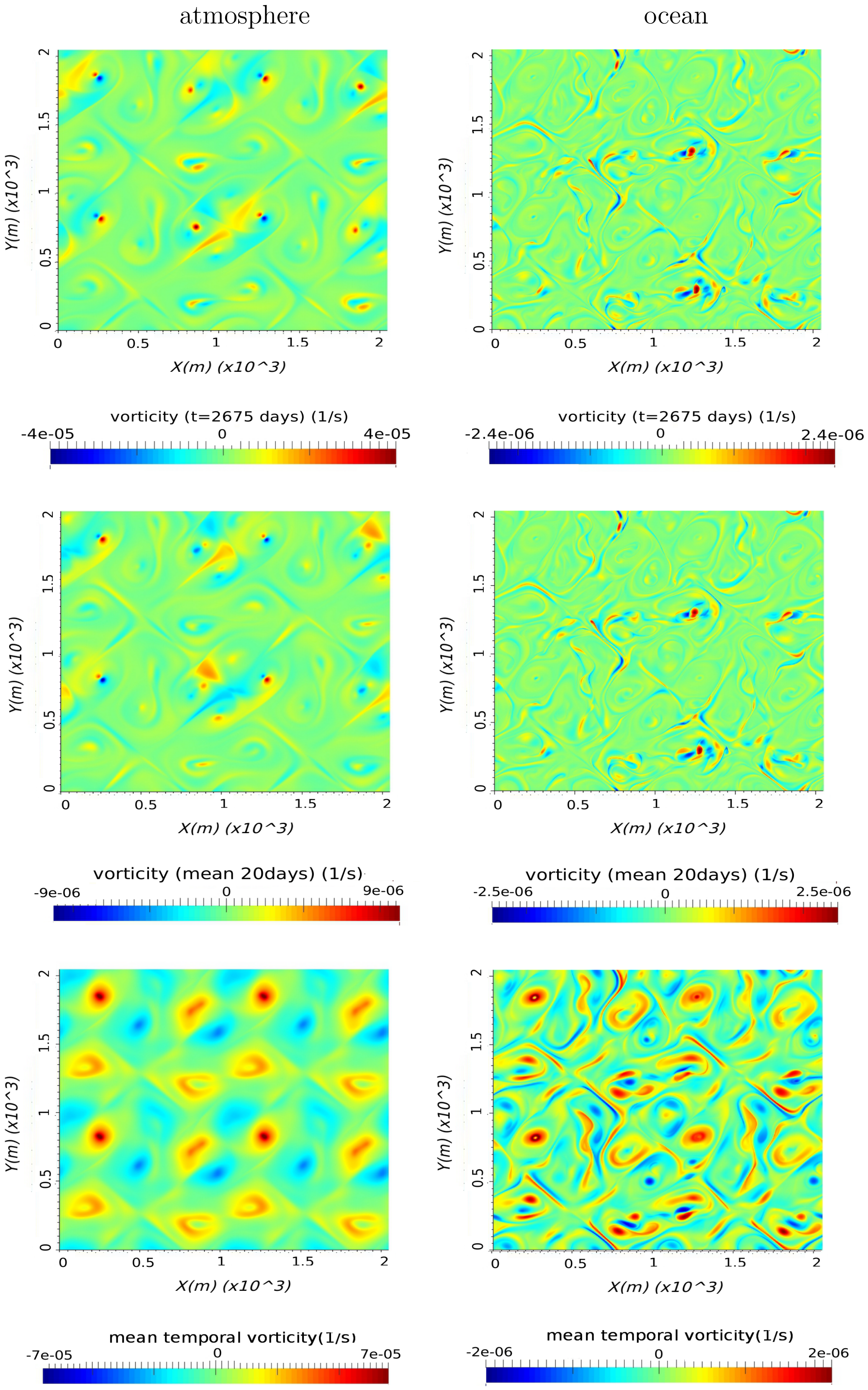

Figure 12.2: For $C_d = 8 \times 10^{-4}$. Map of the average vorticity, averaged over 1000 days, starting from day 1700(bottom). Map of the vorticity anomaly, averaged over 20 days, starting from day 2680, with respect to the 1000day average (middle). Map of the instantaneous vorticity anomaly at day 2675, with respect to the 1000 days average (top).

For the largest value of the drag coefficient the situation is qualitatively different. A variety of coherent structures dominate the vorticity filed in the ocean and the atmosphere and they appear co-located (see fig. 12.1). The temporal vorticity anomaly in the atmosphere is strongly damped (see fig. 12.1 upper-left panel) and the atmosphere and ocean dynamics is in a quenched disordered state. That is, a spatial disorder with a very slow evolution in time, in both the atmosphere and the ocean is observed. Such type of dynamics is found and extensively studied in spin-glasses but has so far not been mentioned in the context of air-sea interaction, to the best of our knowledge. The atmosphere is in a quasi-stationary state. This allows the ocean to develop larger eddies (fig 12.2). After a few years, the ocean and the atmosphere have a similar dynamics at large scale with many co-located features. As we see in figure 12.2, the mean vorticity, averaged over 1000 days, is strong as compared to the temporal vorticity anomalies, in both the atmosphere and the ocean. In the atmosphere the vorticity anomaly shows the formation of dipole structures, where there is a strong mean vorticity. They are the signature of the displacement of vortices. Many of the atmospheric eddies have a ring-structure, due to opposite vorticity in the ocean at the center of the atmospheric eddy. When no opposite vorticity is present in the ocean, the atmospheric eddies have stronger vorticity.

12.2 Kinetic energy transfer

The density differences between the air and the water masses leads to a large discrepancy between the speeds in the ocean and the atmosphere as shown in tab. 12.1. When increasing the drag coefficient eight fold, the atmospheric r.m.s velocity decreases by about 40%, while the oceanic r.m.s velocity increases almost an order of magnitude. This is also visible in the ratio between the kinetic energy in the ocean and the atmosphere, which is over 200 times higher with the highest drag coefficient as compared to the lowest (tab. 12.1).

The mechanical power input per unit surface area to the ocean is the vector-product of the wind-stress shear τ and the ocean velocity $\mathbf{u^o}$, that is: $P = \tau \cdot \mathbf{u^o}$ (*e.g.* Duhaut and Straub [2006]). The power input using the correct representation of the shear force, is based on the velocity difference between the atmospheric and the oceanic velocity $\tau_\mathbf{c} = \rho^a C_d |\mathbf{u^a} - \mathbf{u^o}|(\mathbf{u^a} - \mathbf{u^o})$. The approximation where the effect of the ocean current is neglected when calculating the shear $\tau_\mathbf{app} = \rho^a C_d |\mathbf{u^a}|\mathbf{u^a}$ is often used. It is justified by the fact, that the ocean currents are feeble as compared to the wind speeds ($u^o \ll u^a$). Duhaut and Straub (Duhaut and Straub [2006]) revealed an overestimation of about 20 percent of the power input to the ocean, in a double gyre configuration with a prescribed time-independent wind velocity, when the approximation is used. It can be shown that the correct values of the power input P_c are always smaller than the approximative values P_{app}. In our results, there is almost no difference between P_c and P_{app} for the smaller drag coefficients, because the ocean speeds are very small as compared to the atmospheric speed. For the highest drag coefficient the energy input estimated with the approximation overestimates the power input by 5%. The difference is accentuated for larger drag coefficients as higher velocities are induced in the ocean, and the ocean velocities are more aligned with the atmospheric velocities (fig. 12.2). The fact that on average the difference is low, does not mean, that locally it is not important, in areas where oceanic currents are strong and aligned to the atmospheric winds.

Table 12.1: Averaged quantities for the four values of the drag coefficient. Mean power lost/gained by the atmosphere/ocean for the consistent calculation ($\overline{Pa(u^a)}^t$, $\overline{Po(u^a, u^o)}^t$) and power lost/gained based on the mean atmospheric/oceanic velocity ($Pa(\overline{u^a}^t)$, $Po(\overline{u^a}^t, \overline{u^o}^t)$).

C_d	1×10^{-4}	2×10^{-4}	4×10^{-4}	8×10^{-4}
$\sqrt{u^{a2}}(m/s)$	3.3	2.9	2.5	2.0
$\sqrt{u^{o2}}(m/s)$	3.4×10^{-3}	6.4×10^{-3}	1.3×10^{-2}	3.1×10^{-2}
E_a/E_o	4.6×10^{3}	1.1×10^{3}	2.2×10^{2}	22
surface fraction where the atmosph. losses energy(%)	99	98	97	95.5
surface fraction where the ocean gains energy(%)	58	70	82	77
$Pa(\overline{u^a}^t)$ $(W.m^{-2})$	-3.6×10^{-3}	-4.9×10^{-3}	-6.3×10^{-3}	-6.4×10^{-3}
$\overline{Pa(u^a)}^t$ $(W.m^{-2})$	-4.6×10^{-3}	-6.1×10^{-3}	-7.5×10^{-3}	-7.0×10^{-3}
$Po(\overline{u^a}^t, \overline{u^o}^t)$ $(W.m^{-2})$	2.6×10^{-6}	7.9×10^{-6}	2.4×10^{-5}	7.0×10^{-5}
$\overline{Po(u^a, u^o)}^t$ $(W.m^{-2})$	8.7×10^{-7}	5.2×10^{-6}	2.1×10^{-5}	8.3×10^{-5}
Taylor scale in the atmosphere (km)	127	121	112	116
Taylor scale in the ocean (km)	68	74	83	45

On average, the atmosphere loses energy over more than 95 percent of its surface area for all drag coefficient (table 12.1). The percentage increases with a decreasing drag coefficients, attaining 99% for the smallest drag coefficient. This shows, that for the loss of atmospheric kinetic energy, the ocean has a passive role. The loss of kinetic energy is of the same order of magnitude for all drag coefficients. The main part of the kinetic energy lost by the atmosphere in the air-sea interaction is dissipated. Indeed, only 3 percent is transfered to the ocean for the highest drag coefficient, it decreases to 0.06 percent for the smallest drag coefficient. This can again be explained by the lower speeds in the ocean as compared to the atmosphere and by the non-alignment between the local velocity vectors.

The ocean gains energy from the atmosphere, whenever the absolute value of the angle between the ocean current and the shear force exerted by the atmospheric wind is smaller than 90^o. Note that the direction of the shear force is aligned with the difference of the atmospheric wind vector and the ocean current vector. For the smaller drag coefficient the ocean gains energy from the atmosphere over 58% of its surface area, against 77% for the highest drag coefficient (table 12.1). This is explained by the stronger coupling between the atmosphere and ocean dynamics at higher drag coefficients.

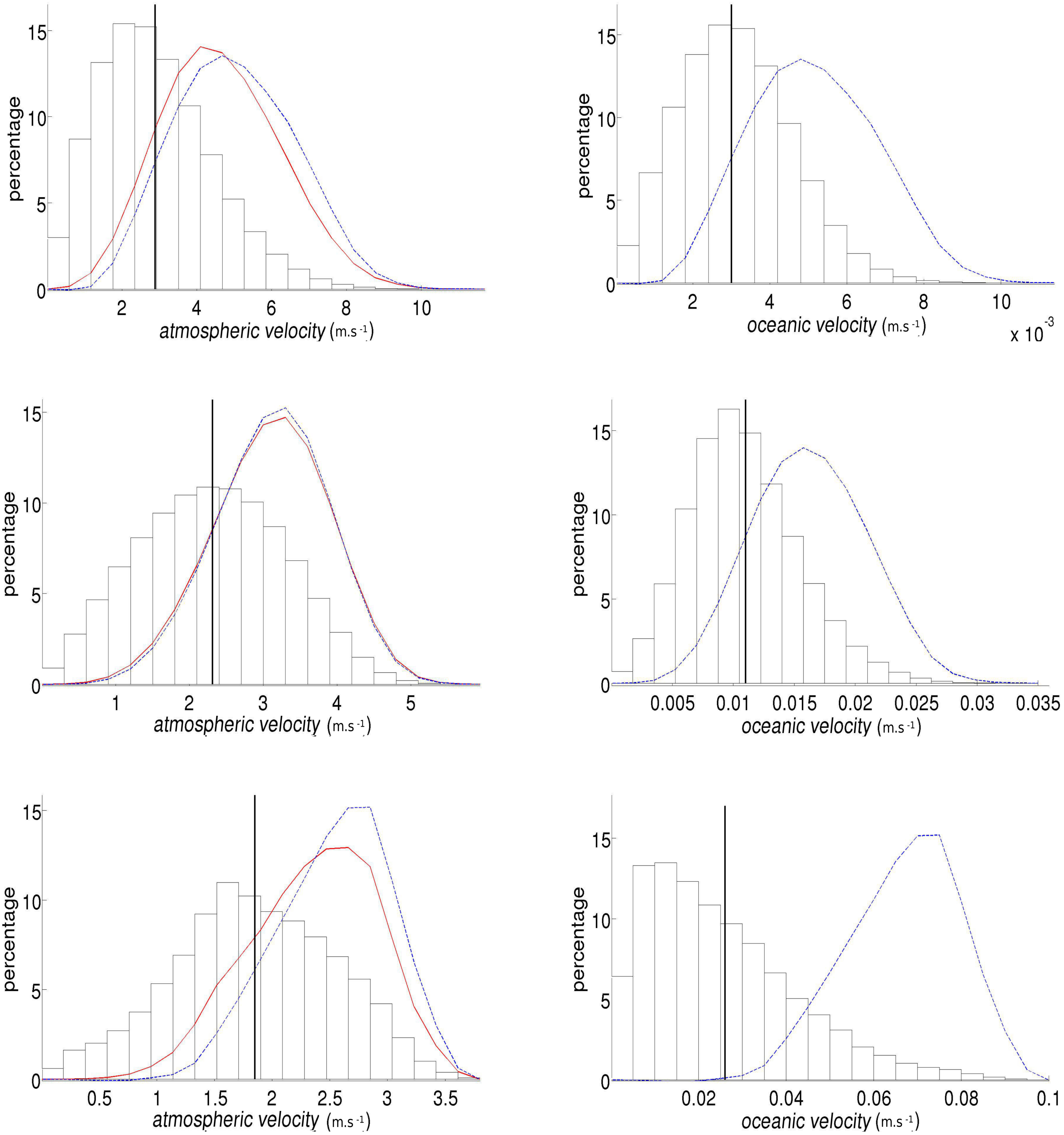

Figure 12.3: Percentage of surface area for a range of speed (histogram) for the atmosphere (left row) and the ocean (right row) for different values of the drag coefficient$C_d = 1\times10^{-4}$ at the top, $C_d = 4\times10^{-4}$ in the middle, and $C_d = 8\times10^{-4}$ at the bottom. The curves superposed give the power input calculated with the consistent formulation for the ocean (red-full) and lost for the atmosphere (blue-dashed) corresponding to the specific range of speed.

Fig 12.3 shows histograms of the wind speeds (left) and the ocean speeds (right). Superposed is the percentage of energy lost by the atmosphere for the corresponding speed range. The percentage of the energy gained by the ocean for the corresponding speed range is shown by the blue curve. The thick vertical line is the mean velocity. Due to the cubic law for the energy loss, the atmosphere loses its power at its high atmospheric speeds (fig 12.3). A comparison of the real energy loss to its approximation calculated with the mean velocity ($\overline{Pa} = \rho^a C_d \overline{u^a}^3$), shows that it underestimates the energy loss by almost a factor of one-and-a-half for the lowest drag coefficients and provides a good estimate for the largest (table 12.1).

The power input to the ocean is principally at the same atmospheric velocities at which the atmosphere loses energy, as is seen in fig. 12.3, where the red full line and the blue dashed line are similar in the figures corresponding to the atmospheric speeds (left column).

The power input to the ocean (fig 12.3, right column) shows a strong dependence on the drag coefficient C_d. For the lowest C_d value, 14 % of the fastest ocean speeds contribute half of the power input. For the largest C_d, this is achieved by only the fastest 3 % of ocean speeds. An explanation of this is an increased correlation between oceanic and atmospheric velocities for higher drag coefficients (see below). This result questions the significance of mean wind and current speeds when the power input is estimated. Indeed, as a rule of thumb, the power input from the atmosphere to the ocean is often estimated based on the mean wind and ocean speeds. In this estimation not only the correlations of the local wind and ocean speeds are neglected, but also the angle between the corresponding velocity vectors. The estimated value is compared to the exact value in table 12.1. For the highest drag coefficient the estimated value is 16% lower than the true value, while it is 3 times higher for the smallest drag coefficient (table 12.1). The higher value of the estimate is explained by the fact that it neglects the non-alignment between atmospheric wind and the ocean currents. The non-alignment is highest for the lower values of the drag coefficient. The lower value of the estimate is explained by the correlation of the magnitudes of the atmospheric and oceanic speeds.

Performing a log-log plot of the power-input to the ocean (averaged in space and time) as a function of the drag coefficient (fig 12.4) we see, that it is close to a quadratic law. Note, that the drag coefficient has a stronger than linear influence on the power input to the ocean as a higher drag coefficient increases the shear force and the velocity in the ocean and the power-input is the (vector) product of the two. A higher correlation between atmosphere and ocean velocities for higher drag coefficients further increase the power input.

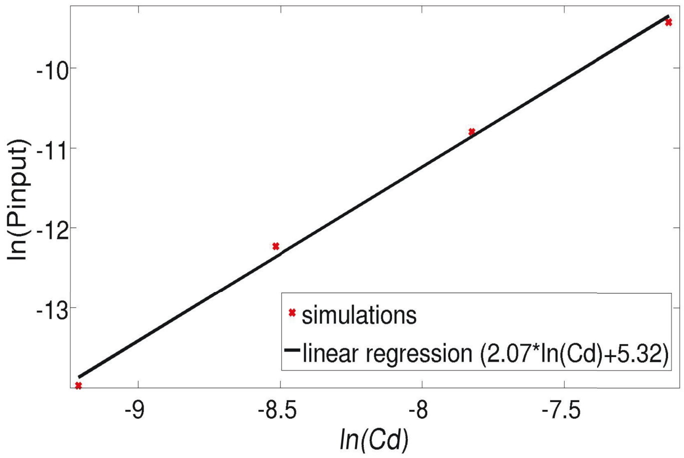

Figure 12.4: Log-log plot of the mean power input (P) as a function of the drag coefficient.

12.3 Vorticity correlation between the atmosphere and the ocean:

Table 12.2: Variance and spatial average of the vorticity in the ocean and in the atmosphere for an instantaneous snapshot (after 2675days) above and for a temporal average over 1000 days (below).

C_d	1×10^{-4}	2×10^{-4}	4×10^{-4}	8×10^{-4}
Instantaneous				
mean of atmospheric vorticity (s^{-1})	2.76×10^{-11}	3.04×10^{-11}	-3.22×10^{-11}	-3.02×10^{-11}
mean of oceanic vorticity (s^{-1})	-1.10×10^{-12}	-1.16×10^{-12}	-1.17×10^{-12}	-1.06×10^{-12}
variance of atmospheric vorticity (s^{-2})	3.28×10^{-10}	3.35×10^{-10}	2.77×10^{-10}	1.71×10^{-10}
variance of oceanic vorticity (s^{-2})	1.35×10^{-15}	4.43×10^{-15}	1.49×10^{-14}	2.37×10^{-13}
ratio between the big and the small half axes of the ellipse	1.48	1.74	2.28	2.24
slope of principal axis	2.03×10^{-3}	3.64×10^{-3}	7.33×10^{-3}	3.73×10^{-2}
1000 day average				
mean of atmospheric vorticity (s^{-1})	5.98×10^{-9}	-7.13×10^{-13}	-7.39×10^{-13}	-8.20×10^{-13}
mean of oceanic vorticity (s^{-1})	-8.97×10^{-10}	4.20×10^{-14}	1.74×10^{-13}	-1.54×10^{-13}
variance of atmospheric vorticity (s^{-2})	3.60×10^{-11}	5.85×10^{-11}	9.90×10^{-11}	1.60×10^{-10}
variance of oceanic vorticity (s^{-2})	9.58×10^{-16}	3.25×10^{-15}	1.18×10^{-14}	1.97×10^{-13}
ratio between the big and the small half axes of the ellipse	3.66	4.91	5.45	2.57
slope of principal axis	5.17×10^{-3}	7.45×10^{-3}	1.09×10^{-2}	3.52×10^{-2}

The normalized bi-variate probability density function (BV-PDF) for the atmospheric and the oceanic vorticity is used, to study the correlation between the dynamics in the ocean and the atmosphere. It is obtained by first subtracting the mean-value and then normalizing the atmospheric and oceanic vorticity by their respective standard deviation, before considering the correlations. For an instantaneous snapshot after 7 years, and the smallest drag coefficient, the isolines of the probability density function and the overlayed correlation ellipse appear almost circular (fig 12.5). Indeed the ratio between the two principal correlations is 1.48 (table 12.2), close to 1 which is the value for a perfect decorrelation.

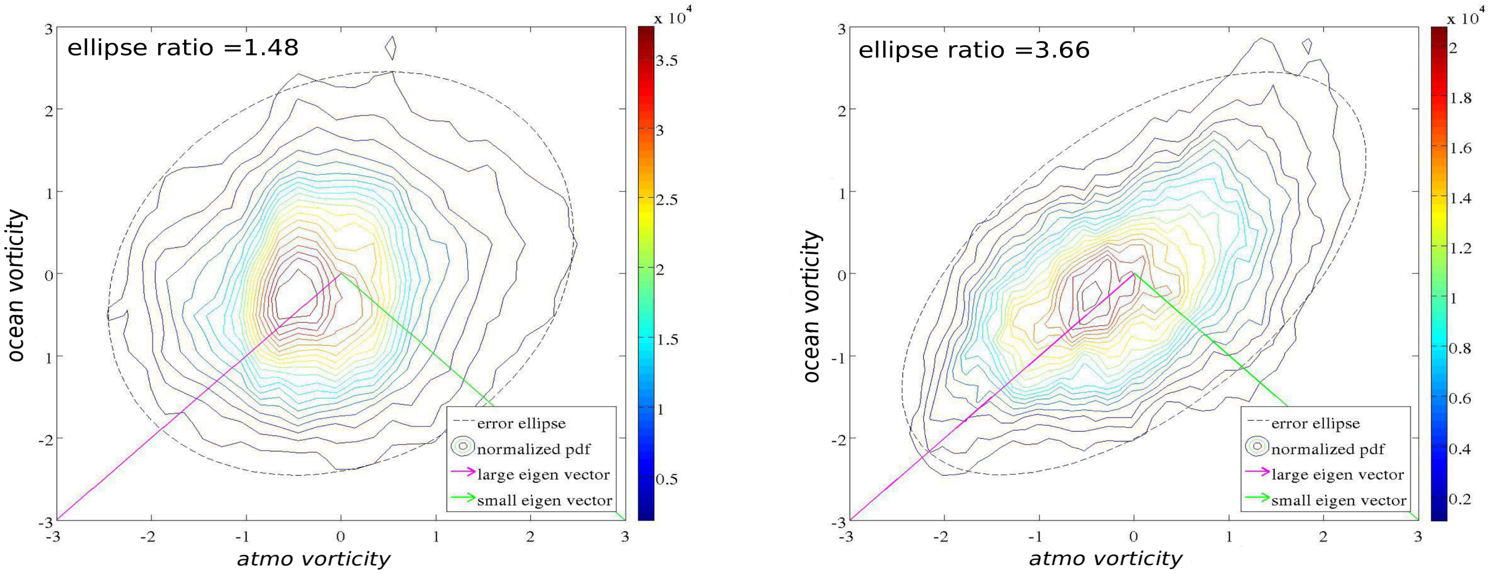

Figure 12.5: Normalized probability density function for C_d=1×10^{-4} for the instantaneous snapshot after 2675 days (left) and for the mean temporal vorticity (right).

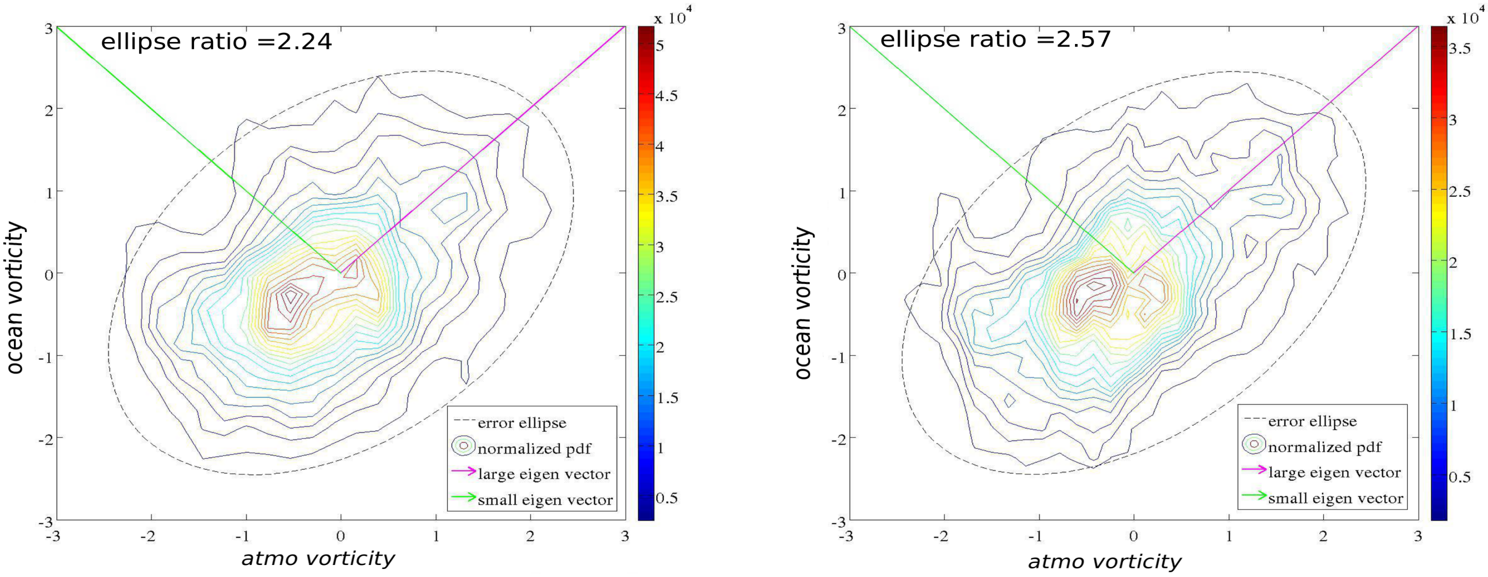

Figure 12.6: Normalized probability density function for C_d=8×10^{-4} for the instantaneous snapshot after 2675 days (left) and for the mean temporal vorticity (right).

This shows that there is only a feeble correlation between the atmospheric and oceanic vorticities. The correlations increases for the drag coefficients $C_d = 2\times10^{-4}$ and $C_d = 4\times10^{-4}$ before slightly dropping to 2.24 for $C_d = 8\times10^{-4}$. For the vorticities averaged over

1000 days the cross-correlation is higher than the instantaneous values. The ratio between the two principal correlations is more than 2 times higher than for the instantaneous snapshot (table 12.2) for the lower three drag coefficients, confirming the above mentioned observation that, when the fast variations of the atmosphere are filtered out the correlation between the ocean and the atmosphere is substantial. For the highest drag coefficient the dynamics is qualitatively different: the time variability, in the atmosphere and the ocean, is low as the dynamics is in a quenched state (see next section) and the cross correlation increases only by 15% when averages, rather than instantaneous values are considered.

When the normalized BV-PDF is considered the slope of the principal axis, which is the ratio of the standard deviation of the ocean and the atmosphere, is diagonal by definition (see Figs. 12.5 and 12.6). In the non normalized case it establishes a correspondence between the vorticity in the two media. The slope of the first principal axis is about two times stronger for the temporal mean than for the snapshot, for the three smaller drag coefficients. For the largest drag coefficient the two slopes are identical as there is no variation in time.

12.4 Spatial versus Temporal Variability of the Vorticity

In this part we study the variability in space and time of the vorticity field in the atmosphere and the ocean as a function of the drag coefficient. We need to define two different types of average: a spatial average and a temporal average. The temporal average of the vorticity has already been defined in the first part. It is the average of the vorticity on 1000 days denoted by $\langle \zeta^k \rangle_{1000}$. Where k corresponds to the ocean or the atmosphere.

The forcing applied to our periodic domain repeats itself 4 times in the x- and in the y-direction, leading to 16 identical cells. Furthermore, rotations of angles 90, 180 and 270 degrees do not change the forcing. The discrete symmetry group of the forcing has therefore 64 members. The dynamics in the atmosphere and the ocean, does not exhibit this periodicity, as it is not present in the initial conditions and as the system is chaotic. There are 4×4 identically forced squares present in the domain and we expect to find the periodicity of the forcing in the averages of dynamical quantities as there is a priori no reason to suppose that averages differ from one square to another once the initial conditions are "forgotten". That is, we suppose the system to be ergodic, meaning that ensemble averages and time averages coincide.

For the calculation of the spatial average we use the full symmetry group with 64 members. We calculate the average over all members of size $1000km \times 1000km$, and continue it periodically over the large domain of size $4000km \times 4000km$. This discrete spatial average is denoted by $\overline{\zeta^k}^{64}$.

To calculate the variability we also need to define the spatial variance:

$$var(a) = \frac{1}{n_x n_y} \sum_{i,j=0}^{n_x,n_y} (a_{i,j})^2,$$

where a is a matrix of size $n_x \times n_y$.

With all these terms the spatial variability can be defined by:

$$VarS^k = var(\langle \zeta^k \rangle_{1000} - \overline{\langle \zeta^k \rangle_{1000}}^{64}).$$

The space variability reveals the difference obtained when we reproduce the experiment with a little initial perturbation.

The temporal variability represents the evolution of the variable in time, it can be defined by:

$$Vart^k = \langle var(\zeta^k - \langle \zeta^k \rangle_{1000}) \rangle_{1000}$$

The total variability is written:

$$VarTot^k = \langle var(\zeta^k - \overline{\langle \zeta^k \rangle_{1000}}^{64}) \rangle_{1000}$$

It can be shown that the total variability is the sum of the spatial and the temporal variability:

$$VarTot^k = VarS^k + Vart^k$$

Table 12.3: Variability in space (varSpat) and time (vartemp) for the four drag coefficient for the ocean and the atmosphere.

C_d	1×10^{-4}	2×10^{-4}	4×10^{-4}	8×10^{-4}
varTota ($1/s^2$)	3.48×10^{-10}	2.77×10^{-10}	1.76×10^{-10}	9.57×10^{-11}
varToto ($1/s^2$)	8.64×10^{-16}	1.69×10^{-15}	4.86×10^{-15}	2.16×10^{-13}
varSpata ($1/s^2$)	6.17×10^{-12}	3.89×10^{-12}	5.69×10^{-12}	8.32×10^{-11}
varSpato ($1/s^2$)	3.46×10^{-16}	7.65×10^{-16}	2.25×10^{-15}	1.79×10^{-13}
vartempa ($1/s^2$)	3.43×10^{-10}	2.73×10^{-10}	1.70×10^{-10}	1.27×10^{-11}
vartempo ($1/s^2$)	5.18×10^{-16}	9.30×10^{-16}	2.60×10^{-15}	3.63×10^{-14}

The results, for the four drag coefficient, are plotted in an histogram for the atmosphere (fig 12.7 (left)) and for the ocean (fig 12.7 (right)). In the atmosphere, the total variability decreases when the drag coefficient increases. The spatial variability is small ($\ll 3\%$) for the the three lower drag coefficients but skyrockets to 86% for C_d=8 × 10^{-4} of the total variability, showing that the dynamics changes qualitatively when the drag coefficient is increased from C_d=4 × 10^{-4} to 8 × 10^{-4}. In the ocean, the total variability is very low for the smallest three drag coefficient (order of $10^{-15}\mathrm{s}^{-2}$) with again a strong dominance of the the temporal variability. The case with the strongest drag coefficient is again very different from the lower ones. It has a total variability around hundred times larger with more than three quarters due to the spatial variation. The disorder in the highest drag coefficient case is dominated by spatial disorder (quenched disorder), whereas the three other cases, the temporal disorder prevail (annealed disorder).

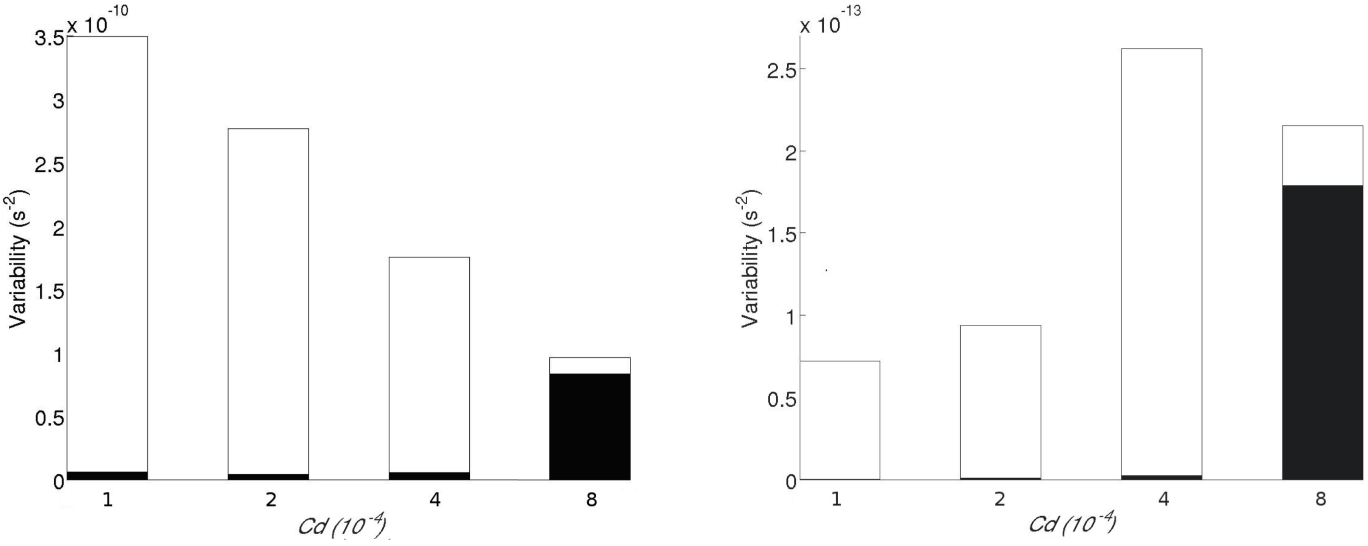

Figure 12.7: Space variability (black) and time variability (white) for four values of the drag coefficient in the atmosphere (right) and in the ocean (left). For the ocean the variability are multiplied by 100 for the three lower drag coefficients.

Chapter 13

Discussion

From a kinetic-energy point of view the atmosphere-ocean system is driven by the injection of kinetic energy into the atmosphere. The system losses energy due to friction at the atmosphere-ocean interface (and to a lesser extent by horizontal friction, not discussed here). A small fraction of the kinetic-energy lost by the atmosphere drives the ocean. The ocean has an almost perfectly passive role, absorbing energy from the atmosphere. Concluding that the ocean has no influence on the dynamics of the atmosphere is however wrong, as demonstrated above. The amount of energy taken out of the atmosphere at its lower interface depends only slightly on the ocean dynamics, but due to the persistence of the ocean dynamics it ultimately governs the long-time dynamics of the atmosphere. In this respect it is difficult to dissect the atmosphere dynamics, the ocean dynamics and their interaction. One should rather see the combined system, interactions and correlations depend on the time scale considered.

The difference of the power input estimated with the wind speeds, only, to the consistent calculation, based on the shear between the atmosphere and the ocean, is found to be small. This is different to the work by Duhaut and Straub [2006], who treated a large scale double gyre circulation. They have a constant-in-time wind velocity and the double gyre configuration that leads to a strong boundary current that separates from the boundary and penetrates into the interior of the domain with large ocean velocities of the order of 1m/s. In our calculations periodic boundary conditions are used and no accumulation of energy at a boundary is possible. Sverdrup theory, based on the conservation of vorticity, predicts velocities for an ocean subject to a large scale wind-forcing constant in time, of only a few centimeters per second. In our calculations the forcing by the atmosphere on the ocean is (for the three lower values of the drag coefficient) constantly changing magnitude and direction, in time-and-space. This temporal and spatial incoherence in the forcing explains the feeble ocean speeds in our model and thus also the smaller differences between the correct implementation and its approximation.

For the highest drag coefficient, the atmosphere injects more energy into the ocean, this leads to stronger ocean currents. Stronger ocean currents together with the higher drag coefficient have an increased influence on the atmosphere, leading to an alignment of the instantaneous atmospheric winds with the ocean currents. This not only leads to stronger ocean currents but also to a reduction of temporal variability in the atmosphere, which furthermore reduces the temporal variability in the ocean. This positive feedback finally causes a strong oceanic current and a strong collocation of atmospheric and oceanic features. The disorder in the highest drag coefficient case is dominated by spatial disorder (quenched disorder), whereas in the three other cases, the temporal disorder prevails (annealed disorder). An astonishing result of our calculations is that the change between the two kinds of disorders seems to happen abruptly and it can not be excluded that it resembles a phase change. The transition happens when the non-dimensional stability parameter (see *e.g.* Chen and Jirka [1997])

$$S = \frac{C_d L^a}{H^a}$$

comparing the drag force to the advection increases towards unity. Even more striking is that the dynamics in the ocean and atmosphere does not converge to the purely periodic state imposed by the forcing but to a spatial disordered state. Such kind of behavior is commonly observed in condensed matter physics, where it is called glass transition (see *e.g.* Stillinger and Debenedetti [2013] and Berthier and Biroli [2013]), it occurs around a glass transition temperature, at which the internal relaxation times begin suddenly to exceed the practical measurement times and, furthermore, the state becomes protocol dependent. When the material is performing a glass transition it does not, or only very very slowly, converges to a periodic (crystalline) state. In our case the drag coefficient plays the role of the control parameter.

The quadratic dependence of the power input to the ocean is important for ocean dynamics as this small-scale energy contributes not only to the mixing in the ocean at the scale where it is injected, but will cascade to larger scales in an inverse energy cascade.

Chapter 14

Conclusions

The majority of results about the air-sea interaction were expected: the passive role of the ocean in the energy transfer; the weak dependence of the air-sea energy transfer on the ocean velocities and its increase with the drag coefficient; and the higher correlation of the averaged vorticities as compared to instantaneous part. The value of the present work lies in the quantification of the air sea interaction at the synoptic- and mesoscale.

The increased correlation of the vorticity between the atmosphere and the ocean (Figs. 12.5 and 12.6) when a temporal average rather than instantaneous values are considered shows, that even when such a correlation is hidden on instantaneous snapshots due to the fast turbulent dynamics of the atmosphere it emerges when averages are considered.

The most striking result is the glass transition in the dynamics of the atmosphere-ocean system when the drag coefficient is increased from $C_d = 4{\times}10^{-4}$ to 8×10^{-4}. For the higher drag coefficient, the time variability is largely reduced and the system is in a quenched disordered state. This is similar to the what happens in a glass transition, when the temperature is reduced below critical. The consequence of this is, that time averages are different from spatial averages, such that the system is no-longer ergodic. In studies of the earth system based on observations, ergodicity is often assumed, as there is only one planet. When studies are based on laboratory experiments or numerical simulations, experiments are continued until statistical quantities have converged, using again the ergodic hypothesis. To further investigate such transition analytically and/or numerically a simpler model is necessary.

In the calculations with the high drag coefficient the high instantaneous correlation between the vorticity in the atmosphere and the ocean (Table 12.3 see also Fig. 12.2), show that the ocean currents leave a definite imprint in the atmospheric winds leading to fine scale structures in the atmosphere. This suggest, that the fine scale structures of the ocean dynamics which have recently been exposed by fine resolution satellite observations can influence the atmospheric dynamics through momentum transfer, even when heat-fluxes are excluded.

The genesis of hurricanes is strongly influenced by air-sea interaction, mostly through the heat exchange but also by the frictionally induced convergence (Charney and Eliassen [1964]). The near surface processes such as mesoscale positive vorticity anomalies are important in the bottom-up scenarios of hurricane genesis (Fang and Zhang [2008]). The capture of atmospheric eddies by oceanic structures and their co-evolution can be an important ingredient in this context. To further investigate the co-evolution of atmospheric and oceanic vorticity anomalies and their statistical properties, a study with a simplified vortex model is currently undertaken.

Part IV

Spin-up of the ocean dynamics due to air-sea interaction around an island

Chapter 15

Introduction

Coast lines and islands are observed to be key regions for generating dynamic mesoscale and small scale structures in the ocean and the atmosphere. Observation networks enable us to see features of both oceanic and atmospheric circulations within these regions (Chelton et al. [2004], Capet et al. [2004]). In the atmosphere orographic effects are present on all horizontal scales and the strong temperature gradient between the land and the ocean surface generates coastal winds subject to a daily cycle. Furthermore, the bottom friction of the atmospheric dynamics varies abruptly and over a few orders of magnitude between the land and the ocean surface. It leads to a strong wind stress curl observed surrounding many islands and coasts all over the world (Chelton et al. [2004], Barton et al. [2000]). Numerous examples of mesoscale features generated by coast lines (as the Pacific coast of central America, Chile, California coast,..) and islands (Hawaii, Madagascar, Philippine, Canary..) are visible in divergence and curl measurements derived from satellite observations (Chelton et al. [2004], Renault [2012], Capet et al. [2004]). In the ocean which is forced by the atmosphere, an Ekman transport is generated which then acts on the interior ocean dynamics through its convergence and divergence (Ekman pumping). Moreover, the orographic effect inducing wind shadows and wind jets leads to eddy generation in the lee of islands (Couvelard et al. [2012], Pullen et al. [2008]), which plays a capital role in the upper ocean circulation. In particular a pair of strong cyclonic and anticyclonic eddies have been observed to emerge on the lee side of the islands (Chavanne et al. [2010], Lumpkin [1998], Pullen et al. [2008]). Mesoscale and small scale currents contribute significantly to the transport and mixing of heat, energy, and water masses in the ocean. In particular, the surface currents and surface eddies, located in the upper hundred or two hundred meters, play a vital role in exchanges between the coastal zone and offshore area. Wind stress curl also generates upwelling and downwelling, that is vertical transport, which affect ocean stratification. The heart of a cyclonic eddy is one example, which leads to a lift of cold water, rich in nutrients, increasing the biological production (Kuwahara et al. [2008]). They are conveyors of momentum flux, energy, mass, and biological and chemical properties.

Oceanic mesoscale eddies generated around islands and coastlines have received great interest from observational programs due to their impact on local biology (80% of fishing is carried out in coastal regions) and chemistry (high presence of chlorophyll-a) (Barton 2005). Regions with strong wind stress curl variations have been observed throughout the coastal regions and their mostly unknown impact can have significant effects on larger scale ocean dynamics. Understanding the formation and the evolution of the wind stress curl generated near the coastline and their contribution to eddy formation, is essential to characterize the exchanges in the ocean, with the atmosphere and the movement of biological species and pollutants.

In today's climate models with a coarse horizontal and vertical model resolutions, both regional and global scale climate features are resolved. Nevertheless, the resolutions of climate and oceanic/atmospheric global circulations models are not sufficient to describe the interaction of the flow with an island smaller than a few hundred kilometers. Oceanic circulation models are mostly forced by wind estimates from Numerical Weather Prediction models (NWP). An important consideration is that orographic effects induced by small scales in the orography are absent in the wind stress field product from NWP models. Indeed they have a resolution of about 50km which does not allow for incorporating islands smaller than a few hundreds of kilometers and therefore, does not reproduce the wind-wake generated by the island orography. The atmospheric wake generated by island orography is not sufficiently resolved by most of the wind products and therefore neglects or underestimates the action on the ocean dynamics. The lack of resolution in previous studies makes it difficult to understand the time and spatial scales of the wind variations and thus the response of the upper ocean layer. Some studies on specific islands are recently made with more accurate wind products, and finer oceanic resolution. Satellite derived wind products and coarser numerical models have been used in order to assess the role of atmospheric wind forcing on the generation and propagation of oceanic eddies. For example, Calil et al. [1993] use Quickscat (25km of resolution), to correctly resolve wind products in the lee of the Hawaiian islands. For the Madeira island, which is smaller, Couvelard et al. [2012] choose to use the Weather Research and Forecasting (WRF) with a finner resolution of 6km, to realistically reproduce the wind wake due to the mountains.

Jia et al. [2011] and Barton et al. [2000] show that two mechanisms can generate eddies in the wake of an island. The first is by an oceanic flow around an oceanic barrier, and the second is by an atmospheric flow (like trade wind) around an atmospheric barrier which induces surface wind shear and so oceanic eddies in the upper oceanic layer. A large part of studies deals with the first case. Numerous works deal with Ekman transport around an island induced by a constant atmospheric forcing (Spall and Pedlowsky [2012] and Pedlowsky [2013]). The presence of an island interrupts the uniform Ekman transport and can lead to mesoscale structures. In the presence of an island immersed in a constant depth ocean, with a uniform Ekman flow driven by a uniform and constant northward wind stress, upwelling at the eastern side and downwelling at the western side of the island are generated (Spall and Pedlowsky [2012]). In all these studies, the atmosphere acts as a constant large scale forcing on the ocean and the island has no effect on the atmosphere, so the wind wake generated by the island is neglected in the friction applied to the ocean.

Jia et al. [2011] demonstrated, with a study on the Hawaiian islands, that eddy generation by an ocean barrier needs strong large scale flows and only contributes to an insignificant amount of eddy kinetic energy (values obtained are far lower than observations). Recent work have shown that adequate wind forcing with an atmospheric wake, is important to reproduce the observed mesoscale vortices in the lee of the islands (Calil et al. [1993]). The oceanic wake due to bathymetry creates only a low intensity curl due to the Ekman transport. The second process induced by an atmospheric barrier (that is orography) is more consistent with the observations and appears as the main contributor to oceanic eddy generation.

All the studies with a consistent wind product show that the eddy occurrence and intensity coincide with periods of strong wind-wake episodes (Jia et al. [2011], Couvelard et al. [2012], Pullen et al. [2008]). The steady monsoon winds (during the winter season) interacting with the Philippine islands can form stationary lee eddies of about 100-200km of diameter, with a regional distribution of cyclones to the south and anticyclones to the north of a line separating positive and negative wind stress curl extending west (Pullen et al. [2008]). A recent model by Calil et al. [1993] has shown that stronger cyclonic eddies were generated when stronger and persistent trade wind forcing was present at the Hawaiian island. Around the Madeira island, oceanic surface kinetic energy and enstrophy are found to increase during the strong wind wake episodes that are dominant during summer months (Couvelard et al. [2012]). The study also concluded the absence of eddy formation in the lee of the Hawaiian Big Island during windless periods.

The combination of the ocean and atmosphere circulation systems makes the region to the lee of the islands more energetic in mesoscale eddies variability than the surrounding areas, and the high eddy activity is closely related to the wind stress curl. For the Hawaiian islands, it is demonstrated that the strong atmospheric subtropical high pressure system generates a consistent trade wind pattern blocked by the Hawaiian chain orography. This creates dipoles of positive and negative wind stress curl in the lee of the islands. This mechanism drives divergent and convergent Ekman transport which is compensated by vertical water motions which in turn move the thermocline up and down resulting in cyclonic and anticyclonic eddies (Lumpkin [1998],Yoshida et al. [2010]). This wind stress curl mechanism has been observed for islands and coasts around the world (Chelton et al. [2004], Pullen et al. [2008], Chavanne et al. [2010]).

In all the cited publications, a specific geographic location is chosen for the study of eddy generation with complex island geometry and forcing due to wind products derived from satellite measurement. In recent years strong evidence on ocean and atmosphere dynamics below the synoptic scale has been gathered from observations. Idealized studies and analytical calculations, relating observed phenomena to fundamental dynamical processes are scant. Bridging the gap between fundamental processes studied analytically or semi-analytically on one side and realistic simulations and observations on the other side, is key to increasing our scientific understanding (Wirth [2010]). Here I study how these eddies are generated, and how they evolve in a very idealized but consistent coupled ocean-atmosphere model when the atmosphere is subjected to a constant atmospheric forcing (in time & space).

This part studies the influence of atmospheric forcing, due to a turbulent quadratic friction law, on the oceanic mixed layer at mesoscale, in the presence of an island. The two superposed shallow water models, one for the atmosphere and one for the ocean, including the island and the ocean-atmosphere coupling is introduced in the next chapter (session 17.1). Experiments are first performed for a 1 way ocean-atmosphere coupling, in cases in which the atmosphere feels or does not feel the island (session 17.1). Then simulations are done for different values of atmospheric forcing and oceanic viscosity. The transport around the island, the dynamic evolution and the injection and generation of vorticity are further investigate in Part IV, session 17.2. Results are summarized and discussed in chapter 18.

Chapter 16

Shallow-water model

16.1 Physical model

The following model is similar to the one used in the first two parts (part I). The model consists of two superposed homogeneous fluid layers, a shallow layer for the lower atmosphere above an ocean surface layer. The average thicknesses are respectively $H^a = 1000m$ and $H^o = 200m$. The actual layer thicknesses $h^a(x, y, t)$, $h^o(x, y, t)$ vary over time and space. The ocean surface layer superposes a motionless layer of higher density and of infinite depth. Similarly, a motionless layer of air of a lesser density superposes the shallow atmosphere layer. Layers have an average density of $\rho^a = 1kg/m^3$ and $\rho^o = 1000kg/m^3$. The fluid motion considered extends over a period of many days and so the model must take into account the Earth's rotation. Using the f-plane approximation I set the Coriolis parameter $f = 5 \times 10^{-5}\mathrm{s}^{-1}$, a typical value at tropical-latitudes (e.g. Hawaii islands). It is consider constant in all the domain and I thus neglect Rossby waves and β-plumes (important for the ocean dynamics around Hawaii). As β=0, I do not have the south or north and the east or west directions. In all this part I will use the terms up- and down-wind and left and right side of the island as defined in the fig. 16.1. The f-plane approximation allows for using periodic boundary conditions in both horizontal directions, which simplifies the numerical implementation.

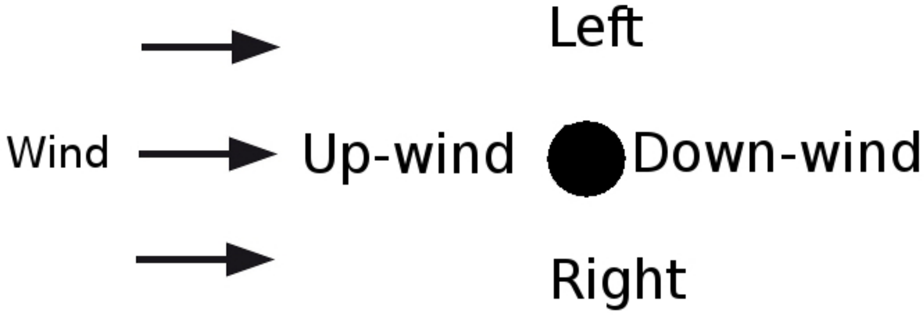

Figure 16.1: Scheme of the direction terms around the island

A circular island of 100km diameter is present in the ocean. It is imposed through a no-slip boundary condition. In the atmosphere the island can be represented (or not), by increasing the drag coefficient of a factor of 100.

16.2 Mathematical model

$$\begin{aligned}
\partial_t u^k + u^k \partial_x u^k + v^k \partial_y u^k - f v^k + g^k \partial_x h^k &= \nu^k \nabla^2 u^k + F_x^k + \tilde{F}_x^k \\
\partial_t v^k + u^k \partial_x v^k + v^k \partial_y v^k + f u^k + g^k \partial_y h^k &= \nu^k \nabla^2 v^k + F_y^k + \tilde{F}_y^k \\
\partial_t h^k + \partial_x [h^k u^k] + \partial_y [h^k v^k] &= 0 \\
&+ \textit{Boundary conditions}
\end{aligned}$$

Where $k = a, o$ stands for the atmosphere and the ocean, respectively. The parameters g^a and g^o are the reduced gravity of the atmosphere and of the ocean (i.e., the gravitational acceleration multiplied by the fractional density difference between the two layers). They are respectively set to $0.8 m/s^2$ and $2.10^{-2}\ m/s^2$.

The typical horizontal scale is the Rossby radius of deformation $Rd^k = \sqrt{g^k H^k}/f$. The Rossby radius is one order of magnitude smaller in the ocean where $Rd^o = 40km$ than in the atmosphere where $Rd^a = 566km$. The domain size is $L_x = 4000km$ and $L_y =$ 1000km and there are periodic boundary conditions in both horizontal directions, in the atmosphere and the ocean. The atmosphere is subjected to a constant in time and space forcing. In the ocean $\tilde{F}^o$ is a damping to dissipate mechanical energy.

The two layers are only linked by frictional forces at the interface, parameterized by a quadratic drag law. The frictional acceleration between the two layers is defined by:

$$\begin{pmatrix} F_x^k \\ F_y^k \end{pmatrix} = \pm \frac{1}{\rho^k h^k} \begin{pmatrix} f_x^k \\ f_y^k \end{pmatrix}. \tag{16.1}$$

Where f_x and f_y are the surface forces depending on x and y.

$$\begin{pmatrix} f_x^o \\ f_y^o \end{pmatrix} = \rho^a C_d |u| \begin{pmatrix} u^o - u^a \\ v^o - v^a \end{pmatrix}, \tag{16.2}$$

with $|u| = \sqrt{(u^o - u^a)^2 + (v^o - v^a)^2}$. The shear applied to the atmosphere is the opposite to the shear applied to the ocean.

The drag coefficient is constant above the ocean ($C_d = 8.10^{-4}$ a classical value) (Stull [1988]). The drag coefficient is constant and 100 times higher above the island.

16.3 Numerical model

The horizontal domain of the ocean and the atmosphere is a rectangle of dimension $L_x \times L_y$ ($L_x = 4000km$ and $L_y = 1000km$). Periodic boundary conditions are used in both horizontal directions (f-plane approximation is used). The numerical grid is regular and contains $n_x \times n_y$ points. We choose $n_x = 1600$ and $n_y = 400$, for the 2D shallow water model. That is a fine spatial resolution $\Delta x = L_x/n_x = \Delta y = L_y/n_y = 2.5km$ is employed to well resolve the oceanic Rossby radius of deformation. The eddy viscosity of the layers ν^a and ν^o are constant in space and time (but are varied between different experiments), (see tab.16.1).

A finite volume method is used for the space discretization and a Crank Nicholson scheme is used for the time discretization. The time step is constraint by the CFL condition. As atmospheric waves are ten times faster than oceanic waves, it is the CFL condition for the atmosphere that sets the minimum time step $\Delta t = 30$s to well resolve the temporal evolution of the atmospheric dynamics.

The atmosphere sees the island as a location of increased bottom friction, where drag coefficient is 100 times higher (8×10^{-1}) than above the water. Simulations stop when the oceanic layer thickness drops below 30 meters at any location. For a thinner layer thickness, the turbulent dynamics in the surface mixed layer leads to entertainment of water from the deep layer and so the shallow water equations are no longer valid to described this physics, which could however be parameterized (see Wirth et al. [2002]).

16.4 Implementation

The implementation is made using OpenFOAM with a penalization method to represent the island in the ocean model. A mask is created for the island and I force the oceanic velocity to 0 at the location of the island. As common in penalization methods, a spurious residual velocity remains at the location of the island. We checked that it is always lower than 2×10^{-4}m/s the maximum speed in all the calculations.

16.5 Experiments Performed

All the experiments discussed here are listed in the table 16.1. We first present results from three experiments with different parameterizations of the momentum fluxes. The first case is for an atmosphere which does not feel the island and the ocean dynamics through the bottom friction. The second one is for an atmosphere which feels the island (friction coefficient is increased hundred fold as compared to the ocean) but does not feel the ocean dynamics through the bottom friction. The bottom friction of the atmosphere only depends on the atmospheric dynamics and the friction coefficient is constant. The third one is more consistent. The atmosphere feels the island through an increased friction coefficient and the ocean dynamics by considering the difference of the velocity in the calculation of the friction force.

In a second part I only use the most consistent case for the friction. Results from four numerical experiments which vary by the oceanic viscosity or the atmospheric forcing are shown. These characteristics are constant for each experiment.

In the four simulations discussed here, the viscosity in the ocean is $\nu^o = 1000 m^2/s$ or $\nu^o = 4000 m^2/s$ and the atmospheric forcing is $U^a = 5 m/s$ or $U^a = 10 m/s$. U^a denotes the wind speed in the calculation where the atmosphere does neither feel the island nor the ocean dynamics.

Simulations stop when the ocean layer thickness decreases below 30 meters. For lower layer thickness the turbulence in the surface mixed layer penetrates to the lower boundary of the layer leading to entertainment. This process is not resolved in our model. Continuing the integration for smaller layer thickness might be mathematically interesting but does not correspond to a physical situation.

Table 16.1: Experiments performed

simulation name	$U^a - wOI$	$U^a - wI$	U^a05_1000	U^a05_4000	U^a10_1000	U^a10_4000
atmosphere feels the ocean			✓	✓	✓	✓
atmosphere feels the island		✓	✓	✓	✓	✓
atmospheric forcing (m/s)	5	5	5	5	10	10
ocean viscosity (m^2/s)	4000	4000	1000	4000	1000	4000
length of experiment (days)	100	100	161	470	45	98

Chapter 17

Results

17.1 Qualitative description

17.1.1 Main processes of the ocean dynamics

I first discuss the three simulations $U^a - wOI$, $U^a - wI$ and U^a05_4000, which differ by the presence of the island for the atmosphere and the action of the ocean dynamics on the atmosphere (tab. 16.1).

When the atmosphere does not feel neither the island nor the ocean dynamics ($U^a - wOI$), the atmospheric wind is uniform in space and converges to a stationary state within few days. There is no vorticity injection by the bottom wind stress.

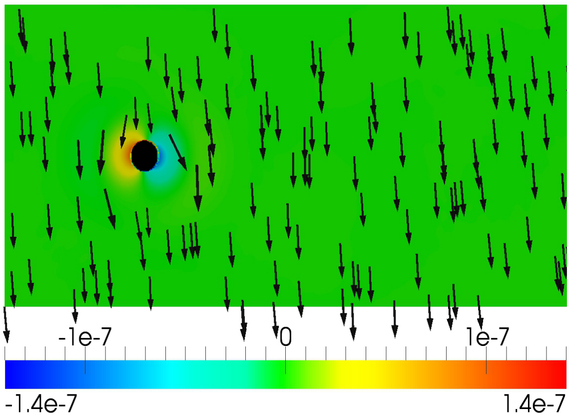

Figure 17.1: Oceanic vorticity (s^-1) and Ekman velocity without wind wake, for an atmospheric forcing corresponding to 5m/s and a viscosity of $4000 m^2/s$. Only 2500km of the domain, in the x-direction, is represented.

After one day, the wind stress applied to the ocean induces a small Ekman velocity in the ocean (2×10^{-3}m/s for an atmospheric forcing of 5m/s), to the right direction (fig.

17.1). The Ekman transport, in the ocean, is perpendicular to the wind forcing, to the right in the northern hemisphere. It is slightly disturbed by the presence of the island (dark disk in the figures). The friction with the coast line generates two insignificant boundary layers with positive and negative vorticity, respectively on the up-wind and down-wind side.

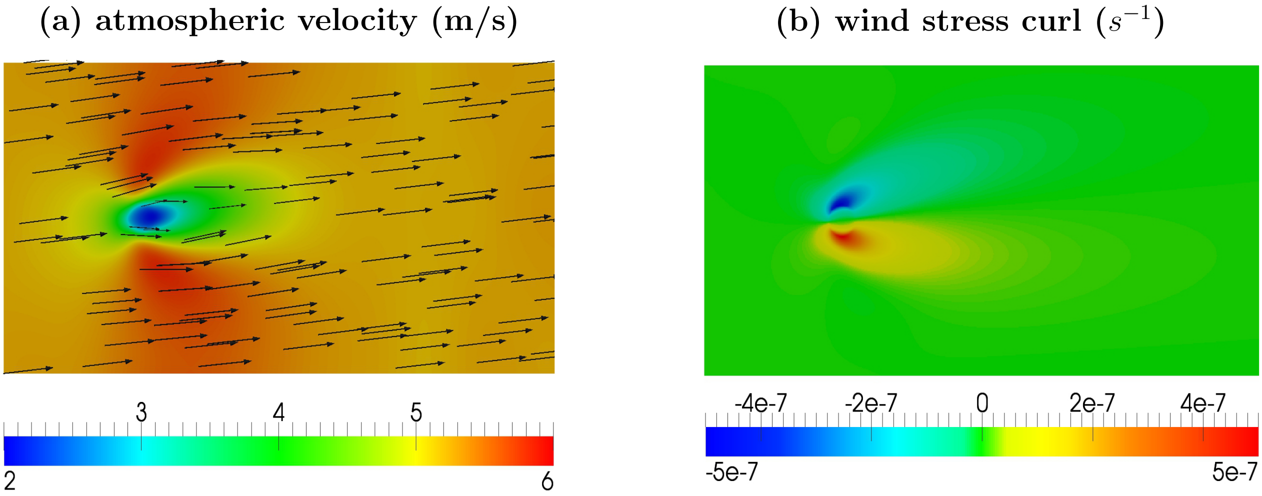
(a) atmospheric velocity (m/s)

(b) wind stress curl (s^{-1})

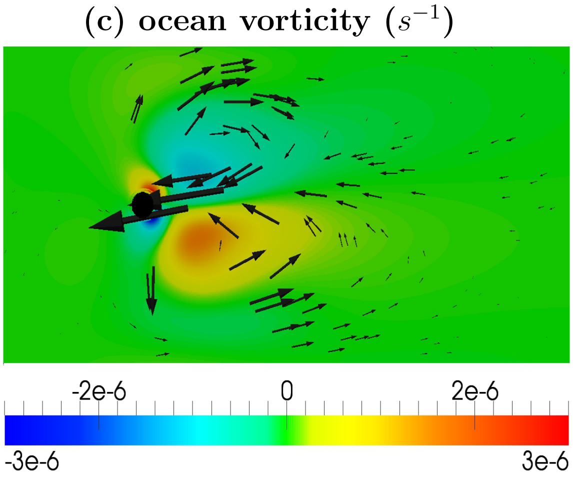
(c) ocean vorticity (s^{-1})

Figure 17.2: atmospheric velocity (a), wind stress curl (b) and ocean vorticity (c), in case of wind wake, for an atmospheric forcing of 5m/s and a viscosity of 4000m^2/s. Only 2500km of the domain, in the x-direction, is represented.

When the atmosphere does not feel the island but interacts with the ocean dynamics ($U^a - wI$), the atmosphere and ocean dynamics are almost identical to experiment $U^a - wOI$. Including the ocean dynamics in the bottom friction does not change the dynamics if the island is not taken into account in the atmospheric circulation, as the ocean speed stays insignificant.

When the atmosphere feels the island (U^a05_4000) a wind wake is created behind the island (fig 17.2.a), due to the difference of the drag coefficient above the water and the island (100 times higher). The atmosphere converges fast to a stationary state (fig 17.2.a). In the ocean, the Ekman velocity establishes, to the right direction, after one day. In this case, the wind wake induces a curl in the bottom wind stress downwind of the island, with an anticyclonic vorticity to the left side and a cyclonic vorticity to the right side (fig 17.2.b). This wind stress injects vorticity in the ocean and generates a large dipole structure in the wind wake (down-wind direction), after a few days. This pair of cyclonic and anticyclonic eddies includes a strong counter current between the two eddies ($\simeq$0.6m/s for an atmospheric forcing corresponding to 5m/s after a few months) (fig 17.2.c). Near the coast line of the island at its downwind side, a boundary layer is generated due to the no slip boundary condition. It generates negative vorticity to the left and positive vorticity to the right, caused by the motion along the island generated by the dipole. This dipole structure grows in time, and no stationary state is reached for the ocean dynamics. The Ekman velocity is insignificant as compared to the dipole velocity and the counter current (about 300 times faster).

The results of my simulations, with an idealized model, agree with existing simulations and satellite data characterizing regional oceanic eddy and surface wind wake properties. These simulations show that the modification of the atmospheric circulation and so the wind stress in presence of an island is the major process for the ocean dynamics around an island. The atmospheric wake induced by the island is the main reason for ocean eddy generation, (as in Jia et al. [2011],Couvelard et al. [2012]). Nevertheless, this phenomenon is only visible if the island is represented in the atmosphere and in the ocean, and so only if the model or the wind forcing resolves the island in the atmosphere (Capet et al. [2004]). Today many numerical studies, do not take into account small or medium size islands in the wind stress and study the disturbance due to the island in the ocean, only, which seems to be an insignificant part for the ocean dynamics.

17.1.2 Emergence of a secondary dipole dependent of the atmospheric forcing and Reynolds number

In this section, I compare the results from the four simulations, for which the atmosphere feels the island and the ocean dynamics (U^a05_1000, U^a05_4000, U^a10_1000 and U^a10_4000 (tab. 16.1)), and which vary by the strength of the atmospheric forcing and the magnitude of the ocean viscosity.
At the beginning, in all the simulations, the ocean dynamics is similar to this described previously (session 17.1.1, simulation U^a05_4000). The first step is the generation of an Ekman velocity after few hours to the right side, in the ocean, due to the wind stress in the x-direction. Subsequently the wind stress curl progressively induces a dipole with a

counter (directed up-wind) current in the wind wake after few days which extends and intensifies in time. When the strength of the dipole increases, an asymmetry appears. The shallower cyclone becomes stronger than the anticyclone, because of the decay of the ocean layer thickness in the cyclone which induces a more effective acceleration. This stronger acceleration for the cyclone leads to an even faster decrease in the layer thickness leading to a stronger acceleration...

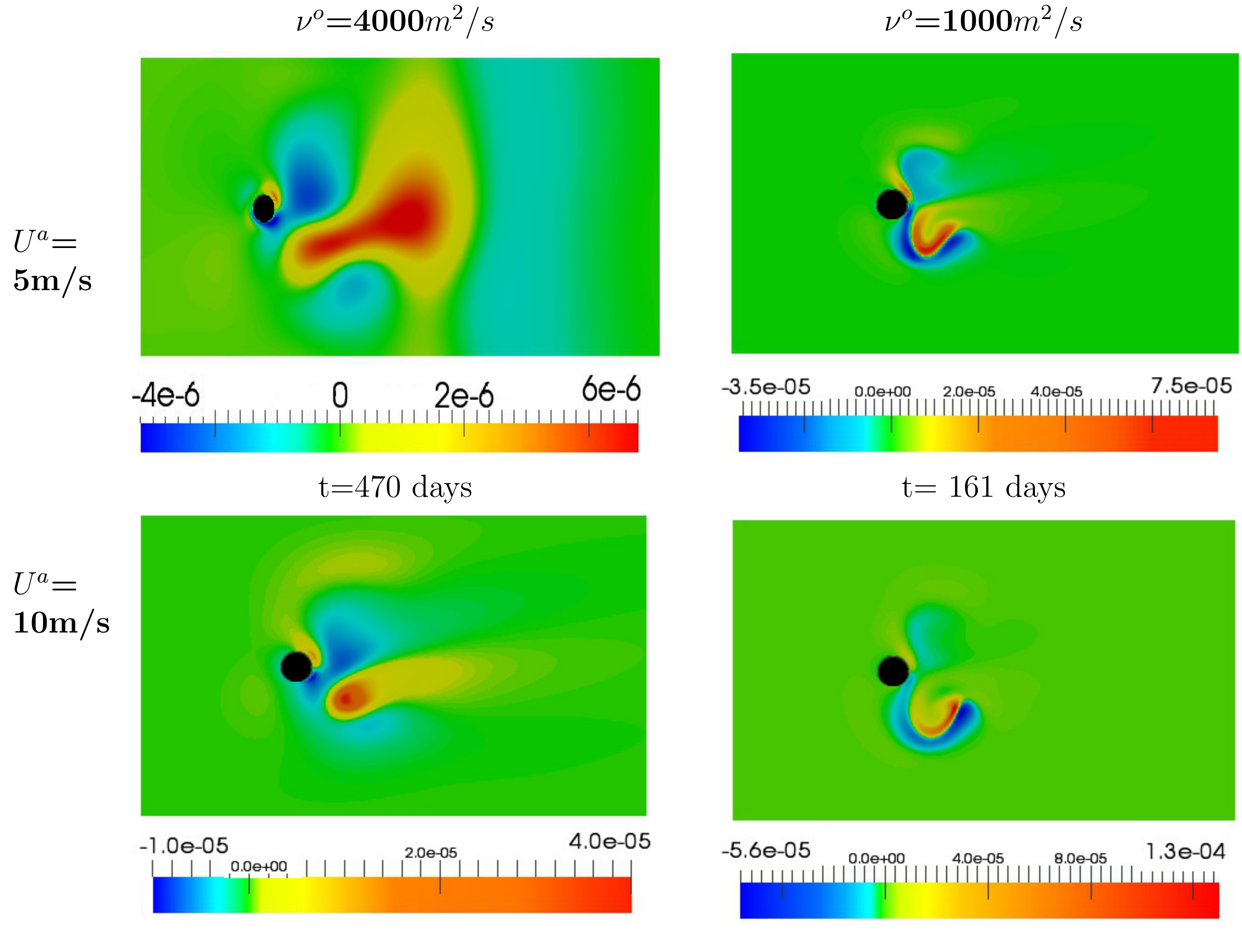

t=470 days t= 161 days

t=98 days t=45 days

Figure 17.3: Map of oceanic vorticity (s^{-1}) for the two atmospheric forcing and the two Reynolds number when the layer thickness reaches 30meters deep. Only the first 2500km in the x-direction are represented.

Two cases can be distinguished for the evolution of the dynamics, depending on the ocean viscosity used (fig 17.3). For the highest Reynolds number (smallest viscosity), a secondary dipole of smaller scale and higher intensity is generated. Due to the friction at the island boundary layer, a strong negative vorticity is generated along the island to the right side, and then displaced by the main cyclonic eddy. The same process occurs, at the left, for the positive vorticity but it is lower due to the higher layer thickness and

the asymmetry of the main dipole. The oceanic viscosity also controls the velocity of the decay of the ocean layer thickness. It occurs faster for the lower viscosity.
The magnitude of the atmospheric forcing does not change much the qualitative behavior of the ocean dynamics. The only difference, is that the layer thickness decreases slower for the weaker forcing and so it lets time for the dipole to advect in the down wind direction for the larger viscosity. The advection is only of a few kilometers and a real detachment of the dipole as in the other studies (Jia et al. [2011],Yoshida et al. [2010]) is not observed here.

The oceanic eddies are formed by the injection of vorticity of the wind stress curl. Negative vorticity to the left side and positive vorticity to the right side is generated as in the atmosphere. Nevertheless each layer develops its own dynamics, with different characteristic length scales. The down-wind scale of the wind wake in the atmosphere is of about 700km (of the order of the atmospheric Rossby radius of deformation $Rd_a \simeq$600km), whereas the typical down-wind length scale of the main dipole in the ocean is about 300km (when the ocean thickness layer reaches 30meters), and about 50km ($Rd_o \simeq$40km) for the secondary dipole. This is in agreement with in situ data which find eddies of about 200km in the lee of Madeira island (Jia et al. [2011]), Philippine Islands (Pullen et al. [2008]) and Hawaiian islands (Yoshida et al. [2010]) .

Moreover the atmospheric wind forces the ocean in the x-direction at all locations, whereas a strong counter current in the upwind direction is formed in the ocean, at the middle of the dipole. This demonstrates, that although the atmospheric wind wake is the most important process, for the ocean dynamics around an island, the ocean develops its own dynamics with a typical scale smaller than that of the atmosphere.

17.2 Quantitative description

For the following, I can defined a Reynolds number:

$$Re = \frac{u^o L}{\nu^o} \tag{17.1}$$

where L=100km is the diameter of the island (the typical scale in our simulations),
u^o is the typical velocity of the counter current, and ν^o the oceanic viscosity.

The Reynolds numbers increase almost linearly in time for each experiment. It is typically around 60 at the end of the simulations.

17.2.1 Time evolution

In the fig 17.4, I represent at the top the time evolution of the maximum/minimum of the oceanic layer thickness. The dash line is the evolution at one fixed point near the center of the anticyclone (layer thickness>200m) and the cyclone (layer thickness <200m).

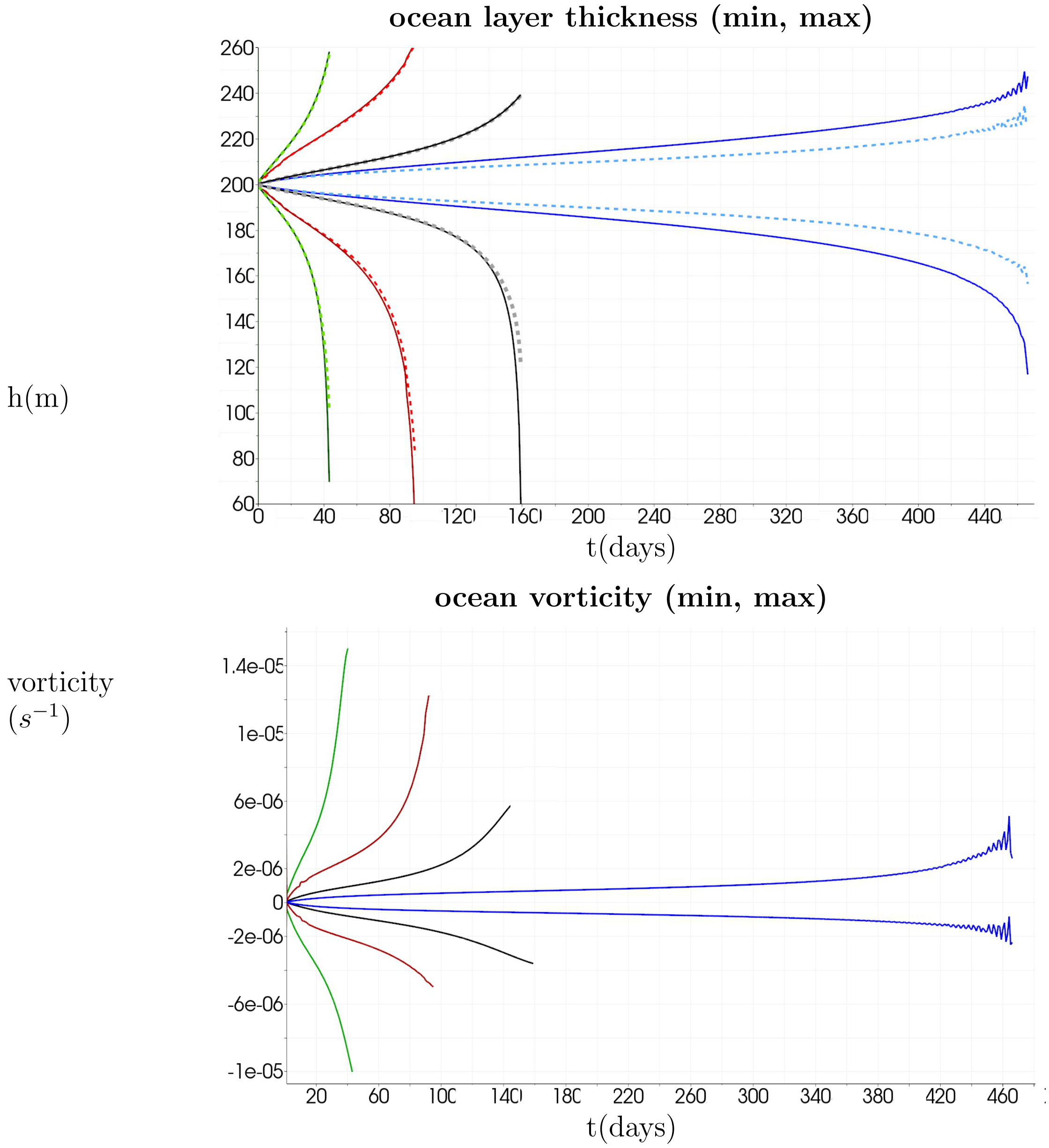

Figure 17.4: Time evolution of the oceanic layer thickness (top) and vorticity (bottom)

——— U^a10_*1000*, ——— U^a10_*4000*,
——— U^a05_*1000*, ——— U^a05_*4000*
– – – *evolution in one point (early extrema)*
——— *evolution of the maximum/minimum*

The center of the cyclone/anticyclone coincides with the maxima of the layer thickness (plain line fig 17.4) except for the simulation with the weakest atmospheric forcing and Reynolds number (U^a05_4000). This simulation continues long enough to have an advection of the dipole which leads to a displacement of the maxima/minima of the ocean layer thickness. In the experiment U^a05_4000 which lasts more time, oscillations are due to the wave propagation and the periodic boundary conditions in the x-direction.

The dipole induces vertical velocities, and more particularly an upwelling in the cyclone (the layer thickness decreases) and a downwelling (the layer thickness increases) in the anticyclone (fig 17.4). The evolution shows the asymmetry between the cyclone and the anticyclone. Indeed in the cyclone the layer thickness becomes thinner; the transmission of energy by the atmosphere is more efficient and increases the cyclonic velocity and strengthens the upwelling.

Unlike in the anticyclone, where the layer thickness increases, the transmission of energy becomes less efficient so it grows slower. This is of a great interest for biological process as they are related to upwelling.

At the very beginning (< 10 days for U5 and < 40 days for U10) there is no dependence on the oceanic Reynolds number. Only the atmospheric forcing governs the ocean dynamics. After several days, the eddy dynamics becomes dominant and Reynold's number dependent. The speed of the decay of the layer thickness in the cyclone depends on the Reynolds number. For higher Reynolds numbers the velocity increases faster and leads to a faster drop of the layer thickness than for the smaller Reynolds number. The minimum of ocean layer thickness is always situated at the center of the cyclone regardless of the presence of the secondary dipole. The secondary dipole does not play an important role for the extremal vertical motion.

In a shallow water model the ocean vertical velocity at the surface vanishes. I can determine the vertical velocity at the bottom of the oceanic layer by the difference of its depth between two time steps. The vertical velocities increase in time. At the beginning, for the upwelling, they are about 0.1m/day for the atmospheric forcing of 5m/s, and 0.7m/day for the atmospheric forcing of 10m/s. It increases up to 10m/day for the cyclone for a layer thickness of 70m for the atmospheric forcing of 10m/s and the viscosity of 1000m/s^2. For the anticyclone the downward vertical velocity never exceeds 2m/day.

The vorticity evolution (fig 17.4, bottom), shows also the asymmetry between the cyclone and the anticyclone. After a few days, it depends on the forcing and the Reynolds number. Vorticities increase as the dipole intensifies in time. The positive vorticity of the cyclone increases faster and reaches higher values than the negative vorticity. This is in agreement with the previous explanation based on the layer thickness.

17.2.2 Oceanic transport around the dipole

The study of the transport in the ocean surrounding the dipole is of interest to understand the ocean dynamics around an island, and its influence on biogeochemistry. In the hypothesis of a geostrophic equilibrium the transport can be estimated by:

$$T = \frac{g'^o}{f} \int_A^B h^o(x, y, t) \Delta\eta^o dS \qquad (17.2)$$

$\Delta\eta^o$ is the difference of layer thickness between two points in the ocean.

$h^o(x, y, t)$ is the actual layer thickness and varies in space and time. The transport is estimated in Sverdrup ($1Sv = 10^6 m^3/s$).

The Ekman transport due to the Ekman velocity is very small. Over the entire domain, it is equal to about 1.6Sv, to the right side. Compared to the counter current transport, after a half a day of spin up, it is only about 1%.

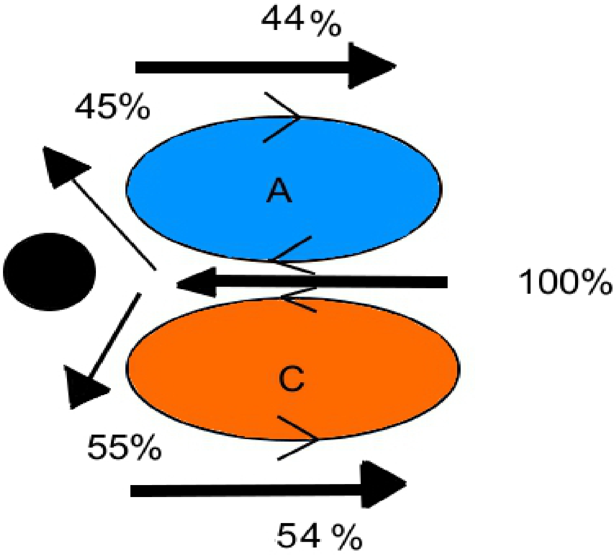

Figure 17.5: Scheme of the transport around the island for a layer thickness in the cyclone of about 150 meters.

The strong counter current between the cyclone and the anticyclone induces an important transport to the up-wind direction, in the ocean. It increases in time because the strength of the dipole grows and so the velocity and the difference of layer thicknesses increases (17.1). Due to this counter current, the ocean losses energy in this place unlike to other places in the domain where ocean gains energy from the atmosphere. The transport of the counter current is then directed to the left or to the right when approaching the island (see fig 17.5). More or less all the transport of water (98% of the initial transport) injected in the eddies is then directed down wind. The water is not transported to the up-wind where only the Ekman transport is present.

The transport of water increases with the strength of the atmospheric forcing. As it is shown previously, the dipole structure does not reach a stationary state so the ocean transport evolves in time. It becomes stronger and is also modified in space. Fig 17.6 shows the evolution of the percentage of transport coming from the counter current and going to the right side (as defined in fig 17.5). The complementary part is the part going to the left side. The evolution trend is similar for all the simulation (fig 17.6). At the begin, there is an equipartition in the both direction as the geometry of the forcing is symmetric and the Ekman transport negligible. Over time the dipole grows but also the asymmetry between the cyclone and the anticyclone due to the difference of layer thicknesses. The cyclone increases faster than the anticyclone (fig 17.4). That is why the transport becomes stronger to the right than to the left direction. Before the layer thickness reaches 30 meters, about 65-75 % of the water turns to the right and only 25-35% goes to the left side.

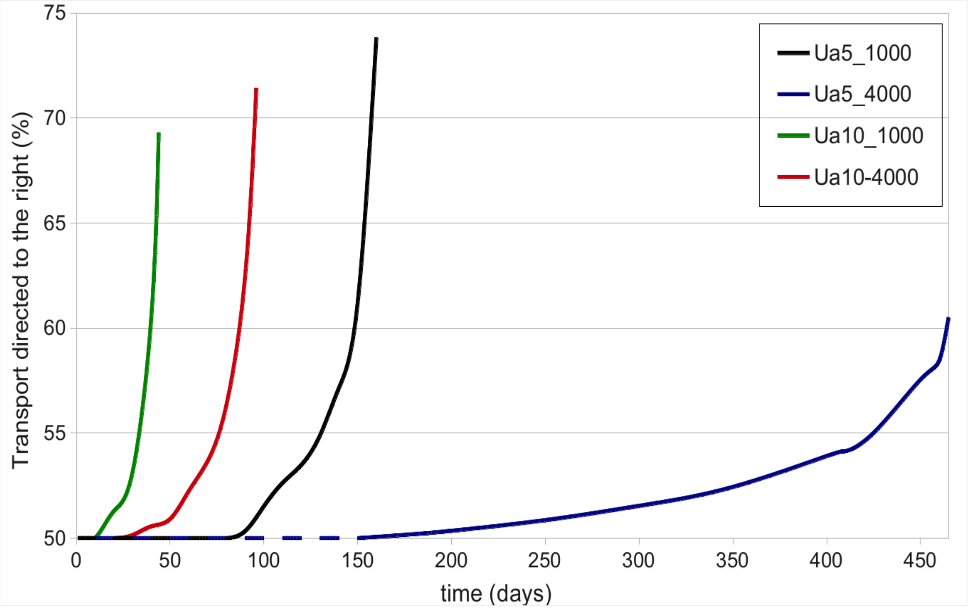

Figure 17.6: Time evolution (in days) of the percentage of transport going to the larger y-values (dark color) and to the lower y-values (light color) for the four simulations

17.3 Decomposition of the vorticity and the wind stress acceleration

17.3.1 Vorticity decomposition

In this part, I split the calculation of the vorticity of the atmospheric forcing in two parts (Plougonven et al. [2015])

$$\zeta = \partial_x v - \partial_y u = \partial_x |u| v' - \partial_y |u| u' \tag{17.3}$$

$$= |u|(\partial_x v' - \partial_y u') + v' \partial_x |u| - u' \partial_y |u| \tag{17.4}$$

where $|u|$ is the vector norm and u' v' are the components of the normalized velocity vector. The first term ($|u|(\partial_x v' - \partial_y u')$) is the contribution of the change of direction of the velocity vector and the second one$(v'\partial_x|u| - u'\partial_y|u|)$ the contribution due to the change of the speed.

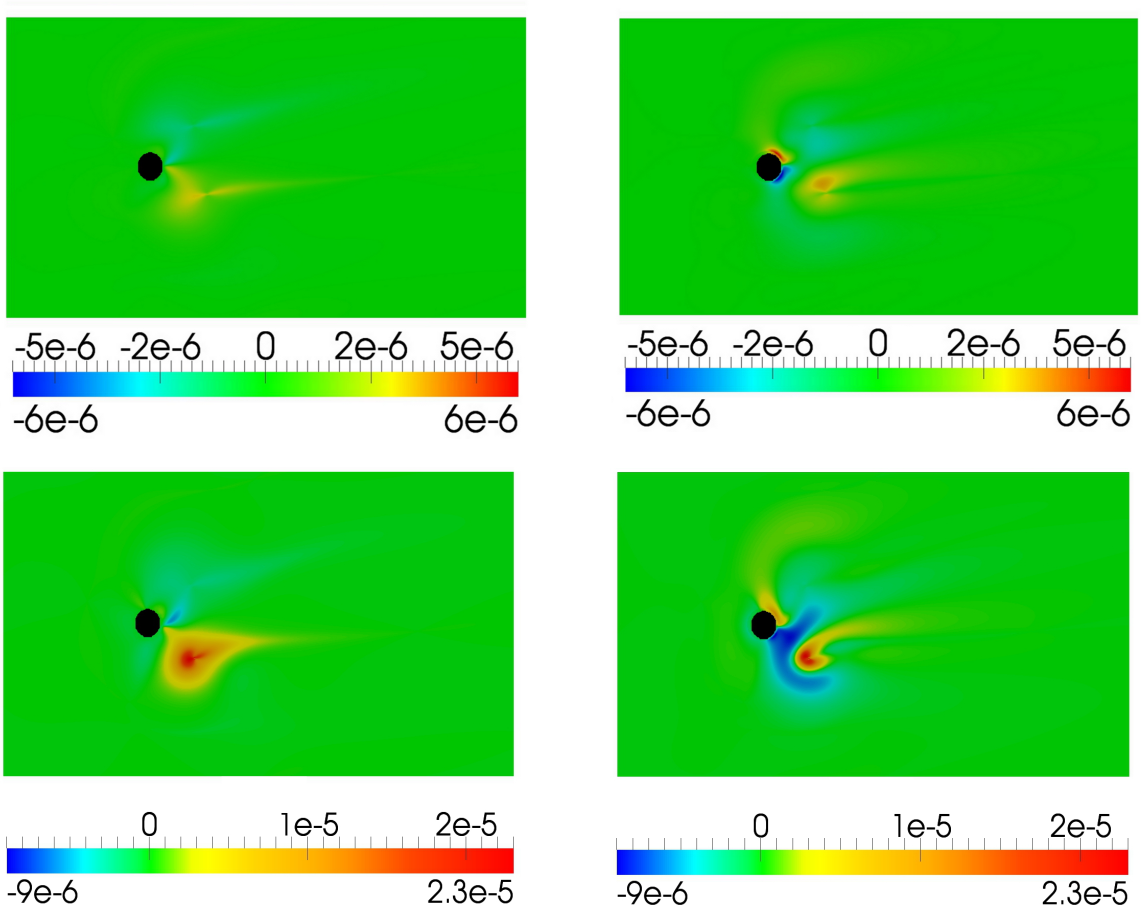

Figure 17.7: Vorticity decomposition (s^{-1}) of the ocean vorticity, for an atmospheric forcing of 10m/s and a viscosity of $4000m^2/s$ after 40days at the top and 95days at the bottom. The contribution of the change of direction of the velocity vector is represented at the left whereas the contribution of the change of speed is represented to the right. Only 2500km of the domain, in the x-direction, is represented.

Please note, that mathematically this decomposition is ill-defined, not Galilean invariant. But note also that Galilean invariance is broken already by the presence of the island.

Almost all the vorticity in the atmospheric forcing is due to the change of speed (not shown) as the atmosphere is not turbulent (the directional part is negligible, wind vectors are always in the positive x-direction). In the ocean, the vorticity becomes evenly distributed between the two terms except at the beginning around the island (fig. 17.7, 17.8). Indeed the vorticity generated by the change of speed around the island is very strong because of the no slip boundary condition. Speeds decrease near the island and the shear gives rise to negative vorticity towards the right and positive vorticity toward the left side. This generation of vorticity by the magnitude term leads to the secondary dipole for higher Reynolds numbers (fig. 17.8).

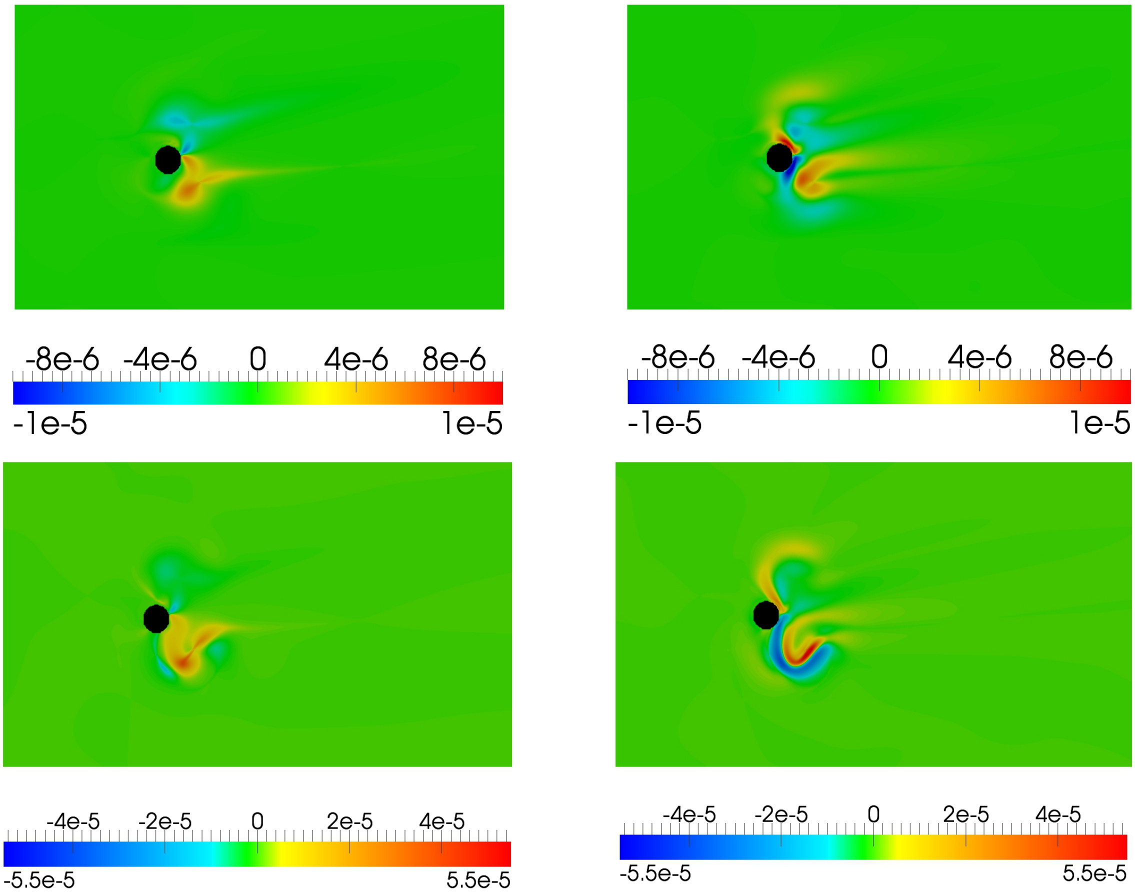

Figure 17.8: Vorticity decomposition (s^{-1}) of the ocean vorticity, for an atmospheric forcing of 10m/s and a viscosity of $1000m^2/s$ after 30days at the top and 45days at the bottom. The contribution of the change of direction of the velocity vector is represented at the left whereas the contribution of the change of speed is represented to the right. Only 2500km of the domain, in the x-direction, is represented.

17.3.2 Forcing of the wind stress curl

I can perform a decomposition of the curl of the acceleration of the ocean by the wind stress.

$$rot\overrightarrow{a} = \nabla \times \frac{\overrightarrow{F}}{\rho^o h^o} = \frac{1}{\rho^o h^o}\nabla \times \overrightarrow{F} - \frac{1}{\rho^o h^{o2}}(F^y \partial_x h^o - F^x \partial_y h^o) \tag{17.5}$$

where $\overrightarrow{F} = \rho^a C_d |u^a - u^o|(\overrightarrow{u^a} - \overrightarrow{u^o})$ is the wind stress.

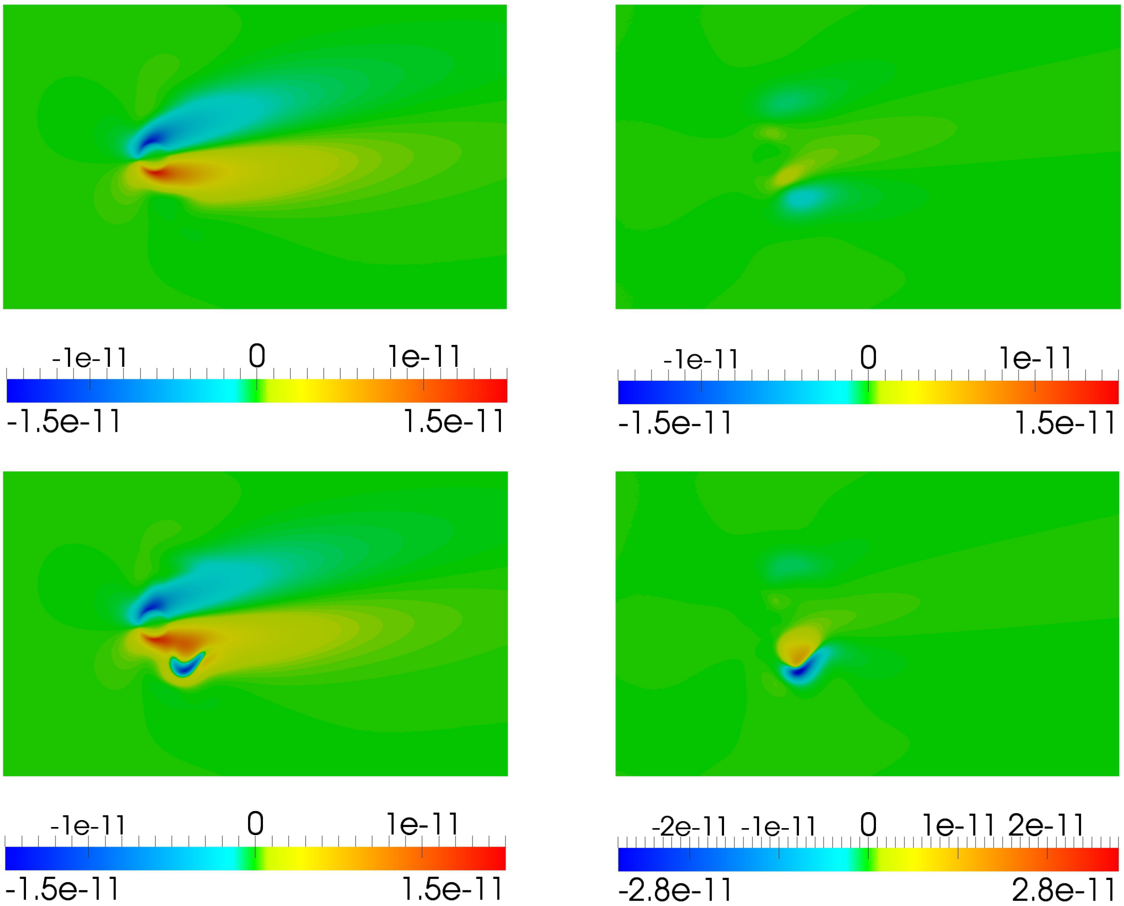

Figure 17.9: Decomposition of the acceleration curl (s^{-1}) for an atmospheric forcing of 10m/s and a viscosity of $1000m^2/s$ after 30days at the top and 45days at the bottom. The contribution related to the wind stress curl is represented at the left whereas the contribution depending on the ocean layer thickness is represented to the right. Only 2500km of the domain, in the x-direction, is represented.

In fact the curl of the acceleration is due to two factors. The first one $\frac{1}{\rho^o h^o}\nabla \times \overrightarrow{F}$ is directly related to the wind stress curl. The second one, $\frac{1}{\rho^o h^{o2}}(F^y \partial_x h^o - F^x \partial_y h^o)$, depends on the gradient of the ocean surface-layer thickness in the direction perpendicular to the wind stress. The vorticity injection into the ocean does not depend only on the velocity of the atmosphere and the ocean as it could be naively thought, but also on the ocean layer thickness, as can be seen from equation 17.5.

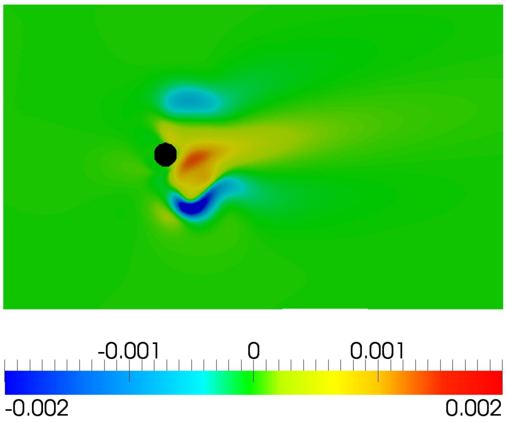

Figure 17.10: Gradient of the ocean layer thickness (m/m) in the y-direction (perpendicular to the atmospheric forcing). Only 2500km of the domain, in the x-direction, is represented.

The part induced by the wind stress itself does not depend much on the ocean dynamics. It is almost constant for one atmospheric forcing and is almost constant during the simulation as ocean velocities are small. However, when the oceanic layer is thinner, strong ocean velocities are generated and have a stronger influence on the wind stress (fig 17.9, bottom left). In this case the velocity difference between the wind and the current for the calculation of the wind stress cannot be neglected.

The other part ($(F \times \bigtriangledown h)_y$) generated by the oceanic surface-layer thickness gradient increases until it becomes of the same order of magnitude than the other part. At the beginning it is small because the relative variation in the layer thickness of the ocean is small (fig 17.9, top right). After several days the wind stress injects negative oceanic vorticity at the left and positive vorticity at the right (due to the curl generated by the wind wake) of the island. This leads to the dipole in the ocean which grows and leads to a high gradient of layer thickness (fig 17.10). Oceanic vorticity is then generated because the surface-layer thickness (in the y-direction) is orthogonal to the wind stress (in the x-direction) (fig 17.9).

The secondary dipole created by the no-slip boundary condition of the island, turns around the cyclonic eddies and contributes to the gradient of layer thickness in the direction perpendicular to the atmospheric forcing.

Chapter 18

Conclusion

This study, first, confirms that the wind wake induced by the presence of the island (represented through an increased drag coefficient) is the main process leading to oceanic mesoscale eddies. A dipole with a cyclonic eddy at the right and an anticyclonic eddy at the left separated by a counter current in the up-wind direction are induced. The direct effect of the island in the ocean (when the wind wake is neglected) seems to be insignificant. Indeed it only generates low vorticity in the boundary layer. The main dipole generates vertical movement in the ocean important for the biogeochemistry. At the beginning of the simulations, the ocean dynamics depends only on the atmospheric forcing, but the further evolution, especially of the vertical motion, depends strongly on the Reynolds number. For higher Reynolds number the upwelling is stronger than for the smaller Reynolds number. After the set up of the ocean dynamics according to the atmospheric forcing, the presence of the island in the ocean becomes as important as the wind wake, for the ocean dynamics. Indeed, the boundary layer around the island induces vorticity along the island at the periphery of the main dipole. In case of a higher Reynolds number, a secondary dipole of smaller scale (few tens of kilometers) is generated in the boundary layer and displaced by the current around the main dipole. This dipole does not play an important role for the upwelling which is only controlled by the oceanic viscosity and the atmospheric forcing.

Unfortunately, today a lot of numerical models have a coarse resolution in the atmosphere and so neglect the presence of smaller islands and so the effect of the wind wake for the ocean dynamics. This shows that fine spatial resolution in the ocean and in the atmosphere are key to a realistic modeling of the ocean dynamics. Moreover this model needs high numerical viscosity for numerical stability and so may overestimate the upwelling in the ocean.

Dipoles in the lee of islands extending a few hundreds of kilometers are observed (Jia et al. [2011], Pullen et al. [2008], Yoshida et al. [2010]), this corresponds to the order of magnitude of the main dipole generated by the wind wake in my simulations. The secondary dipole generated by the friction with the island has not been observed to the best of my knowledge. It should be of great interest to search in observational and in situ data if oceanic small eddies are generated in the down wind side by the oceanic boundary

layer dynamics.
An other important point described in this study, is that the vorticity is not only injected directly by the curl of the the wind stress. It is also generated by a gradient of the oceanic layer thickness perpendicular to the wind. Like in the first study I find that the wind stress depends on the oceanic velocity in case of strong currents and can modify the vorticity injection.

Research of how the ocean dynamics evolves in case of a turbulent wind wake or when the atmospheric forcing is stopped could further the understanding of the displacement of the eddies in the wake of islands (as in Madeira island when the wind wake is less important). An even more idealized study with a more idealized model with a linear cost line is needed to really understand the vortex generation in the ocean and their displacement in function of the atmospheric forcing. An other prospect would be to take into account the beta effects in the simulation which can have an important effect on the vorticity and on the self advection of the dipole (Cushman-Roisin et al. [1990]). For the case of the Hawaiian islands the β-plume extends several thousand kilometers to the east (e.g. Jia et al. [2011]).

Part V

Conclusion and prospects for future work

18.1 Conclusion

The aim of this PhD is to study the coupled dynamics between the ocean and the atmosphere, due to momentum flux only, at the synoptic and the mesoscale.
Currently, studies concerned with the influence of the ocean on the atmosphere are made considering SST induced processes but not the involvement of surface ocean currents. Much of the small scale variability in the wind stress field are assigned to SST modification of low level winds through the influence of air sea-heat flux on the marine atmospheric boundary layer (Chelton et al. [2004]). However the effect of momentum exchange at the mesoscale remains unexplored and unknown while they may have an important role (evenf if it is secondary compared to the SST) in the air-sea interaction, as shown in this thesis.

This study question the importance of the surface shear stress parametrization in simulations of the ocean dynamics, the coupled ocean-atmosphere and the atmosphere dynamics. Indeed it should be parametrized as a function of the difference between wind and current. Because they did not account for the effects of ocean currents on the wind stress, numerical weather prediction models until few years ago, did not provide the true wind stress that drives the ocean circulation (Chelton et al. [2004]). This study allows to determine how is important to use a consistent parametrization, and what are the physical processes imply and how they change at mesoscale and synoptic scale. It also questions the quantification and the place of the energy exchange between the ocean and the atmosphere in case of turbulent simulations. And furtherit questions the physical process involved when an island is present in the ocean.

I recall that all the results are obtained using an idealized but consistent model. The idealized model allows a high spatial and temporal resolution, and is better suited for answering to specific questions of momentum exchange at mesoscale as it does not imply a lot of connected phenomena. The model is based on two superposed one-layer fine-resolution shallow-water models. The upper layer represents the atmosphere and the lower layer the ocean. The interaction is only due to the shear between the two layers. The shear applied to the ocean is calculated using the velocity difference between the ocean and the atmosphere. The frictional force between the two-layers is implemented using the quadratic drag law. The particularity is that the shear applied to the atmosphere is consistent and calculated using the difference of velocities between the wind and the current.
Three model configurations are explored (part II, part III, and part IV). The results reproduced but also revealed innovent mechanical processes, which could appear also in the reality or more realistic models.

The results of this PhD, give quantitative results on the correlation of vorticity (instantaneous and average) and the energy transfer from below the oceanic Rossby radius to above the atmospheric Rossby radius of deformation. Results differ from previous investigations where the exchange of momentum was considered at basin scale. It is shown that the ocean has a passive role, absorbing kinetic energy at nearly all times and locations as expected. The energy input to the ocean increases almost quadratically with the value of the drag coefficient.

Due to the small velocities in a turbulent ocean, as compared to the atmosphere, the energy transfer depends only weakly on the ocean velocity. The shear calculation using the velocity difference between the ocean and the atmosphere, for the two layers, seems important in some particular case (particularly strong current). Results of the Part II, show that it can lead to instabilities due to the air-sea interaction with a quadratic drag law and horizontal viscous dissipation in the atmosphere. We have demonstrated, that the complicity of turbulent friction between the air and the ocean, and the horizontal turbulent friction in the atmosphere triggers a barotropic instability in the ocean which can propagate to the atmosphere, in this idealized case. The instability explanation is based on physical arguments which apply also to more involved models and to the nature of the air, the sea and their interaction. Nevertheless, including ocean velocities in the air-sea interaction does not seem indispensable for the turbulent simulations and the island study while the ocean current is not strong. Indeed in the Part IV, simulations taking into account or not the velocity difference between the atmosphere and the ocean for the shear applied to the atmosphere give nearly the same results in the major part during simulations. This parametrization only becomes important when the ocean currents are faster for example when the ocean layer thickness decreases strongly (end of simulations).

The ocean dynamics leaves nevertheless its imprint in the atmospheric dynamics leading to a quenched disordered state of the atmosphere-ocean system, for the highest value of the friction coefficient considered (Part III). An unexpected phase transition appears in the dynamics of the atmosphere-ocean system when the drag coefficient is increased from $C_d = 4\times 10^{-4}$ to 8×10^{-4}. For the higher drag coefficient, the time variability is largely reduced whereas the spatial variability increases, the system is in a quenched disordered state. Non-ergodicity in a simple model does not mean that the real world configuration is non-ergodic. But when the situation is non-ergodic in a simple model this can indicate that there might be a very slow evolution of a configuration in the real world.
This behaviour looks similar to the glass transition in condensed matter physics. Although the transitions are observed and studied since several decades solid theoretical results, which allow for a deeper understanding are still scant. In condensed matter physics the glass transition is strongly favoured by mixtures of two or more types of molecules with different correlation scales, which seems similar to what occurs in our model with two disparate length scales (Rossby radius of the atmosphere and the ocean). This finding questions the ergodic hypothesis for the idealized configuration studied here. The ergodic hypothesis is at the basis of a large number of experimental, observational and numerical results in ocean, atmosphere and climate dynamics.
In this simulation in quenched disorder state, the high instantaneous correlation between the vorticity in the atmosphere and the ocean show that the ocean currents leave a definite imprint in the atmospheric winds leading to fine scale structures in the atmosphere. This suggest, that the fine scale structures of the ocean dynamics which have recently been

exposed by fine resolution satellite observations can influence the atmospheric dynamics through momentum transfer, even when heat-fluxes are excluded.
Moreover, a high attraction of the atmospheric dipole is shown when there is a high correlation between the oceanic and atmospheric structures. The near surface processes such as mesoscale positive vorticity anomalies are important in the bottom-up scenarios of hurricane genesis (Fang and Zhang [2008]). The capture of atmospheric eddies by oceanic structures and their co-evolution can be relevant in this context.

The phase change needs to be further investigated and better appreciated before drawing conclusion of how relevant it can be for the climate system and the hurricane genesis. An even more idealized model is needed to explore these results further (see Prospects).

Study Part IV, confirms that the wind wake induced by the presence of the island (represented in the atmosphere through an increased drag coefficient) is the main process leading to oceanic mesoscale eddies. The direct effect of the island in the ocean (when the wind wake is neglected) seems to be insignificant to initiate the dipole. Further, the boundary layer around the island induces vorticity along the island at the periphery of the main dipole. In case of a higher Reynolds number, a secondary dipole of smaller scale (few tens of kilometers) is generated in the boundary layer and displaced by the current around the main dipole. This dipole does not play an important role for the upwelling which is only controlled by the oceanic viscosity and the atmospheric forcing. This secondary dipole generated by the friction with the island has been observed in laboratory experiment (Verzicco et al. [1995]) but not in in-situ data to the best of my knowledge.
An other important point described in this study, is that the vorticity is not only injected directly by the curl of the wind stress but also by the atmosphere-ocean coupling. Vorticity is generated by a gradient of the oceanic layer thickness perpendicular to the wind. This result seems obvious but as never been discuss for the air-sea interface to the best of my knowledge. It is only rapidly described for the bottom friction (Grubisic et al. [1995]).

For the numerical modeling, I demonstrated that, a consistent and precise representation at high resolution in both the ocean and the atmosphere, leads to new phenomena in all the three configurations.
This work shows the importance of idealized simulations. The use of idealized models is inevitable because of the expensive coast of realistic models. Idealized models (and analytical calculation) are key to identify specific processes and understand their physics. Moreover idealized models can used finner resolution and allows to find new processes.
This PhD demonstrates that fine spatial resolution in the ocean and in the atmosphere are key to a realistic modeling of the ocean and the atmosphere dynamics. In all the three configurations, a fine resolution which resolves the Rossby radius of deformation of the ocean (Part II,III) and takes into account small islands of a few tens of kilometers (Part IV), in the ocean and in the atmosphere appears to be essential for the dynamics of the ocean but also for the dynamics of the atmosphere. Indeed, coarser resolution leads to neglect the small oceanic perturbations and the orography (like small island) in the atmosphere. The idealized model used here, needs high numerical viscosity for numerical

stability due to the initial shock in the spin-up and the resolution of the dynamics in the horizontal boundary-layer (Part IV), and so may overestimate the upwelling in the ocean. It resolves barely more than the small scales of the secondary dipole.
Unfortunately, today a lot of numerical models have a coarse resolution in the atmosphere. They neglect the presence of smaller islands and so the effect of the wind wake for the ocean dynamics which is the main process for the dipole generation. They do not resolve the Rossby radius of deformation of the ocean in the atmosphere and so cannot well resolve the imprint of the ocean on the atmosphere.
Realistic models which are as important as idealized models for studying the ocean and atmosphere dynamics, do not allow the smaller scale dynamics not only in the atmosphere, but also in the ocean and neglect some mesoscale processes which can be essential for the global dynamics, the biological processes and the climate system.

18.2 Prospects

Clearly, many ways can be explored to continue the work started in this thesis. Perspectives could be arranged in four main groups according to the coveted objectives. They consist in using other configurations of the actual model or a more realistic model or simpler models or also using observational data.

1. CHANGING CONFIGURATION:

   The shallow-water model could be used with a different forcing to established the relationship between the drag coefficient and the fundamental nature of the atmosphere ocean coupling. This is of importance to determine how the conclusions depend on the scale and type of the forcing.

   It could also be of interest to research the critical drag coefficient for the phase change (Part III) in case of a shallow water model, but it has an high computational cost to perform the simulations.

   In the Part IV, the research of how the ocean dynamics evolves in case of a turbulent wind wake or when the atmospheric forcing is stopped could further the understanding of the eddies dynamics, in the wake of islands (as in Madeira island when the wind wake is less important).

2. MORE REALISTIC MODEL:

   More realistic models are indeed essential to get closer to reality. It seems to me of great interest to add an other layer to the ocean and the atmosphere. This way baroclinic instability is included, a fundamental process in nature. Its influence on the air-sea interaction should be investigated.

For the dynamics around islands, it would be necessary to include β-effect which is neglected with the periodic boundary condition, but important in real studies of tropical islands. Taking into account the β-effect in the simulation can have an important effect on the vorticity and on the self advection of the dipole called β-plume (Cushman-Roisin et al. [1990]). For the case of the Hawaiian islands the β-plume extends several thousand kilometers to the east (e.g. Jia et al. [2011]).

Heat fluxes at the air-sea interface have demonstrated their importance for both, the atmosphere and the ocean (Chelton and Xie [2010]). Next, it could be interesting to add heat fluxes to study the non-linear interaction with the shear, and determine the influence of each other on the ocean and atmosphere dynamics.

3. SIMPLER MODEL:

   The idealized model used here is sometimes still too complicated to understand all the details of the physical processes as for the quenched disorder state or the dynamics around the island. It could be of interest to study the dynamics with an even simpler model.

   Even when the situation is non-ergodic in an idealized model it might well be ergodic in a more involved model or in the real world. The phase change needs to be investigated and better appreciated in a simpler model to understand the physics behind this mechanism and give hypothesis on the real ocean-atmosphere coupling. A point vortex or quasi-geostrophic model for studying the quenched disorder state (Part III) seems to be more suitable to understand this process. It could allow to study the dependence of the spatial disorder on the forcing and the scales. And could also bring more details on the capture of atmospheric eddies by oceanic structure and their co-evolution.

   For the study of air-sea-land interaction (Part IV) a simpler configuration with a linear coastline instead of a circular island in the last part would increase our understanding. It could lead to a better comprehension of the vortex generation in the ocean and their displacement in function of the atmospheric forcing.

4. FINE RESOLUTION OBSERVATIONS:

   The research of small scale structures in the ocean near lines and points of vanishing wind-stress could be of interest to find oceanic instabilities in the ocean. Fine resolution observations provided by satellite data of the sea surface, together with observations of the ocean wind stress will be used to track down the instability discover in the ocean (Part II).

To evaluate the robustness of our results, observational studies similar to Chelton et al. [2004] should also consider the correlation between persistent winds in the atmospheric boundary layer and currents in the oceanic boundary layer, at small scales (Part III). To evaluate the pertinence of these findings it could be of interest to combined observations of the dynamics in the atmospheric and oceanic boundary layer.

The existence of the secondary dipole (analyzed in Part IV), also found in experimental studies (Verzicco et al. [1995]), have to the best of my knowledge never been observed. It should be of great interest to search in observational and in situ data if oceanic small eddies are generated in the down wind side by the oceanic boundary layer dynamics. Fine resolution observations in the lee of islands could be necessary to deduce the existence or not of this secondary dipole due to the horizontal friction with the island itself (observed in experimental studies).

Bibliography

AMS. American meteorological society s glossary of meteorology, 2015. URL http://glossary.ametsoc.org/wiki/Synoptic. 2015-06-27.

E. D. Barton, G. Basterretxea, P. Flament, E. G. Mitchelson-Jacob, B. Jones, J. Arístegui, and F. Herrera. Lee region of gran canaria. J. Geophys. Res., 105:17173–17193, 2000. DOI: 10.1029/2000JC900010.

M.A. Bender, R.J. Ross, R.E. Tuleya, and Y. Kurihara. Improvements in tropical cyclone track and intensity forecasts using the gfdl initialization system. Mon. Wea. Rev., 121: 2046–2061, 1993. DOI: 10.1029/2000JC900010.

L. Berthier and G. Biroli. Theoretical perspective on glass transition and amorphous materials. Rev. of Mod. Phys., 83:587–645, 2013. DOI: 10.1103/RevModPhys.83587.

P.H.R. Calil, Richards K.J., Y. Jia, and Bidigare R.R. Eddy activity in the lee of the hawaiian islands(deep-sea research ii). 55/10-13:1179–1194, 1993. DOI: 10.1016/j.dsr2.2008.01.00.

X. J. Capet, P. Marchesiello, and J. C. McWilliams. Upwelling response to coastal wind profiles. Geophys. Res. Lett., 31, 2004. DOI: 10.1029/2004GL020123.

J. Charney and A. Eliassen. On the growth of the hurricaine depression. J. Atmos Sciences, 21:68–75, 1964.

C. Chavanne, P. Flament, D. Luther, and K-W. Gurgel. The surface expression of semidiurnal internal tides near a strong source at hawaii. part ii: Interactions with mesoscale currents. J. Phys. Oceanogr., 40:1180–1200, 2010. DOI: 10.1175/2010JPO4223.1.

D. B. Chelton and S. P. Xie. Coupled ocean-atmosphere interaction at oceanic mesoscales. Oceanography, 23:52–69, 2010. DOI: 10.5670/oceanog.2010.05.

D. B. Chelton, M. G. Schlax, M. H. Freilich, and R. F. Milliff. Satellite measurements reveal persistent small-scale features in ocean winds. Science Mag, 303:978–983, 2004.

D. Chen and G.H. Jirka. Absolute and convective instabilities of plane turbulent wakes in a shallow water layer. JFM, 338:157–172, 1997.

R. Courant, K. Friedrichs, and H. Lewy. Uber die partiellen differenzengleichungen der mathematischen physik. Mathematische Annalen (in German), 100:32–74, 1928. DOI: 10.1007/BF01448839.

X. Couvelard, R. M. A. Caldeira, I. B. Araujo, and R. Tomé. Wind mediated vorticity-generation and eddy-confinement, leeward of the madeira island: 2008 numerical case study. Dynamics of Atmospheres and Oceans, 58:128–149, 2012.

B. Cushman-Roisin, E. Chassignet, and B. Tang. Westward motion of mesoscale eddies. Journal of Geophysical Oceanography, 20:758–768, 1990.

T. H. A. Duhaut and D. N. Straub. Wind stress dependence on ocean surface velocity: Implications for mechanical energy input to ocean circulation. Journal of physical oceanography, 36:202–211, 2006.

K. Emanuel. Contribution of tropical cyclones to meridional heat transport by the oceans. Journal of Geophysical Research, 106, 2001.

I. Esau. Indirect air–sea interactions simulated with a coupled turbulence-resolving model. Ocean Dynamics, 64:689–705, 2014.

J. Fang and F. Zhang. Initial development and genesis of hurricane dolly. J. Atmos Sciences, 67:655–672, 2008. DOI: 10.1175/2009JAS3115.1.

R. Ferrari and C. Wunsch. Ocean circulation kinetic energy: Reservoirs, sources, and sinks. Annual Review of Fluid Mechanics, 41:253–282, 2009. DOI: 10.1146/annurev.fluid.40.111406.102139.

V. Grubisic, R.B. Smith, and C. Schar. The effect of bottom friction on shallow-water flow past an isolated obstacle. J. Atmos. Sci., 52:1985–2005, 1995.

A. Mc C. Hogg, W.K. Dewar, P. Berloff, S. Kravtsov, and D.K. Hutchinson. The effects of mesoscale ocean–atmosphere coupling on the large-scale ocean circulation. J. Climate, 22:4066–4082, 2009.

U. Högström, A. Rutgersson, E. Sahlée, A.-S. Smedman, S. Tihomir Hristov, W. M. Drennan, and K. K. Kahma. Air-sea interaction features in the baltic sea and at a pacific trade-wind site: An inter-comparison study. Bound.-Layer Meteorol., 147:139–163, 2013. DOI: 10.1007/s10546-012-9776-8.

IPCC. Climate change 2007: The physical science basis (ch8), 2007. URL http://www.ipcc.ch/publications_and_data/ar4/wg1/en/contents.html.

Y. Jia, P. H. R. Calil, E. P. Chassignet, E. J. Metzger, J. T. Potemra, K. J. Richards, and A. J. Wallcraft. Generation of mesoscale eddies in the lee of the hawaiian islands. Journal of Geophysical research, 11:1–18, 2011. DOI: 10.1029/2011JC007305.

W. Jin. Wind-stress coefficients over sea surface from breeze to hurricane. Journal of Geophysical Research, 87:9704–9706, 1982.

V. S. Kuwahara, F. Nencioli, T. D. Dickey, Y. M. Rii, and R. R. Bidigare. Physical dynamics and biological implications of cyclone noah in the lee of hawai'i during e-flux i. Deep Sea Research Part II: Topical Studies in Oceanography, 55:1231–1251, 2008.

C. F. Lumpkin. Eddies and current of the Hawaiian islands. PhD thesis, Univ. of Hawaii at Manoa, Honolulu., 1998.

A. Moulin, , and A. Wirth. A drag-induced barotropic instability in air-sea interaction. Journal of physical oceanography, 44:733–741, 2014.

N. Paldor and M. Ghil. Linear instability of a zonal jet on an f plane. J. of Phys. Oceanogr., 27:2361–2369, 1997.

J. Pedlowsky. An inertial model of the interaction of ekman layers and planetary islands. Journal of physical oceanography, 43, 2013. DOI: 10.1175/JPO-D-13-028.1.

J. Pilqvist. Tutorial - shallowwaterfoam, 2010. URL http://www.tfd.chalmers.se/~hani/kurser/OS_CFD_2010/johanPilqvist/johanPilqvistReport.pdf. 2014-08.

R. Plougonven, G. Lapeyre, and X. Perrot. Impacts of mesoscale sst anomalies on atmospheric mid-latitude storms. work in progress, 2015.

L. Prandtl. Z. angew. Math. Mech. 5, 1:133–139, 1925.

L. Prandtl and H. Schlichting. Das widerstandsgesetz rauher platten. Werft, Reederei, Hafen, 15:1–14, 1934.

J. Pullen, J. D. Doyle, P. May, C. Chavanne, P. Flament, and R. A. Arnone. Monsoon surges trigger oceanic eddy formation and propagation in the lee of the philippine islands. Geophysical Research Letters, 35, 2008. DOI: 10.1029/2007GL033109.

B. Dewitte P. Marchesiello S. Illig V. Echevin G. Cambon M. Ramos O. Astudillo P. Minnis J. K. Ayers Renault, L. Upwelling response to atmospheric coastal jets off central chile: A modeling study of the october 2000 event. Journal of Geophysical Research, 117, 2012. DOI: 10.1029/2011JC007446.

F. Roquet, C. Wunsch, and G. Madec. On the patterns of wind-power input to the ocean circulation. Journal of physical oceanography, 41:2328–2342, 2011.

H. Schlichting and K. Gertsen. Boundary-Layer Theory. Springer Verlag, 2000. ISBN-13: 978-3540662709.

R. B. Scott and Y. Xu. An update on the wind power input to the surface geostrophic flow of the world ocean. deep sea research part i. Oceanographic Research Papers, 56: 295–304, 2009.

H. Seo, R. Murtugudde, M. Jochum, and A. J. Miller. Modeling of mesoscale coupled ocean-atmosphere interaction and its feedback to ocean in the western arabian sea. Ocean Modell, 25:120–131, 2008.

S. D. Smith. Coefficients for sea surface wind stress, heat flux, and wind profiles as a function of wind speed and temperature. Journal of geophysical research, 93:15467–15472, 1988.

M. A. Spall and J. Pedlowsky. Interaction of ekman layers and islands. Journal of Physical Oceanography, 43, 2012. DOI: 10.1175/JPO-D-12-0159.1.

F. K. Stillinger and P. G. Debenedetti. Glass transition thermodynamics and kinetics. Annu. Rev. Condens. Matter Phys., 4:263–285, 2013. DOI: 10.1146/annurev-conmatphys-030212-184329.

R.B. Stull. An Introduction to Boundary Layer Meteorology. Springer, 1988. ISBN: 9027727686.

G. Vallis. Atmospheric and Oceanic Fluid Dynamics. Cambridge Univ. Press., 2006. ISBN: 0-521-84969-1.

R. Verzicco, J.B. Flor, G.J.F. van Heijst, and P. Orlandi. Numerical and experimental study of the interaction between a vortex dipole and a circular cylinder. Exp. in Fluids, 18:153–163, 1995.

H. G. Weller, G. Tabor, H. Jasak, and C. Fureby. A tensorial approach to computational continuum mechanics using object-oriented techniques. Computers in physics, 12:620–630, 1998.

WHOI. Woods hole oceanographic institution, 2013. URL http://www.whoi.edu/ooi_cgsn/page.do?pid=53278. 2013-06-11.

A. Wirth. Etudes et evaluation de processus oceaniques par des hierarchies de modèles. 2010. HDR spécialité sciences de la planète, Université de Grenoble.

A. Wirth, J. Willebrand, and F. Schott. Variability of the great-whirl from observations and models. Deep Sea Research, 49:1279–1295, 2002.

R. A. Wood, M. Vellinga, and R. Thorpe. Global warming and thermohaline circulation stability. JPhil. Trans. R. Soc. Lond.A, 361:1961–1970, 2003.

S. Yoshida, B. Qiu, and P. Hacker. Wind-generated eddy characteristics in the lee of the island of hawaii. Journal of Geophysical Research, 115, 2010. DOI: 10.1029/2009JC005417.

Appendix A

Atmospheric forcing Part II

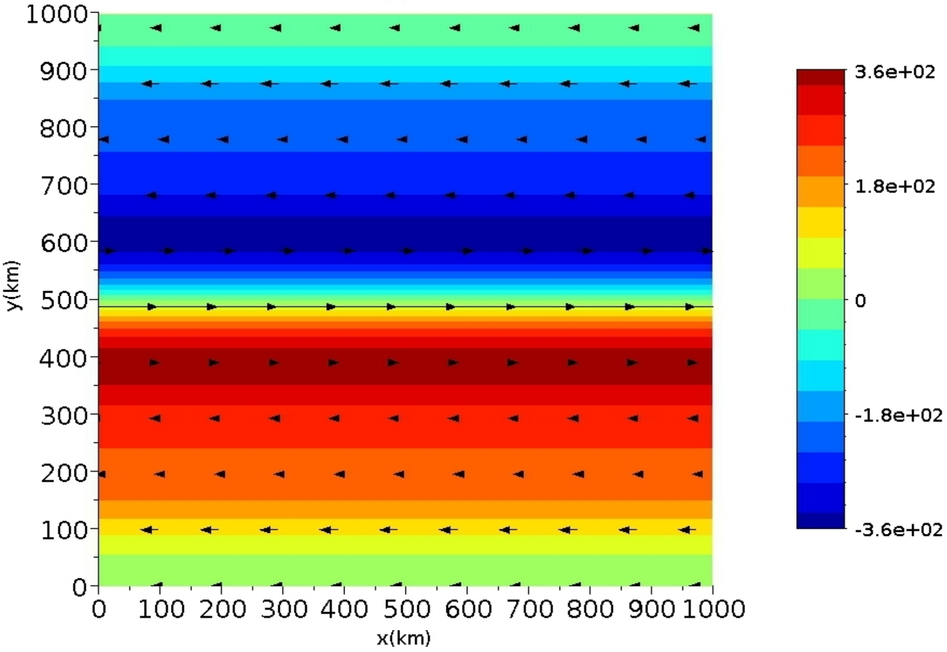

Figure A.1: atmospheric forcing (h_a)

Appendix B

Atmospheric forcing Part III

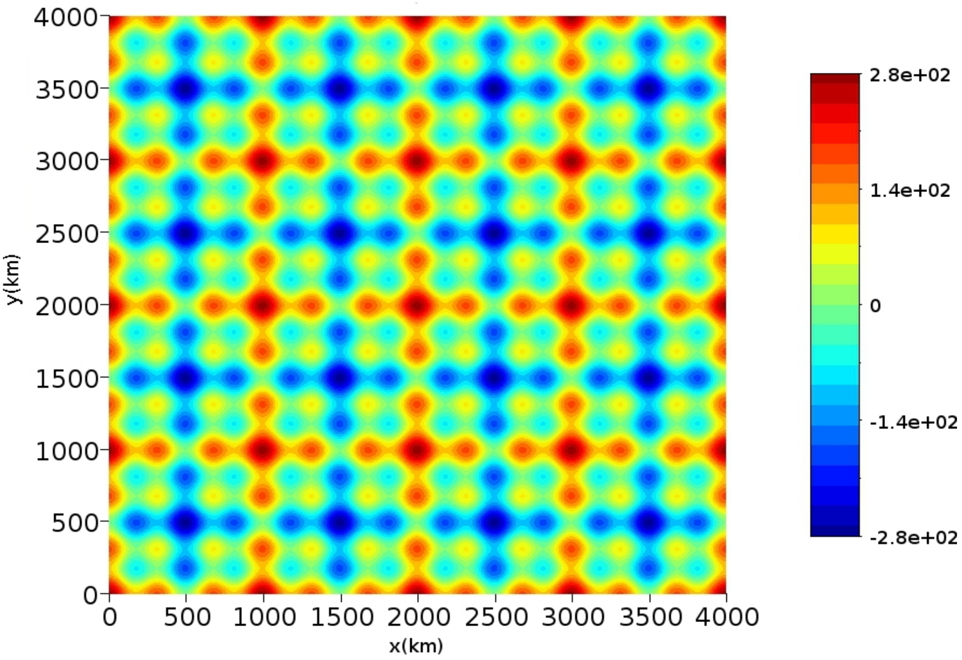

Figure B.1: Atmospheric forcing (h_a)